Towards Faster Data Transfer by Spoof Plasmonics

by

Soumitra Roy Joy

A dissertation submitted in partial fulfillment
of the requirements for the degree of
Doctor of Philosophy
(Electrical and Computer Engineering)
in The University of Michigan
2020

Doctoral Committee:

Professor Pinaki Mazumder, Chair
Professor Theodore B. Norris
Professor John Schotland
Professor Herbert G. Winful

Soumitra Roy Joy
srjoy@umich.edu
ORCID iD:0000-0002-8363-3385

I dedicate this thesis to my affectionate father, my all-enduring mom, my best-friend sister, my dearest sacrificing wife and my heartiest loveliest son

ACKNOWLEDGEMENTS

Thanks to my wife Priyanka Mozumdar for making the utmost sacrifice to her career to support my PhD journey.

Thanks to my parents, Swapan Talukder and Gita Saha for all the struggle they have voluntarily taken to ensure my success.

Thanks to my advisor Prof. Pinaki Mazumder who kept his faith on my ability and acted like a parent to me in a foreign land.

Thanks to my mentor Dr. Mikhail Erementchouk whose company enriched my scientific and philosophical thought.

And of-course thanks to my lovely 2-years old son Arjun Roy to bring a new meaning to my life.

TABLE OF CONTENTS

LIST OF FIGURES

Figure

ABSTRACT

With the emergence of complex architectures in modern electronics such as multi-chip modules, the increasing electromagnetic cross-talk in the circuitry causes a serious issue for high-speed, reliable data transfer among the chips. This thesis aims at developing a cross-talk resilient communication technology by utilizing a special form of electromagnetic mode, called spoof surface plasmon polariton for information transfer. The technique is based on the fact that a metal wire with periodic sub-wavelength patterns can support propagation of confined electromagnetic mode, which can suppress cross-talk noise among the adjacent channels; and thus outperform conventional electrical interconnects in a parallel, high channel density data-bus. My developed model shows that, with 1 THz carrier frequency, the optimal design of cross-talk resilient spoof plasmon data-bus would allow each channel to support as high as 300 Gbps data, the bandwidth density can reach 1 Tbps per millimeter width of data-bus, and the digital pulse modulated carrier can travel more than 5 mm distance on the substrate.

I have demonstrated that spoof plasmonic interconnects, comprised of patterned metallic conductors, can simultaneously accommodate electronic TEM mode, which is superior in cross-talk suppression at low-frequencies; and spoof plasmon mode, which is superior at high-frequencies. The research work is divided into two complementary parts: developing a theory for electromagnetic property analysis of spoof plasmon waveguide, and manipulating these properties for high speed data transfer. Based on the theory developed, I investigated the complex interplay among various figure-of-merits of data transfer in spoof plasmonics, such as bandwidth density, propagation

loss, thermal noise, speed of modulation etc. My developed model predicts that, with the availability of 1 THz carrier, the bit-error-rate of spoof plasmon data bus, subjected to thermal noise would be $\sim 10^{-8}$ while the Shannon information capacity of the bus would be 10 Tbps/mm. The model also predicts that, by proper designing of modulator, it can be possible to alter the transmission property of the waveguide over one-fifth (1/5) of the spoof plasmon band which spans from DC frequency to the frequency of spoof plasmon resonance. To exemplify, if the spoof plasmon resonance is set at 1 THz, then we can achieve more than 200 Gbps speed of modulation with very high extinction ratio, assuming the switching latency of the transistors at our disposal is negligible to the time-resolution of interest. We envision spoof plasmonic interconnect to constitute the next generation communication technology that will be transfering data at hundreds of Gigabit per second (Gbps) speed among different chips on a multi-chip module (MCM) carrier or system-on-chip (SoC) packaging.

CHAPTER I

In Quest of a New Interconnect Technology

1.1 What kind of interconnect is pertained to the thesis?

Interconnect technologies used in digital systems have primarily emerged from two opposite ends of the electromagnetic (EM) spectrum (*Karkar et al.* (2016); *Michel and Kimerling* (2007); *Urino et al.* (2011)). In the electronic side of the spectrum, copper wires are employed to transfer data at the rate of nearly Giga-bits per second (Gbps). On the other hand, in the photonic side of the EM spectrum, optical interconnect technology having a wavelength of 1.55 μm (i.e., $\sim$ 200 THz) is used for communication between circuit boards and racks in large digital systems by deploying photons to transfer data at a much higher rate (*Haurylau et al.* (2006); *Keiser* (2003); *Essiambre et al.* (2010); *Lim et al.* (2014)).

The two interconnect technologies, namely electrical and optical ones; rely on two different mechanisms of guiding electromagnetic mode through the channel. Electrical interconnects confines electromagnetic mode by setting a pair of conductors: each conductor carries equal current with opposite phase. As long as the spacing between the conductors is much smaller than the wavelength, the pair of wires guide electromagnetic wave along the longitudinal direction with negligible radiation to the surroundings. Optical interconnect, on the other hand, guides electromagnetic mode by using the difference of refractive index of the channel material with respect to its

surroundings.

In this thesis, I shall introduce a new way of information transfer that relies on a very different mechanism of guiding electromagnetic mode. This mechanism neither requires multiple conductors for signal transfer, nor does it require material with high refractive index for waveguiding. It rather employs a series of periodic resonators along the channel, which help to confine electromagnetic mode on the surface of the channel, and guide along the longitudinal direction. The channel is essentially a single-conductor metallic wire, whose surface is judiciously patterned to create periodic resonators. The confined electromagnetic mode on the surface of the channel coupled with the resonating mode has got a fancy name: spoof surface plasmon polariton (SSPP). Accordingly, I shall call this new class of channel as SSPP interconnect or spoof plasmon interconnect, interchangeably, and delve into a detail discussion on its information transfer capacity.

Designer Surface Plasmon, or Spoof Surface Plasmon was first introduced by J. B. Pendry in 2004, and later on researchers across the globe has employed this particular electromagnetic mode for various purpose: such as sensor with ultra-sensitivity, optical filters, etc. However, there is little to no discussion on the potential of spoof plasmon mode as a means of information transfer. This thesis, to my best knowledge, is the first, comprehensive account of the ability of the data transfer of SSPP waveguide. In particular, I shall discuss how much bandwidth we can extract out of SSPP channels, how far a spectral band can traverse through the channel, how close we can place the channel while keeping the cross-talk minimal, how much thermal noise should we expect out of the channel, how fast shall we be able to modulate the SSPP signal, so on and so forth.

However, from an engineering point-of-view, it is very reasonable to ask that why we do require a new kind of interconnect. In other words, what kind of advantage will this new class of interconnect bring into the table that the conventional interconnect

technologies would fall short of delivering? To answer that question, we need to understand the shortcomings of short-distance, chip-to-chip interconnects of standard technologies. The following is an account of the same.

1.2 Scaling issue of system level interconnect

Over the past decade, we have seen an exponential growth of IC speed and integration levels, as the IC fabrication technology, coupled with aggressive circuit design, have advanced significantly. In order to get the benefit of the improvement of the chip level speed at the overall system performance, the communication bandwidth among different ICs and sub-systems must scale accordingly. Currently, communication links in various applications approach Gbps data rates. These applications include computer-to-peripheral connections, local area networks, memory buses, and multiprocessor interconnection networks. Figure 1.1a and 1.1b shows the cross-section of Integrated Circuit (IC) modules on board to reveal the wire pitch of different levels of interconnects.

Board based interconnects have been used for relatively long range interconnects ($\sim 30 - 100$ cm) between modules. Unfortunately, the increases in the bandwidth of system level interconnect do not scale at the same rate as on-chip core frequencies (*Horowitz et al.* (1998)). This is primarily because of the inherent limit of the minimum channel pitch achievable on the motherboard. For instance, high density differential stripline pair has typically pitch around ~ 500 μm. Therefore, with 10 Gbps channel data rate, the maximum bandwidth density that we can achieve on board based interconnect is in the ballpark of ~ 15 Gbps/mm. Figure 1.2, reproduced from *Yamada et al.* (2013), shows the trend in the wire/pad pitch of the VLSI technology at different levels of interconnects, where wire pitch is defined as the spacing between neighboring interconnects. It is evident that for on-chip interconnects, the wire pitch is being scaled down by a factor of 2 every 6 years, whereas the pad

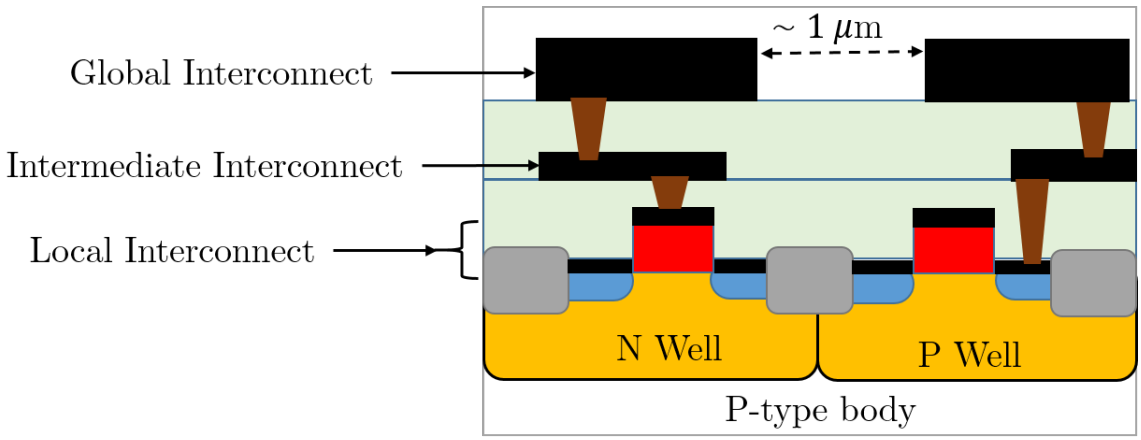

(a) Chip level interconnects

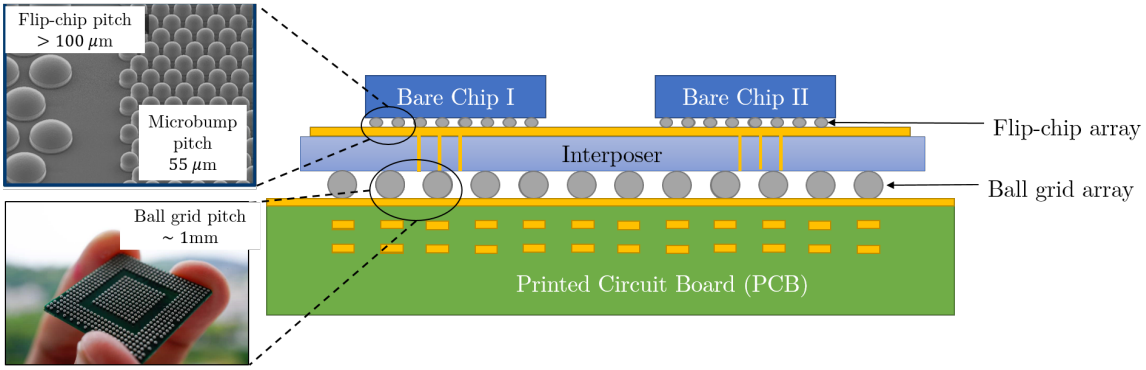

(b) System level interconnects

Figure 1.1: Cross-section of VLSI system, showing interconnects at its various levels

pitch on the PCB has barely scaled for the last few years.

Apparently, there are two ways of increasing the bandwidth of system level interconnects to keep pace with the speed improvement of on-chip interconnect. One way is to increase the pin-count of IC package to scale up the data throughput of the package. The main problem is that simply adding pins to an off-chip bus does not necessarily increase the throughput in a linear manner (*Note* (2003)). As pins are added to a package to increase the bus size and throughput, the noise induced by the signals that are simultaneously switching leads to a significant increase in noise. This means that as signals are added, the per-pin datarate of each pin needs to be decreased to meet the system noise limits. As a result, the overall throughput of an

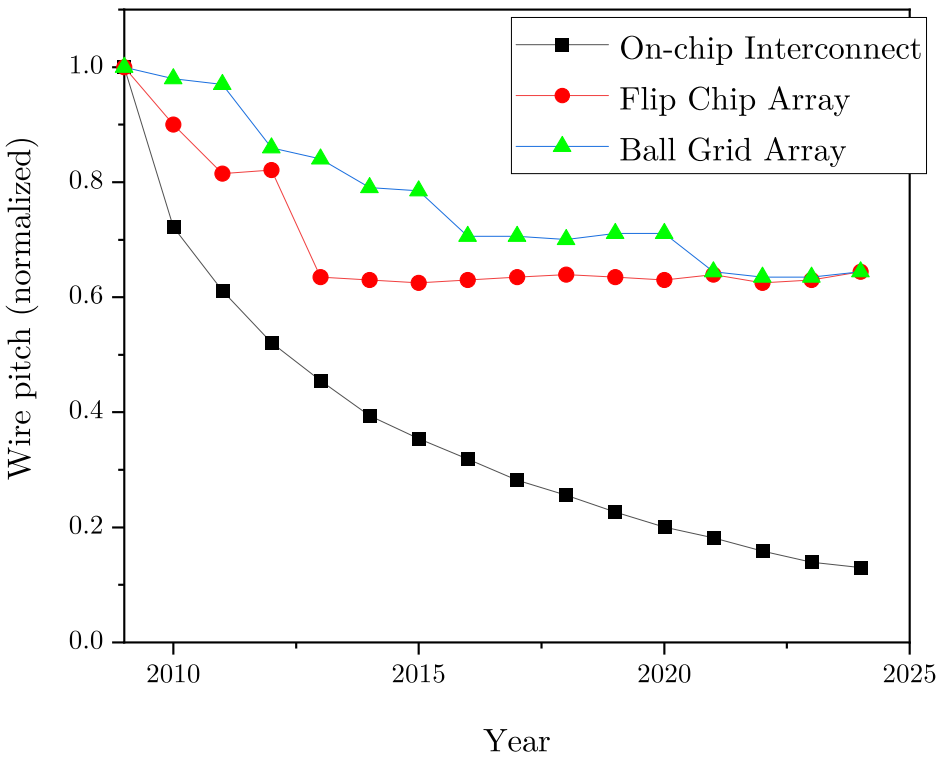

Figure 1.2: Trend of wire pitch/pad pitch at different levels of interconnect, reproduced from *Yamada et al.* (2013)

off-chip bus approaches an asymptotic limit as signals are added (*Duan et al.* (2010)).

Wide parallel busses undergo several signal integrity issues associated with simultaneous switching of digital signals (*Casper et al.* (2002); *Kim et al.* (2003)). The noise induced in the package is proportional to the number of off-chip signals that are switching simultaneously. The other possible option of increasing throughput of system level interconnect is to drive each pin at higher data-rate, or to deploy the mechanism signal modulation, coupled with frequency division multiplexing (FDM) so that each physical channel on the system level can support multiple virtual channels. The problem of this approach is that, the electromagnetic coupling among the adjacent wires at the elevated frequencies would be too high to maintain signal integrity. One solution to this problem is to increase the number of power and ground

pins in the bus configuration so that they can provide electromagnetic shield between two nearby channels. For instance, PCI-express data bus, which is a successor of PCI parallel bus intersperses ground pins more frequently among the I/O data pins in order to facilitate at least an order of increase in the speed of data transfer with high signal fidelity. Figure 1.3b shows the connector pin-out from $18 - 32$ pins of PCI-express x4 data bus, where we can see that each differential pair of input and output channel is shielded by two ground pins (one on each side of the channel) to maintain signal integrity. However, inclusion of more ground pins among the data-bus increases the cost of the package because the number of I/O pins increases.

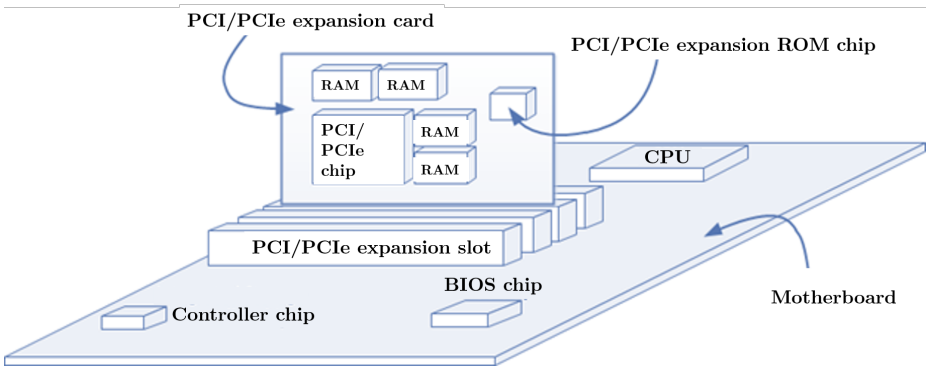

(a)

Pin number	Side B	Side A	Description
18	Ground	Ground	
19	HSOp(1)	Reserved	Transmitter Lane 1, differential pair
20	HSOn(1)	Ground	
21	Ground	HSIp(1)	Receiver Lane 1, differential pair
22	Ground	HSIn(1)	
23	HSOp(2)	Ground	Transmitter Lane 2, differential pair
24	HSOn(2)	Ground	
25	Ground	HSIp(2)	Receiver Lane 2, differential pair
26	Ground	HSIn(2)	
27	HSOp(3)	Ground	Transmitter Lane 3, differential pair
28	HSOn(3)	Ground	
29	Ground	HSIp(3)	Receiver Lane 3, differential pair
30	PWRBRK	HSIn(3)	
31	PRSNT2	Ground	
32	Ground	Reserved	

(b)

Figure 1.3: (a) Illustration of an exemplary parallel bus (PCI module expansion) on motherboard, (b) I/O Pin-out configuration of PCIe-x4 data bus, showing frequent use of ground pins to prevent cross-talk among data bus

Among the existing technology of parallel busses are (*Casper et al.* (2002)) Rapid I/O, PCI Express, and Hyper Transport. The factors that causes an upper limit of

the information transfer capacity of parallel data-bus are: propagation loss in the channel due to channel resistance, channel latency (i.e., minimum rise/fall time of signal at the channel terminal) due to electrical capacitance, noise (such as thermal and flicker noise), and cross-talk due to electromagnetic coupling among adjacent channels. Among them, the resistance derives from the material property, specifically from the conductivity of metal. Whereas cross-talk mostly owes to the geometry/ layout of the wires. If the metal traces are assumed to be almost ideal (i.e., metal with very large conductivity), then the propagation loss as well as channel latency would be insignificant. Under such condition, a standalone channel would have infinite bandwidth. The only limiting factor for information transfer would then be the cross-talk among neighbor wires in the bus. This is where we may want to replace conventional ground-associated electrical interconnect bus by spoof plasmon interconnect bus. Spoof plasmon interconnect does not require any additional ground wire for electromagnetic shielding. Rather, spoof plasmon mode has an auto-immunity to cross-talk at frequencies close to the spoof plasmon resonance. The resonant frequency can be tailored by appropriate patterning on the metallic wire, and thus are at the disposal of designer's choice.

Readers may wonder as why we have not yet discussed about the possibility of optical interconnect as an alternative for short distance communication? The next section is an endeavor to address the issue with optical interconnect implementation for short distance coverage.

1.3 Why don't we just use optical interconnects all-through?

By now, we have argued how cross-talk among the channels in data-bus can become the ultimate limiting factor in achieving high bandwidth density, given the fact that electrical wires succumbs to electromagnetic interferences as we move towards higher frequencies. This may ignite the thought of replacing electrical data-bus by

optical data-bus, since optical waveguides suppresses cross-talk at high frequencies: an opposite trend of electromagnetic interferences with frequencies compared to that of electrical ones. While optical data bus can indeed outperform electrical data-bus in terms of dealing with cross-talk, it comes with a price: optical waveguides always requires sources of carrier frequency, modulators, and demodulators, which add to the overhead energy budget of information transfer. Usage of a given interconnect technology over the other alternatives is justifiable only when the technology in question can result in the minimum energy consumption for per bit of transferred data. Therefore, unless the rate of data-transfer exceeds a threshold value, optical interconnects gives in to its electrical counterpart in the ability of data transfer. It turns out that, for short-range interconnects, the rate of data-traffic in a channel may vary in such a wide range over time that employing an optical interconnect may often remain underutilized of its full capacity of information transfer, and therefore cost unnecessary loss of energy attributed to its overhead power budget.

Because of the above mentioned system complexity and overhead cost, fiber-optic communication systems couldn't make their niche in short distance communication. They have primarily been installed in long-distance applications, where they can be used to their full transmission capacity, offsetting the set-up cost. Finally, plasmonic interconnects, which grabbed researchers' interest over last decades due to their ability of subwavelength confinement, are plagued with metallic losses and the high attenuation factor limits the signal propagation length within few microns [26]–[28].

1.4 Appreciating the complexity of data transfer

We identify two key features prevailing in inter-chip communications:

- Centimeter scale distance is the most critical range of communication, where no single means of standard communication (between electronics and optics)

stands out to be distinguishingly superior to the other.

- The nature of data-traffic rate statistically varies from time to time rather than being constant. Hence, any fixed mode of the communication link for centimeter scale distance of coverage may run the risk of remaining largely under-utilized or over-utilized for most of the time, resulting in a severe strain on energy dissipation.

1.4.1 Time variation in data-traffic: a dilemma in selecting interconnect technology

The dilemma in the selection of interconnect for energy economization becomes obvious once we consider the time-dependent statistical nature of the volume of data traffic. Traffic can be characterized assuming that the packet arrivals obey the Poisson distribution. For example, at IT datacenters, it witnesses a large temporal variation of data-flow over the course of a day (*Heller et al.* (2010)). The time variation of traffic gets even more prominent as we move down the network hierarchy: from data-center core to the individual user terminals. Benson, et al. (*Benson et al.* (2010)) showed that link utilization is one-fourth in the terminal layer than in the core layer, with the full utilization not exceeding 10%. Because of the temporal distribution of data-traffic, especially at the range of centimeter scale interconnect length on the board-level, it is most difficult to choose an optimum interconnect technology that can ensure full utilization of link capacity and minimize energy cost for a highly random volume of data flow. This is why, it would be immensely beneficial to overcome the 'last centimeter interconnect barrier' by a technology that, rather than supporting a fixed mode, can alternate between two different modes of communication.

1.5 Do we have any alternative interconnect technology in hand?

As discussed in the preceding sections, there remains a range of distance of 0.1 – 10 cm, dubbed as the 'last centimeter barrier', where state-of-the-art interconnect technologies compromise on critical performance metrics such as bandwidth and energy efficiency (*Gu* (2015)). The unresolved challenges in short-range communications between integrated circuits (ICs), therefore, warrant discoveries of new interconnect technologies having ultrafast data transfer rate, high energy-efficiency, and compatibility with CMOS technology (*Owens et al.* (2007); *Saraswat and Mohammadi* (1982); *Mui et al.* (2004)). As shown in Fig. **??**, in between the EM spectral ranges for electronic and optical technologies, an emerging Terahertz regime (0.1-10 THz) in the underexploited and underutilized EM spectral band is now garnering attention for wired and wireless communication systems (*Chamberlain* (2004); *Sirtori* (2002); *Han and Afshari* (2015); *Saeedkia* (2013); *Kleine-Ostmann and Nagatsuma* (2011)).

1.6 Spoof plasmon interconnect: a new paradigm in communication technology

In the framework of the current thesis, I have investigated the concept of implementing a communication network that can transfer information by a new type of particle, called spoof surface plasmon polariton (SSPP) (Fig. 1.4) for the future high-speed data transfer between integrated circuit (IC) chips overcoming the limitations of state-of-the-art interconnects. Spoof surface plasmon polariton (SSPP) is a special, surface-bound electromagnetic wave in patterned metal (*Pendry et al.* (2004a); *Erementchouk et al.* (2016a)). It may be noted that the precursor of spoof plasmon technology was surface plasmon polariton (SPP) or plasmonic mode of signal

propagation in the optical and near-infrared frequency range (300 THz –800 THz). Researchers in materials science and physics have concluded that plasmonics or SPP was not suitable for chip-scale interconnect technology because of accompanying high signal attenuation. The thesis does not discuss SPP or plasmonic modes. SSPP waves are strongly confined subwavelength modes (*Pendry et al.* (2004b)), therefore the parallel data bus of SSPP can be densely packed, and data can be safeguarded from crosstalk interferences.

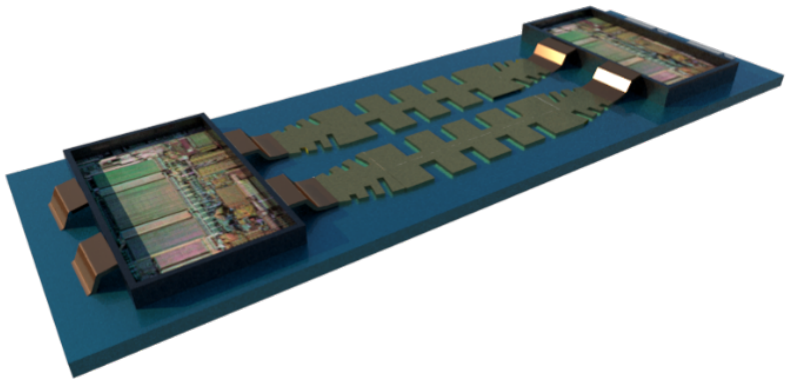

Figure 1.4: An inter-chip communication network employing SSPP channels. The typical free space wavelength corresponding to spoof plasmon resonance is 300 microns.

In addition, SSPP modes can propagate considerable distance (a few centimeters) [30] by circumventing ohmic loss resulted from penetration of the mode into the metal. On one hand, SSPP interconnect possesses the advantage of CMOS compatibility (*Liang et al.* (2016)) and its energy-economic quasi-electrical mode can transfer data without requiring excessive energy. On the other hand, its quasi-optical mode with deep subwavelength confinement can provide high bandwidth overcoming the conventional 1/RC-limit. In my research, I showed that spoof-plasmon based data bus can provide nearly 300 Gbps data transfer rate per channel with 1 Tbps/mm bandwidth density, while the signal can propagate up to a wire length of 1 centimeter (cm) (*Joy et al.* (2019)). These results indicate a remarkable potential of SSPP

interconnects for becoming the most viable technology for the next generation high-speed inter-chip short-range communications.

1.7 Research on spoof plasmon wave: towards CMOS compatibility

Spoof plasmon wave has become a new exciting field of research (*Rusina et al.* (2010a); *Kats et al.* (2011); *Garcia-Vidal et al.* (2005a); *Shen et al.* (2008); *Yu et al.* (2010); *Ma et al.* (2014)) and my research group, led by Professor P. Mazumder has made significant contributions to the theory and applications of SSPP based systems (*Xu et al.* (2012a); *Erementchouk et al.* (2016a); *Song and Mazumder* (2009); *Xu and Mazumder* (2012); *Song and Mazumder* (2013, 2011); *Zheng et al.* (2013); *Song and Mazumder* (2012); *Aghadjani et al.* (2016); *Joy et al.* (2017)). Pioneered by Sir John Pendry's group at the Imperial College, UK (*Pendry et al.* (2004a); *Pors et al.* (2012)), several researchers such as Stefan Maier at Imperial College, UK (*Maier et al.* (2006b); *Liao et al.* (2015); *Fernandez-Dominguez et al.* (2008); *Gu et al.* (2012)), Federico Capasso at Harvard University, USA (*Kats et al.* (2011); *Yu et al.* (2010); *Woolf et al.* (2014)), Harry Atwater at California Institute of Technology, USA (*Brar et al.* (2013)), Tei Cui at Southeast University, China (*Liang et al.* (2016); *Ma et al.* (2014); *Shen et al.* (2013a); *Gao and Cui* (2015)), Pinaki Mazumder at University of Michigan, USA (*Erementchouk et al.* (2016a); *Song and Mazumder* (2009); *Aghadjani et al.* (2016); *Joy et al.* (2017)), and Hao Yu at Nanyang Technological University, Singapore (*Liang et al.* (2016, 2015a,b)) have advanced the field of THz surface-wave engineering.

Starting from large 2D periodic hollow metal structure proposed by Pendry in 2004 (*Pendry et al.* (2004a)), THz SSPP morphed to 1D corrugated structures by the work of Garcia-Vidal in 2005 (*Garcia-Vidal et al.* (2005a))(on rectangular

SSPP structures) and Maier in 2006 (on cylindrical SSPP structures) (*Maier et al.* (2006a)). Subsequently, single-sided SSPP structure was designed by Moreno in 2010 (*Martin-Cano et al.* (2010)) and double-sided SSPP structure was introduced by Mazumder in 2012 (*Xu et al.* (2012b)) to increase the length of signal propagation with low attenuation. In order to adapt the spoof THz surface wave technology (SSPP) to thin-film interconnect technology, Mazumder and Yu (2017) fabricated surface-wave based structures on silicon substrate using commercial 65 nm CMOS technology (*Liang et al.* (2016); *Joy et al.* (2019)). Their work has now opened a greater opportunity to improve the bandwidth of the interconnect technology by an order of magnitude, while making THz surface-wave propagation on SSPP structure compatible with commercial CMOS technology.

1.8 Organization of the Work

In the next few chapters, I shall describe the mechanism and the different components required for information transfer through spoof surface plasmon polariton interconnects, and demonstrate why such kind of interconnects can constitute a augmented way of data transfer. In broad sense, the description of the SSPP based data transfer is divided into the following segments.

- Electromagnetic analysis of spoof plasmon mode
- Information Capacity and noise analysis of spoof plasmon interconnects
- High speed modulation technique in spoof plasmon waveguide
- Recuperation of signal quality in non-ideal spoof plasmon interconnects

CHAPTER II

Electromagnetics of Spoof Plasmon Mode

2.1 Introduction

Spoof surface plasmon polariton (SSPP) is an exotic electromagnetic state that confines light at a subwavelength scale at a design-specific frequency. In this chapter, the electromagnetic states of SSPP mode are analyzed systematically based on the transfer matrix formalism. Within this approach, systems with arbitrary transversal structure can be investigated in a straightforward manner. A general expression for the dispersion relation of SSPP waveguide is established. The results of the general analysis are applied for studying the effect of dielectric environment on SSPP spectra.

It has been known for a while that spoof plasmon mode can exist in planar, thin structures with dispersion properties similar to that of its wide three dimensional structure counterpart. I, however, have shown that spoof plasmons in thin structures possess some unique properties that has remained unexplored so far. My analysis reveals that the field interior to SSPP waveguide can achieve an exceptional hyperbolic spatial dependence, which can explain why spoof plasma resonance incurs red-shift with the reduction of the waveguide thickness, whereas common wisdom suggests frequency blue-shift of a resonant structure with its size reduction. In addition, I show that strong confinement can be achieved over a wide band in thin spoof plasmon structure, ranging from the spoof plasma frequency up to a lower frequency consider-

ably away from the resonant point. The nature of lateral confinement in thin SSPP structures may enable interesting applications involving fast modulation rate due to enhanced sensitivity of optical modes without compromising modal confinement.

2.2 Origin of the name: analogy with real plasmon

The concept and application of propagation of electromagnetic waves near periodically corrugated conducting surface has attracted attention since the 1940s in the context of slow waves (*Brillouin* (1948); *Chu and Hansen* (1947)). Now-a-days, scattering of electromagnetic waves on a corrugated surface of a perfect electric conductor is one of the standard topics of textbooks on electromagnetic theory. The situation has changed recently when a deep analogy between the field states and plasmons in metals has been recognized (*Pendry et al.* (2004a); *Hibbins et al.* (2005)). The grooves in the conductor, in structures similar to those shown in Fig. 2.1a play the role of cavities holding most of the field in the slow wave regime. As a result, while there is no true penetration into the material, the field is contained beneath the surface covering the structure mimicking such penetration. Moreover, near frequencies corresponding to the quarter-wavelength resonance of the grooves, the response of the patterned metal to the incident electromagnetic waves can be approximately described with the help of an effective Drude model (*Pendry et al.* (2004a); *Erementchouk et al.* (2016a)) with the plasma frequency,

$$\omega_p = \frac{\pi c}{2h} \tag{2.1}$$

Owing to such resemblance of the behaviour of true plasmon polaritons in metals, the states of the electromagnetic field confined to the corrugated surface of a perfect conductor were dubbed spoof surface plasmon polaritons (SSPP).

It should be noted, however, that the relationship between the effective plasma frequency and the parameters of the surface obtained in Eq. 2.1 is specific for the

quasi-one-dimensional geometry, when the structure has well-defined hierarchy of sizes (along x-, y- and z-axes). In the two-dimensional case, where grooves have the form of cylinders, the SSPP effective plasma frequency is determined by the optical radius of the grooves (*Garcia-Vidal et al.* (2005a); *Maier et al.* (2006a)) and in order to reach the regime with well-formed SSPP, it is necessary to fill grooves with a dielectric with high refractive index. Mimicking plasmon features without penetrating into material generated a significant interest in SSPP. With the help of spoof plasmons, it becomes possible to employ various plasmon-like effects, for instance, field confinement and field enhancement, at low frequencies (such as Terahertz and microwave), where true plasmons can barely exist.

2.3 Literature Review: research in spoof plasmonics

Surface plasmon resonance (*Barnes et al.* (2003b)) in metals has triggered a number of exciting applications (*Homola* (2003); *Pillai et al.* (2007); *Mulvaney* (1996); *Willets and Duyne* (2007); *Yang et al.* (2015); *Liu et al.* (2017b); *Anwar et al.* (2018); *Chen* (2016)), due to its ability to push the conventional boundary of resolution beyond the Abbe diffraction limit (*Zhang and Liu* (2008)). However, surface plasmon has also got its own limitations as well. The operating frequency is dependent on the electron density in metal which is pretty much determined by nature. In addition, there is an inherent trade-off between scaling down the optical mode volume and its loss in metal (*Chang et al.* (2011); *Ambati et al.* (2008)). The seminal paper authored by Pendry and co-workers (*Pendry et al.* (2004b); *Garcia-Vidal et al.* (2005b)) introduced the very idea of spoof surface plasmon polariton (SSPP), where the artificial plasma frequency became design-specific, and the modal size can be squeezed below diffraction while the electromagnetic field does not penetrate into the metal. Thus, in principle we can achieve subwavelength confinement in SSPP at whatever frequency we demand without incurring any Ohmic loss.

Albeit deemed as a brilliant solution, the very large cross-sectional size (ideally infinite) of the metamaterial (see Fig. 2.1a) as originally proposed makes the 3D structure unwieldy to fabricate and harness in engineering applications, such as - data processing and routing. In 2013, Shen et al. (*Shen et al.* (2013b); *Shen and Jun Cui* (2013)) showed that the SSPP mode is supported even by an ultra-thin film structure with a thickness 600 folds smaller than its operating wavelength. This discovery immediately broadened the scope of constructing truly sub-wavelength structure which can be bent and twisted to allow the signal routing in a flexible way (*Ma et al.* (2014)). Yu et. al. demonstrated that sub-wavelength size standalone interconnect can be implemented in thin, planar CMOS compatible SSPP metamaterial to operate at sub-THz range having strong immunity to interference (*Liang et al.* (2015b); **?**); **?**). This unravels the potential of the SSPP interconnect to serve as a reliable way of transferring data at THz speed with reduced crosstalk.

2.4 Author's contribution in electrodynamics of spoof plasmon

In order to appreciate the novel contribution made by this current work in the field of electrodynamics of spoof plasmon, it is necessary to identify the prior work in this context and their limitation: especially in the description of spoof plasmon mode in a waveguide of finite cross-section. Based on the argument of conservation of field polarization, it was hypothesized that (*Shen et al.* (2013b)), even in thin structures, the main characteristics of SSPP metamaterial with infinite thickness are retained, and hence the standard theory for spoof plasmon (*Kats et al.* (2011); *Woolf et al.* (2014); *Song and Mazumder* (2009); *Xu et al.* (2012b); *Chen* (2016)), originally derived for 3D structure, requires no revision. Because of the apparent resemblance between the dispersion behavior of a 3D SSPP structure and that of its 2D planar counter-

part, it was deemed redundant to perform an exclusive analysis of the planar SSPP structure. My objective in this chapter is to develop a complete theory explaining the optical characteristics of SSPP mode in planar structure coupled with its environment including the substrate underneath. It may be noted that Liu et al. (*Liu et al.* (2013)) performed numerical simulations to study the effect of SSPP thickness on dispersion as shown in (*Yang et al.* (2017)) and the impact of substrate on SSPP mode was characterized by introducing an effective permittivity term ϵ_{eff}. However, a quantitative analysis of a planar structure is needed to explain the counter-intuitive red-shift occurrence in the SSPP waveguide with the reduction of the thickness of SSPP at a given propagation constant (β). Wan and Cui in (*Wan and Cui* (2014)) presented a theoretical analysis of spoof plasmon in thin structures. Their analysis, however, does not predict any frequency shift or field confinement in the lower region of the SSPP band, although in practice the whole band undergoes red shift with reduction of SSPP thickness as established through experimental measurement (*Shen et al.* (2013b); **?**); **?**) as well as COMSOL simulation. In addition to explaining this anomaly, my analysis also shows that a field confinement is achieved at any non-zero frequency on the lateral wall of SSPP even at a frequency away from the spoof plasma resonance. In other words, subwavelength confinement in planar SSPP can be a broadband phenomenon contrary to the common notion of resonance-based narrow-band confinement (*Luo et al.* (2016); *Liu et al.* (2017a)). In this chapter, I introduce the idea of effective thickness of SSPP mode in an ultra-thin structure, which offers an intuitive view of why spoof plasma mode exists even in the limit of vanishing metal thickness. I also provide a quantitative analysis of the ultra-thin structure using the proposed effective thickness model which agrees with 3D simulation results.

This work endeavors to make both intuitive and quantitative analysis of spoof plasmon mode in planar structures. The following sections discuss a theory which shows that for an SSPP waveguide surrounded by dielectric on each of its lateral

side, an imaginary wave-vector $P = i\delta_P$ describes the mode profile along lateral direction. This unusual cross-sectional mode with hyperbolic profile explains why the operating frequency at a given propagation constant makes redshift with the thickness reduction, which is quite contrary to a conventional structure where frequency scales inversely with size. I also discuss an interesting concept of effective thickness t_{eff} of SSPP groove to explain why we retain a solution of SSPP mode even in the limit of vanishing metal thickness. A useful contribution of this work is the analysis of the effective refractive index $n_{g,eff}$ of the groove, which takes into account both the geometry of the waveguide and the environment outside of it on governing its dispersion relation. These parameters simplify other analyses relevant to the design of bandwidth-efficient SSPP data buses, and estimation of bandwidth modulation rate with the change in the external environment.

2.5 Modal Analysis of Spoof Plasmon

2.5.1 Dispersion relation in wide structures

The distribution of the field across a periodic structure is conveniently described within formalism of the transversal transfer matrix when the field is represented as a superposition of upward and downward propagating waves with transfer matrices relating amplitudes in different regions. The developed formalism is directly applied for finding dispersion law governing states of the field confined to the corrugated surface, spoof surface plasmon polaritons (SSPP). The dispersion law is obtained by requiring that the transfer matrix must map state vector corresponding to the boundary condition at one point, say, $|\alpha_L\rangle$ at the lower end, into a state vector corresponding to the condition at the opposite point, say, $|\alpha_U\rangle$. Explicitly, this condition is written as

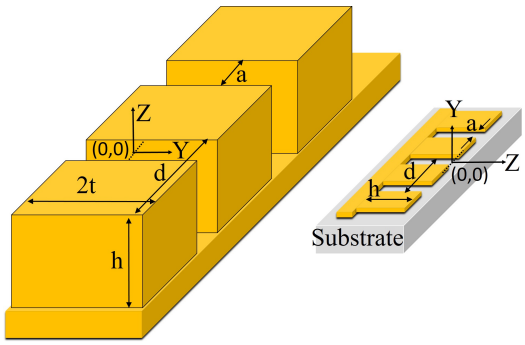

(a)

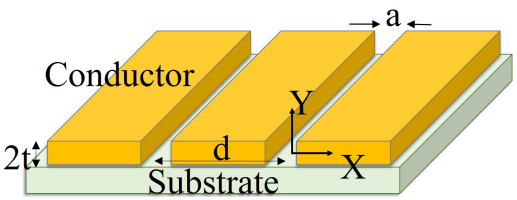

(b)

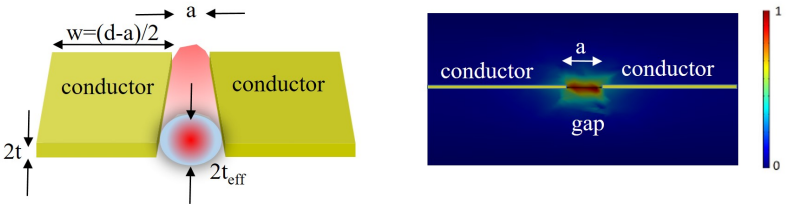

(c)

Figure 2.1: (a)schematics of a 3D SSPP structure standing alone and a 2D SSPP structure on substrate. (b)Planar SSPP seen from a lateral viewpoint. The groove is very long along z direction. (c) [left]Illustration of effective thickness of SSPP groove. The optical mode formed between the pair of conductors extends beyond the physical thickness of metal. [right] 3D simulation result of the mode formation inside the groove, justifying the concept of effective thickness.

$$D(\omega, \beta) \equiv \langle \alpha_U^{\perp} | \mathcal{T} | \alpha_L \rangle = 0 \tag{2.2}$$

where $|\alpha_U^{\perp}\rangle$ is an element of space defined by $\langle \alpha_U^{\perp} | \alpha_U \rangle = 0$. It can be shown that, the dispersion relation, when written in terms of the spoof plasmon waveguide geometry with one-dimensional periodic grooves of quarter-wavelength height (h), yields the following,

$$D(\omega, \beta) = \cos(Q_0 h) - \eta \frac{Q_0}{\kappa_0} \sin(Q_0 h) = 0 \tag{2.3}$$

where Q_0 is the zeroth order wave-vector inside the groove along the direction of its height, $\kappa_0^2 = \beta^2 - Q_0^2$, where β is the propagation wave-vector of spoof plasmon mode. Taking higher order bloch-modes into account, the coupling co-efficient η can be shown to be

$$\eta \approx \frac{a}{d} \Big[\operatorname{sinc}^2(\frac{a\beta}{2}) + \frac{\kappa_0 d}{\pi} \Big(\frac{3}{2} - \ln(\frac{2\pi a}{d}) \Big) \Big] \tag{2.4}$$

The second term in the braces, deviating from the approximation routinely used in studies of SSPP in periodically corrugated structures, $\eta_{SMA} = \frac{a}{d} \operatorname{sinc}^2(\frac{a\beta}{2})$, accounts for the effect of multiple Bloch modes.

2.5.2 Impact of dielectric half-space on dispersion

We start by considering the case when the interior of the grooves of a half-closed waveguide and the outside space are filled with materials with different dielectric constants, ϵ_g and ϵ_a, respectively (figure 6a). The mismatch between ϵ_g and ϵ_a leads to modification of the interface transfer matrix. It has been shown by our group that,in this case the SSPP dispersion equation has the same general form as for a dielectrically homogeneous environment

$$\cos(Qh) - \eta(\epsilon_a)\frac{Q^2(\epsilon_a)}{Q^2(\epsilon_g)}\frac{Q(\epsilon_g)}{\kappa(\epsilon_a)}\sin(Qh) = 0 \tag{2.5}$$

Changes induced by the dielectric environment in this case are quite straightforward. We discuss them in the limit $\omega \to \infty$, when after introducing $\tilde{Q} = \sqrt{\epsilon_a}\omega/c$ and $\tilde{h} = h\sqrt{\epsilon_g/\epsilon_a}$ we arrive at the same equation that governs the electromagnetic dispersion relation in an all-homogeneous-dielectric (i.e., all-air) SSPP waveguide structure with rescaled coupling parameter $\eta \to \eta\sqrt{\epsilon_a/\epsilon_g}$. Noteworthy, due to the strong attenuation of the electromagnetic field exterior to the groove in the regime of $\beta d >> \frac{\omega}{c}h$, the spoof plasmon resonance frequency $\tilde{\omega}_p$ is independent of the dielectric environment outside of the groove and is only a function of the dielectric constant of the material interior to the groove.

$$\tilde{\omega}_p = \frac{\omega_p}{\sqrt{\epsilon_g}} \tag{2.6}$$

In the case of a dielectric half-space, the dispersion relation can be characterized by the band-edge frequency $\omega_e = \tilde{\omega}_p - \Delta\omega_e(\epsilon_a, \epsilon_g)$ of the fundamental band, where

$$\Delta\omega_e(\epsilon_a, \epsilon_g) = \tilde{\omega}_p\sqrt{\frac{\epsilon_a}{\epsilon_g}}\frac{2\eta(\epsilon_a)}{\pi\sqrt{(2h/d)^2\epsilon_g/\epsilon_a - 1}} \tag{2.7}$$

Its dependence on the height of the groove is shown in Fig. 2.2 together with the results of full-wave numerical simulations. It demonstrates, in particular, that as long as the system is in the SSPP regime, $\beta\tilde{h} > \pi/2$, Eq. 2.7 agrees very well with numerical simulations.

2.5.3 Dispersion relation correction in structures of finite thickness

For the sake of simplicity, we will start our analysis for a planar (with finite thickness) corrugated metal structure with groove of infinite length, as depicted in figure 1b. This will help us isolate analysis of the mode profile in lateral plane (XY plane) and longitudinal plane (ZX plane). By the term of 'lateral' side of SSPP, we

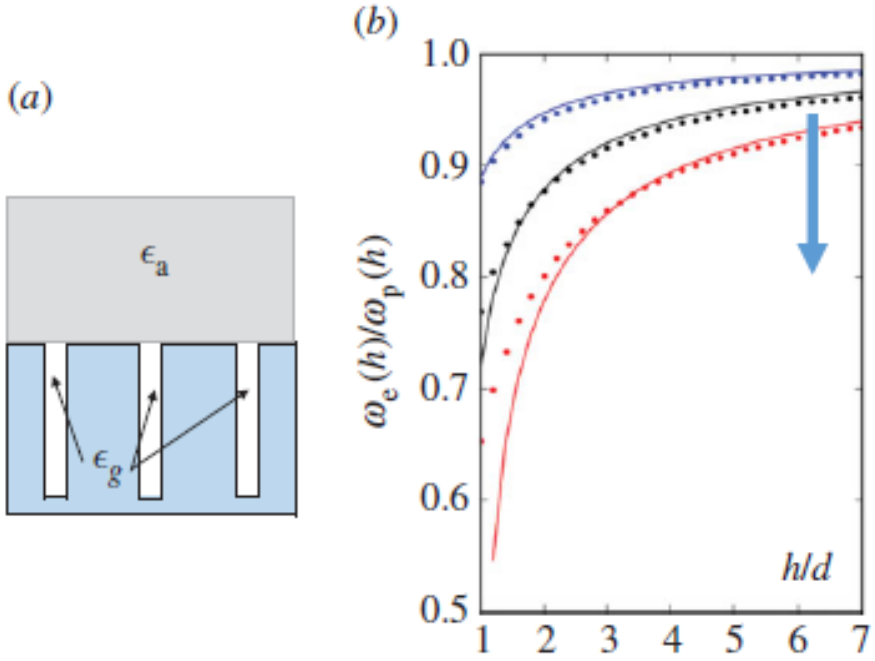

Figure 2.2: (a) The cross section of a half-closed waveguide filled by material with the dielectric function ϵ_g bounded by halfspace with the dielectric function ϵ_a. (b) The normalized position of the edge of the fundamental band $\omega_e(h)/\tilde{\omega}_p(h)$ as a function of the grooves height for different values of ϵ_a (the arrows show the variation with increasing $\epsilon_a = 1, 2.25, 4$): solid lines are obtained from Eq. 2.7, dotted lines show the results of full-wave numerical simulations.

refer to the half-space extended along Y direction exterior to the groove. This half-space is defined by $|y| > t$, where $2t$ is the thickness of the structure, the grooves are oriented along Z direction and (x, y)=(0, 0) line longitudinally bisects a groove into equal halves. Finite cross section of SSPP will induce a non-zero wavevector P along the lateral direction of the groove. We will make two alternative assumptions to analyse what sort of modification is needed to study the dispersion characteristics of an SSPP waveguide with finite thickness ($2t$).

2.5.3.1 Assumption I: absence of Ez field

The perfect electric conductor (PEC) approximation of metal at terahertz frequencies and below along with the fact that the operating wavelength is much larger than twice the groove width justifies the assumption that the electric field component E_z, because of being tangential to every point on the surface of patterned metal (including the interior wall of the grooves) vanishes on the waveguide surface and is necessarily nominal compared to the other components of electric field of SSPP mode in space. Let, $E_{g,x}$ and $E_{a,x}$ are x-components of electric field interior and exterior to the groove, respectively, and we will consider first the even mode of $E_{g,x}$ (even/odd mode is defined according to the symmetry of $E_{g,x}$ component along Y axis with its center at the middle of the groove).

$$E_{g,x} = \sum_m G_m \cos(\frac{m\pi}{a}(x - \frac{a}{2})) \cos(P_m y) e^{iQz} \tag{2.8a}$$

$$E_{a,x} = \sum_n A_n e^{i\beta_n x} e^{-\kappa_n (y-t)} e^{iQz} \tag{2.8b}$$

where Q and β are propagation wave-vector components along the groove length and waveguide's periodicity, respectively; P_m and $K_n = i\kappa_n$ are the transverse wave-vector components along Y axis describing modes at the interior and exterior to the

groove, respectively; $\epsilon_g = n_g^2\epsilon_0$ is the dielectric constant of the groove, G_m and A_n are the amplitudes of the field components in the groove and air, respectively; m, n are integers corresponding to optical modes. κ_n must have to be of real value in order to sustain guided mode. An assumption of $E_z = 0$ in addition to the divergence relation of electric field in source free region, i.e., $\nabla.\mathbf{E} = 0$ leads to the following simple expression of other field components.

$$E_y = -\int \frac{\partial E_x}{\partial x} dy \tag{2.8c}$$

$$H_z = -\frac{i}{\omega\mu}\left(\frac{\partial E_y}{\partial x} - \frac{\partial E_x}{\partial y}\right) \tag{2.8d}$$

Hence the other field components inside (outside) of the groove can be expressed in terms of the amplitude $G_m(A_n)$.

Now, matching the electric field boundary condition $E_{a,x} = E_{g,x}|_{y=t,-a/2<x<a/2}$ at the interface and taking the fact that $E_x = 0$ outside the window of $-a/2 < x < a/2$ on the interface, and also keeping the continuity condition of tangential magnetic field, it can be shown that

$$\tan(Pt) = \frac{-P}{\kappa}\frac{a}{d}\,\mathrm{sinc}^2(a\beta/2) \tag{2.9}$$

where we assumed the prevalence of $n = m = 0$ mode, and used the relation $\beta^2 - \kappa^2 + Q^2 = P^2 + Q^2 = (\frac{\omega n_g}{c})^2$; n_g being the refractive index of the material that fills the groove. It can be seen that, irrespective of the metal thickness $2t$, Eq. 2.9 is satisfied for $P = 0$, which, in turn, leads to the prediction of $Q = \frac{\omega n_g}{c}$. Thus, assumption I predicts existence of SSPP mode in structures with arbitrary thickness, however, it falls short in explaining the small shift in frequency with change of metal thickness.

Assumption II: TM mode prevalence

For a structure with thickness ($2t$), standing free in air environment, with the wave propagating along the groove's direction of periodicity (x direction), we can set $H_x = 0$ at the lower frequency regime inside the narrow groove for perfect electric conductor(PEC) boundary. Then the field components for TM mode inside the groove (E_g, H_g) and outside of it (E_a, H_a) can be written in terms of the geometric features (such as groove length, period, thickness etc) of spoof plasmon waveguides, assuming $e^{-i\omega t}$ time dependence.

Then from the condition of tangential field (i.e., E_x and H_z) continuity at the interface ($y = t$), it can be shown that,

$$P\tan(Pt) = -(\frac{\omega}{c})^2 \frac{a}{d}\,\mathrm{sinc}^2(a\beta/2)\frac{\kappa}{\beta^2 - (\omega/c)^2} \tag{2.10}$$

As we can see, because the RHS of Eq. 2.10 is a negative number for a guided mode, Pt must have to be greater than $\pi/2$ to make the LHS negative as well. This sets a lower limit on the SSPP waveguide thickness in turn. This prediction is harmonious to the result of some of the earlier attempts i.e., (*Martin-Cano et al.* (2010)) for size reduction of SSPP waveguide where structure with thickness comparable to its periodicity were considered to be the best possible solution. Interestingly, the LHS of Eq. 2.10 can also be negative for arbitrary thickness $2t$ if P assumes a small, purely imaginary value, i.e., $P = 0 + i\delta_P$, since the imaginary P yields $LHS = P\tan(Pt) \approx P^2 t = -\delta_P^2 t$ for small Pt. Then, using $(\omega/c)^2 = \frac{1}{n_g^2}(P^2 + Q^2) \approx \frac{Q^2}{n_g^2}$, we get

$$(\delta_P)^2 t \approx \frac{1}{n_g^2}\frac{a}{d}\,\mathrm{sinc}^2(a\beta/2)\frac{Q^2\sqrt{\beta^2 + Q^2(1 - \frac{1}{n_g^2})}}{\beta^2 - Q^2} \tag{2.11}$$

where $tanh(x) \approx x$ is used, and we kept our interest limited to thin groove. The corresponding frequency will be $\omega/c = \frac{1}{n_g}\sqrt{Q^2 - (\delta_P)^2} \approx \frac{1}{n_g}Q(1 - \frac{1}{2}\frac{\delta_P}{Q})$. So, the

frequency detuning due to finite size of SSPP waveguide standing free in air is $\Delta = -\frac{1}{2}\delta_P$.

For odd mode with $\sin(P_m y)$ variation of $E_{g,x}$ field, Eq. 2.10 should be replaced with the following

$$P\cot(Pt) = (\frac{\omega}{c})^2 \frac{a}{d}\operatorname{sinc}^2(a\beta/2)\frac{\kappa_0}{\beta^2 - (\omega/c)^2}$$

To determine the value of the wave-vector P, we need to know the phase factor along the groove length (i.e., wave-vector Q) for a given propagation constant β. The relation between β and Q follows from the standard theory of SSPP mode (*Song and Mazumder* (2009); *Erementchouk et al.* (2016b)) in 1-D corrugated metal structure.

$$\sqrt{\beta^2 - (\omega/c)^2} = Q\frac{a}{d}\operatorname{sinc}^2(a\beta/2)\tan(Qh) \tag{2.12}$$

For a structure of thickness $2t$ bound with metallic walls on the lateral sides, the lowest order lateral wave-vector would be $P_0 = \dfrac{\pi}{2t}$. This indicates that reduction of thickness $2t$ in such a structure would increase P which would in turn cause an increase of frequency ω (i.e., blue-shift) at a given β, as $P^2 + Q^2(\beta) = (\frac{\omega}{c})^2$. On the contrary, SSPP structures whose lateral sides have interface with dielectric show the opposite response, i.e., for a given β, the operating frequency demonstrates red-shift with the reduction of its thickness, as the wave-vector P takes an imaginary value following Eq. 2.11.

2.5.4 Effect of substrate

Usually SSPP waveguides are grown on top of a substrate such as silicon, which introduces asymmetry to the cross-section profile of the waveguide. Let us assume that, the grooves are filled with dielectric constant $\epsilon_r = \epsilon_g$, and are fabricated on substrate with $\epsilon_r = \epsilon_s$.

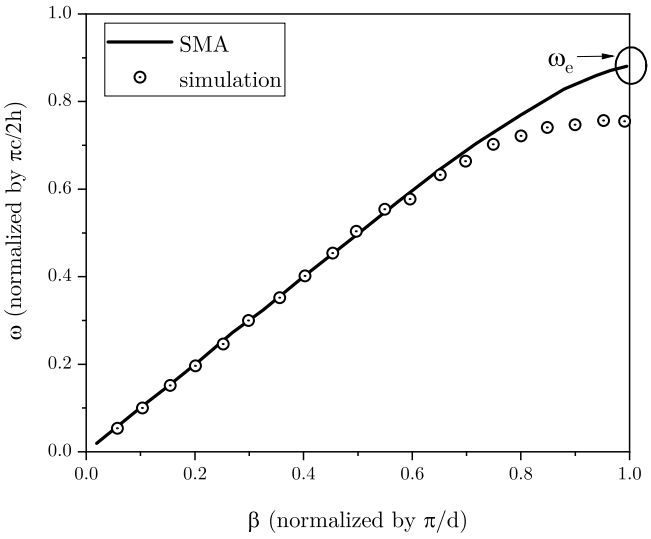

Figure 2.3: Dispersion relation in SSPP structure with infinite width. Solid lines are generated from analytical results with single mode approximation, while the dots are from 2D simulation in COMSOL Multiphysics.

Following the same strategy stated above, we obtain the following dispersion relation taking into account the presence of a substrate

$$\Big(\cos(2Pt) + S^2\frac{\kappa_a}{k_0^2-\beta^2}\sin(2Pt)\Big)\Big(\cos(2Pt) + \epsilon_r S^2\frac{\kappa_s}{k_s^2-\beta^2}\sin(2Pt)\Big) = 1 \quad (2.13)$$

where $S^2 = \dfrac{k_0^2}{P}\dfrac{a}{d}\,\mathrm{sinc}^2(a\beta/2)$, and $\epsilon_r = \frac{\epsilon_s}{\epsilon_0}$.

Also $\beta^2 + Q^2 - \kappa_a^2 = \dfrac{1}{n_g^2}(P^2+Q^2) = (\omega/c)^2 = \dfrac{1}{n_s^2}(\beta^2 + Q^2 - \kappa_s^2)$

2.5.5 Effective refractive index of a planar SSPP

In an SSPP medium with infinite lateral dimension, the propagation constant inside the groove is, $Q = \frac{\omega}{c}$. From the above analysis, we can also determine an

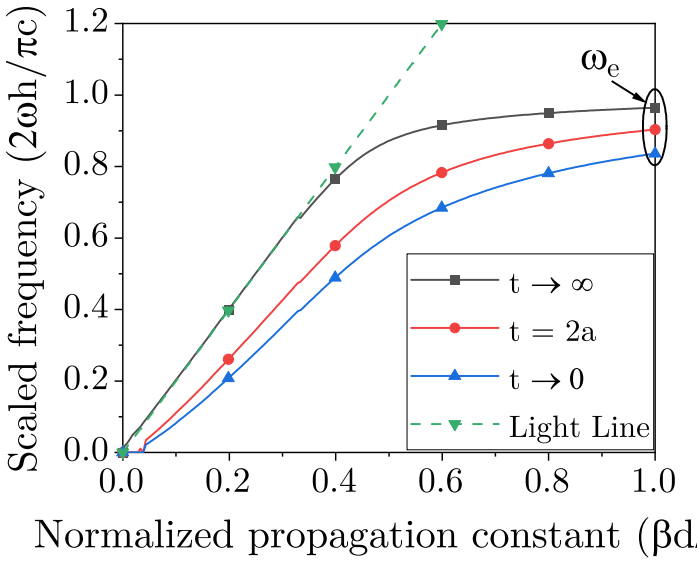

(a)

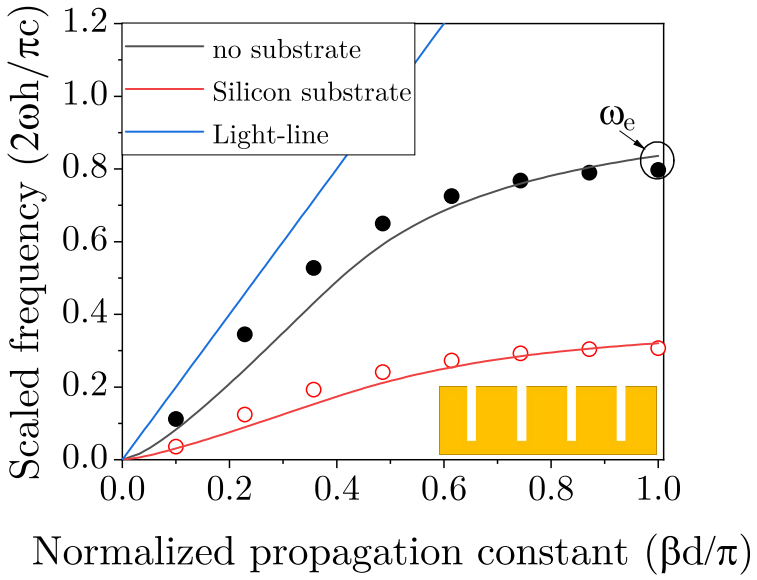

(b)

Figure 2.4: (a)Comparison between dispersion diagram of three different SSPP structure: 3D SSPP (with large thickness), planar 2D SSPP with finite thickness ($t = 2a$), and thin film SSPP (with $t \to 0$). The other geometric parameters are: $h = d \approx 10a$. (b)Comparison between dispersion diagram of thin film SSPP structure ($t \to 0$) for two different case: waveguide placed in air, and placed on a silicon substrate. The other geometric parameters are : $h = d \approx 10a$. The solid lines are from the developed theoretical model in this paper, while the discrete dots (•) and (○) are obtained by FDTD numerical simulation in COMSOL Multiphysics, Version 5.2; Comsol, Inc.

effective propagation constant for an SSPP medium with finite thickness as follows:

$$\begin{aligned} Q^2 &= (\frac{\omega}{c}n_g)^2 - P^2 \\ &= (\frac{\omega}{c}n_g)^2 + (\frac{\omega}{c})^2\frac{1+n_s^2}{2}\frac{a}{d}\,\mathrm{sinc}^2(a\beta/2)\frac{1}{\beta t} = (\frac{\omega}{c}n_{g,eff})^2 \end{aligned} \tag{2.14a}$$

Thus we can state that, the impact of reducing the thickness of SSPP structure from an infinite value to some finite one is equivalent to filling up the interior of the groove of the SSPP waveguide (with infinite thickness) with some material of refractive index $n_{g,eff}$.

$$n_{g,eff}^2 = n_g^2 + \frac{1+n_s^2}{2}\frac{a}{d}\,\mathrm{sinc}^2(a\beta/2)\frac{1}{\beta t} \tag{2.14b}$$

The above analysis implies that the refractive index of the material lying outside of a planar SSPP on its lateral side can redefine the spoof plasma frequency of the medium. Consequently, the lateral surface of a planar SSPP structure is the most sensitive interface among all. This knowledge will help us to design efficient SSPP signal modulation scheme by placing an electro-optic material on the lateral SSPP interface. This will obviate the need to perform uniform deposition of material into the walls of narrow grooves of SSPP waveguides.

2.6 Thin film of SSPP

2.6.1 The concept of effective thickness

The single mode approximation method, while providing a simple way to analyze the behavior of sub-wavelength mode in periodic SSPP structure, has one drawback. As we exclude the higher order modes in our calculation ignoring the field fringing effect at the edges, the extrapolation from the analysis begins to depart from the exact results as the thickness of the metallic structure becomes comparable to the

dimension of the surface emanating the fringe field.

In this work, we propose a different strategy of finding analytical solution for SSPP mode in an ultra-thin waveguide. We introduce a simple yet powerful concept of effective thickness of SSPP groove in order to incorporate the effect of field fringing. Fig. 2.1c gives visualization of the idea of effective thickness and corresponding simulation. The idea of defining an effective thickness of SSPP is owing to the observation that the grooves of SSPP structures essentially behave as capacitors. The capacitance per unit length can be estimated as the following,

$$C_g = \frac{Q_{g,s}}{V_g} = \epsilon_0 \frac{2tE_{g,x}}{aE_{g,x}} = \epsilon_0 \frac{2t}{a}$$

where the surface charge per unit length $Q_{g,s}$ is estimated from the boundary condition $\epsilon_0 E_g.\hat{x} = \rho_s = \frac{Q_{g,s}}{2t}$.

As we know, electric field can be expressed as a contribution from both a scalar potential and a magnetic vector potential, i.e.,$E_{g,x} = -\nabla_x \phi - i\omega A_x = -\frac{\partial \phi}{\partial x} - i\omega A_x$. In our case, $\nabla_x \phi$ is on the order of $\frac{1}{a}$, while the normalized frequency $Q \sim \omega/c$ that we are interested in is much less than π/a. This is why $|\frac{\omega A_x}{\nabla_x \phi}| << 1$, and we can approximate the state inside the groove as a quasi-static field, where $E_{g,x} \approx -\nabla_x \phi$.

A slightly better formula for parallel plate capacitance incorporating field fringing effect up to the limit of $t > a$, provided by Parker (*Parker* (1991, 2002)) enables us to define an effective thickness of SSPP groove as

$$t_{eff}|_{t \geq a} = t\Big[1 + \frac{a}{2\pi t}\Big(1 + ln(\frac{4\pi t}{a})\Big)\Big]$$

We capitalize the very idea of finding the static capacitance between the edges of neighboring metal strips forming grooves of SSPP waveguide (see Appendix **??** for details), which yields an effective thickness for SSPP waveguide with vanishing thick-

ness (i.e., $t \to 0$), as

$$t_{eff}|_{t\to 0} = t_{TF} = \frac{a\pi}{4} \frac{1}{\ln\left(\frac{w + a + \sqrt{a^2 + 2wa}}{w}\right)} \tag{2.15}$$

Here $w = (d - a)/2$, and d is the periodicity of the structure.

2.6.2 Effect of a substrate on thin SSPP

In case of SSPP of nominal thickness on a substrate, we will first find the gross refractive index that an infinitely long and thin conducting strip will experience close to the interface of substrate by applying image theory for dielectric (**?***Lindell et al.* (1997)) as $n_{strip} = \frac{\sqrt{n_s^2 + 1}}{\sqrt{2}}$. The newly defined renormalized refractive index for the hypothetical uniform space around a thin conductor strip n_{strip} basically takes the effect of substrate into account. In contrast, the effective refractive index $n_{g,eff}$ of SSPP structure takes care of phase variation inside patterned metal, described by Eq. 2.14b. In particular, we see a stronger impact of the environment on thin film SSPP reflected through its effective index $n_{g,TF_{eff}}$.

$$n^2_{g,TF_{eff}} = \frac{n_s^2 + 1}{2}\left(1 + \frac{a}{d}\,\mathrm{sinc}^2(a\beta/2)\frac{1}{t_{TF}}\frac{1}{\beta}\right) \tag{2.16}$$

A visual comparison of the band-edge frequencies $\omega_e = \omega|_{\beta=\pi/d}$ (marked with a circle in Fig. 2.4a and 2.4b) normalized with respect to the quarter wavelength frequency (corresponding to $\frac{\pi}{4}$ phase change along the groove length) for SSPP waveguides of different thicknesses is given in Fig. 2.4a. It shows that, for an SSPP waveguide with geometric parameters taken as $h = d \approx 10a$, the modification of the band due to the change of waveguide thickness is nominal, the maximum detuning of ω_e for thin film SSPP waveguide being not more than 20% (i.e. $\frac{\frac{\pi}{2} - \frac{\omega_e h}{c}}{\frac{\pi}{2}} \approx 0.2$). On the other hand, as depicted in Fig. 2.4b, the impact of the substrate on detuning of the band-

edge frequency of a thin film SSPP waveguide from quarter wavelength frequency is remarkable, reaching as much as 70% for silicon substrate, whose refractive index is ≈ 3.5 at 1 THz. This spectacular change in the operating frequency of planar SSPP structure owes to the fact of modified plasma frequency $\omega_p = \dfrac{\pi}{2n_{g,eff}h}$, where $n_{g,eff}$ is described by Eq. 2.14b for SSPP with thickness $t > t_{TF}$ and by Eq. 2.16 for $t \leq t_{TF}$. Figure 2.5b shows the simulation result by COMSOL Multiphysics of the profile of electric field component (E_x) taken along a line passing through an 8μm thick SSPP unit cell. While evanescent field profile exterior to the groove appears as expected, we emphasize on the nature of field interior the groove in particular, as it shows a peculiar profile of hyperbolic spatial distribution with its center at the middle of the groove. This profile justifies our description of the interior E_x field by the function $\cos(i\delta_P t)$, δ_P being a small positive number with unit of wave-vector.

2.7 Properties of confined modes

2.7.1 Degree of confinement

While the dispersion relation of spoof plasmon remains approximately same in both thin and wide structures (up to the small frequency shift), the field confinement along two different directions on the plane transverse to the direction of propagation is subject to different degrees of localization at a given frequency. Figure 2.5a gives a visual illustration of the profile of confined E_x field in an unit cell of SSPP waveguide along two different transverse directions, namely lateral, and vertical. In order to quantify the degree of localization in these two directions, let us attribute the following condition on the transverse wave-vector κ of evanescent mode exterior to the groove for distinguishing the spectrum of modal confinement: $\kappa \geq \dfrac{s\omega}{c}$, where $s > 0$ is a dimensionless parameter specifying the threshold degree of modal confinement in the system of interest. Then using the relation between β and ω, and leveraging the fact

that $\beta \approx \kappa$ on the lateral side of a planar SSPP structure, we arrive at the following inequality condition for the spectra of modal confinement along lateral direction.

$$s^2 \leq 1 + (\frac{a}{d})^2 \tan^2(\frac{\omega}{h}c) \tag{2.17}$$

As the RHS of the inequality 2.17 is always greater than 1, the inequality for modal confinement is always satisfied for all frequencies, as long as $s < 1$ suffices for the system, and we will have modal confinement for all possible frequencies up to the spoof plasma resonance, i.e., the entire band. For arbitrary positive value of s, the fraction of band over which we will achieve threshold confinement along lateral direction can be shown to be

$$\Delta_{c,lat} = \frac{\omega_p - \frac{\omega_{min}h}{c}}{\omega_p} = 1 - \frac{2}{\pi}\tan^{-1}(\frac{d}{a}\sqrt{(s^2-1)u_{s-1}}) \tag{2.18}$$

where u_{s-1} is a unit step function of s with value equal to 1 for $s > 1$, ω_p is the normalized spoof plasma frequency of the meta-structure, and ω_{min} is the frequency corresponding to threshold degree of confinement.

On the contrary, for vertical confinement along Z direction, the bandwidth over which the confinement can exceed threshold value can be shown to be

$$\Delta_{c,vert} = 1 - \frac{2}{\pi}\tan^{-1}(\frac{d}{a}s) \tag{2.19}$$

Comparing Eqs. 2.18 and 2.19, by taking, for instance, $s \to 1$, we can see that, the fraction of the band of modal confinement $\Delta_{c,vert}$ along vertical (Z) direction is much smaller than unity for SSPP structures with narrow grooves. Whereas, for the same value of s, $\Delta_{c,lat}$ approaches unity, which means the degree of confinement along lateral (Y) direction can exceed threshold limit almost over the entire band of thin SSPP waveguide, irrespective of the value of a/d. For $s >> 1$, i.e., for stringent

requirement of deep subwavelength confinement, the two equation becomes similar, as expected.

2.7.2 Bandwidth modulation of confined mode

In order to find the band-width (BW_{sp}) of SSPP waveguide of the fundamental band, it suffices to know the spectral position of the band-edge frequency $\omega(\beta_{max}) = \omega_e$, as $BW_{sp} = \dfrac{1}{2\pi}\omega_e$. Band-edge frequency also indicates the frequency region where the sub-diffraction characteristics of SSPP mode are strongest. For 3D SSPP structure, with groove length of h, refractive index of n_g and a dielectric half-space of index n_d residing on top of it, we can estimate the difference between the plasma frequency (asymptotic frequency) and the band-edge frequency. Let δ_ω be the deviation of the band-edge frequency from normalized plasma frequency $\tilde{\omega}_p = \dfrac{\omega_p}{c} n_g h = \dfrac{\pi}{2}$. We shall let $\tilde{\omega}_e = \dfrac{\omega_e}{c} h = (\dfrac{\pi}{2} - \delta_\omega)\dfrac{1}{n_g}$ to be the normalized band-edge frequency for SSPP mode.

The sensitivity of the band-edge frequency on dielectric half-space can be found as follows,

$$\left.\frac{\partial \tilde{\omega}_e}{\partial n_d}\right|_{3D-SSPP} = -\frac{n_d}{8n_g^2}\frac{a}{h}\Big(\frac{d}{h}\Big)^2 \operatorname{sinc}^2(\frac{\pi a}{2d}) \tag{2.20}$$

The approximation is valid for SSPP structure with groove length $h >> d/2$.

On the other hand, for SSPP mode in planar structure, the sensitivity of $\tilde{\omega}_e$ on the refractive index of the substrate can be shown to be

$$\left.\frac{\partial \tilde{\omega}_e}{\partial n_s}\right|_{2D-SSPP} = -\frac{\pi}{2n_{g,eff}^2}\frac{\partial n_{g,eff}}{\partial n_s} \tag{2.21a}$$

where

$$\frac{\partial n_{g,eff}}{\partial n_s} = n_s \frac{a}{d}\operatorname{sinc}^2(a\beta/2)\frac{1}{\beta t}\frac{1}{2n_{g,eff}} \tag{2.21b}$$

For thin-film SSPP structure, the sensitivity of band-edge frequency on substrate

index is even more pronounced due to the following term

$$\frac{\partial n_{g,TF_{eff}}}{\partial n_s} = n_s\Big(1 + \frac{a}{d}\,\mathrm{sinc}^2(a\beta/2)\frac{1}{\beta t_{TF}}\Big)\frac{1}{2n_{g,TF_{eff}}} \tag{2.22}$$

It is easy to see from Eq. 2.20 that, while in the limit of $\frac{a}{h} \to 0$ for a given groove width a, the dependence of band-edge frequency of a 3D SSPP structure over the dielectric half-space simply vanishes. The dependency of band-edge frequency of a planar SSPP structure (i.e., structure with small thickness) over substrate index is given by Eq. 2.21a.

$$\left|\frac{\partial\tilde{\omega}_e}{\partial n_s}\right|_{2D-SSPP,a/h\to 0} \approx n_s\frac{1}{n_{g,eff}^3}\frac{a}{4t}\,\mathrm{sinc}^2(\frac{\pi a}{2d})$$

where $n_{g,eff}$ is always greater than n_g. We see that, as $t \to \infty$, the band-edge frequency ceases to vary with the refractive index of substrate.

The sensitivity of the band-edge frequency on the optical property of environment can be significant for planar SSPP structure than for its $3D$ counterpart. In the case of strongly confined SSPP mode, which requires $d << h$, the band-edge of the $3D$ SSPP structure will have a scant regard to its environment, while in planar structure the sensitivity of band-edge can remain significant, independent of the ratio of d/h.

For thin film SSPP, the dependency of band-edge frequency over substrate index is the strongest of all, since the groove mode expands into the substrate itself. Our analysis suggests the sensitivity of band-edge frequency of thin film SSPP to be, for $n_s >> 1$

$$\left|\frac{\partial\tilde{\omega}_e}{\partial n_s}\right|_{TF,a/h\to 0} \approx n_s\frac{\pi}{4}\frac{1}{n_{g,TF_{eff}}^3}$$

Figure 2.5c illustrates a comparative view of the change of SSPP bandwidth with the change of the refractive index of external environment, for a $2D$ and $3D$ SSPP structure. The groove length h is taken 5 times the periodicity d, so as to single

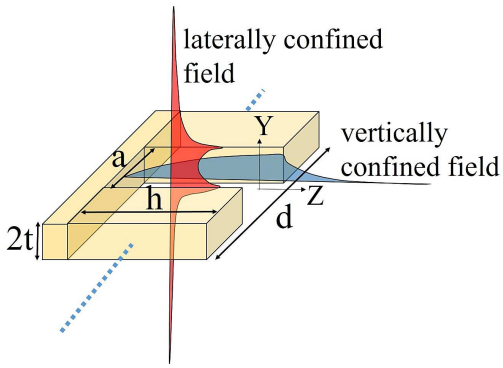

(a)

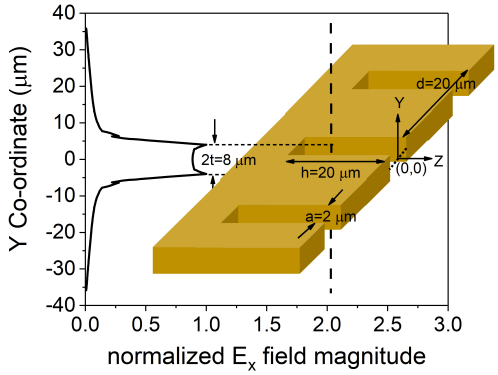

(b)

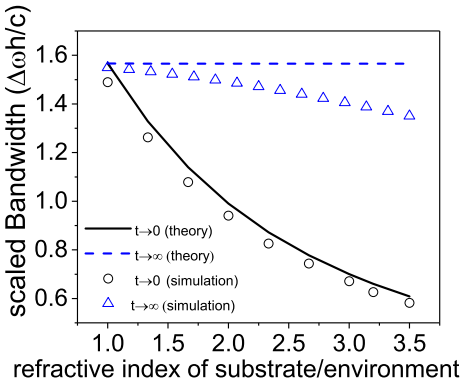

(c)

Figure 2.5: (a)Illustration of confined E_x field profile in 2D transverse YZ plane for a unit cell of SSPP waveguide, while the mode propagates along X direction. Field profile along Y axis is labeled as laterally confined field (red in color), and that along Z direction as vertically confined field (blue in color). (b) Simulation result of the profile of electric field component (E_x) taken along a line crossing through an SSPP unit cell of 8 μm thickness at a frequency $\omega_p/2$, where $\omega_p = \frac{\pi c}{2h}$. (c) Change of bandwidth of a thin film SSPP structure and an infinitely thick SSPP structure with the change of the refractive index of the substrate/external environment. Groove length $h = 10d$,and groove width $a = \frac{d}{10}$. Solid lines are obtained by our developed theory, while the discrete circles (o) and triangles (Δ) are obtained via numerical simulation in COMSOL Multiphysics *Multiphysics*

out the sole contribution of the change of plasma frequency ω_p in governing the change of bandwidth. For $3D$ structure, the change of bandwidth is nominal, as its plasma frequency is independent of the condition of environment. However, for planar thin film SSPP structure, the change of bandwidth is tremendous, since the plasma frequency in this case is indirectly dictated by the environment.

2.8 Summary of the chapter

The current chapter discloses a comprehensive theory that provides the explanation of the properties of spoof surface plasmon mode of electromagnetic wave propagation in a corrugated conductor with tunable geometric parameters such as groove length, width, thickness and periodicity, as well as the coupling of SSPP structure with the external environment, namely,the substrate. The theory specifically introduces new parameters such as effective refractive index and effective thickness of SSPP waveguide, which help reduce the complexity of analysis of spoof plasmon mode in SSPP structures of advanced and large network. An anomalous frequency shift with SSPP thickness reduction is also explicated by deriving the irregular field profile quantitatively and then validating the theoretical models through simulation. Lastly, I discussed how to leverage the lateral surface of SSPP waveguide for broadband modal confinement and high-sensitivity to its surroundings. Therefore, this work will help lay the foundation for the spoof plasmon based novel subwavelength techniques and applications.

CHAPTER III

Performance Analysis of Spoof Plasmon Interconnects

3.1 Introduction

The world is being driven by an ever increasing demand for the distribution of data-intensive content at an enormous speed of information transfer. Large data-centers and high-speed broadband network came into being in order to cope with this vive of information explosion. For example, the bandwidth of chip-to-chip interconnects between LSIs (large-scale integrated circuits) will double every two years and is expected to reach 10 Tbit/s by 2020 (*Brey* (2008)). It is also surmised that by the late 2020s, conventional electrical wiring will not be able to provide any practical solutions (*Urino et al.* (2011)). As explicated by Meindl, the aggressive scaling of devices leads to a Beyond Moore's Law era, marked by 'tyranny of interconnects' (*Meindl* (2003)), where interconnects supplant logic devices in the role of the main factor determining circuit performance. It is predicted that the decisive role of interconnects in circuit characteristics would only strengthen with every future technology node. Therefore, it is imperative for us to investigate new kind of interconnect technology that can overcome the limitation of the current ones. In this chapter, I take a special attention to evaluate the figure-of-merits of a new class of interconnect that carry

data in the form of spoof plasmon mode

3.2 Background studies on interconnect

The trouble of conventional electrical data-bus is that their bandwidth, even with the assumption of the lossless conductor, is limited by the cross-talk among the adjacent wires. Higher frequencies are more susceptible to cross-talk and therefore compromises signal integrity.

There also exists an alternative interconnect implementation based on optical communication link (*Haurylau et al.* (2006)), renowned for its gigantic bandwidth of tens of Tbps (*Keiser* (2003); *Essiambre et al.* (2010)). However, optical interconnects comes with a price. Conventional photonic technologies are quite different from those of electronics in terms of materials, device sizes, and fabrication processes and thus lacks high density photonic device integration (*Lim et al.* (2014); *Michel and Kimerling* (2007); *Shin et al.* (2013); *Roelkens et al.* (2014)). Because of the large thermo-optic effect in silicon compared to the electro-optic effect, the projected advantage of power economization in chip-level optical interconnect almost nullifies once we account for the power consumed by the thermal stabilization circuit (*Dokania and Apsel* (2009)). In addition, the high overhead energy cost associated with electro-optic signal conversion, and large (hundreds of wavelength) foot-print of optical modulato (*Urino et al.* (2013)) render optical interconnect almost prohibitive for data-bus smaller than 10 cm length (*Markov et al.* (2012); *Roelkens et al.* (2005)). According to Cho and coworkers (*Cho et al.* (2004)), the critical length below which optical interconnect is energetically less-favorable for data transfer than its electrical counterpart is 15 cm for a typical coupling loss of 3 dB at 6 Gbps data rate even with the assumption of an ideal modulator. Thus, we are left with a range of distance of $0.1 - 10$cm, dubbed as the 'last centimeter barrier', which falls into the category of inter-chip distance and looms insurmountable with any available cost-

effective means (*Gu* (2015)).

3.3 Author's contribution to the field of interconnect design

In chapter 1, I discussed in detail about the complexity of choosing between electrical and optical interconnects for short distance communication, given that the rate of data traffic varies widely over time. I argued that the dilemma of favoring one interconnect technology over the other under the above circumstances can be circumvented by designing a reconfigurable interconnect technology: where the physical interconnect can alter its mechanism of guiding wave to minimize energy consumption per bit of transferred data at all possible traffic rate. With this quest in mind, I investigate the potential of spoof surface plasmon polariton (SSPP) interconnects. With feature sizes of few tens of microns, which coincide with the dimensions of the wire pitches on electrical backplane limited by the geometric size of the chip pins and pads, this alternative technology may become a new paradigm in inter-chip communications. Since the analysis of electrical means of information transfer via conductive SSPP interconnects associated with a metallic ground are well-understood, I rather aim to discuss how to harness the potential of strong field confinement in the SSPP channel, unaided by any ground wires. Coined by the seminal work of Pendry and co-workers (*Pendry et al.* (2004b); *Garcia-Vidal et al.* (2005b)), spoof surface plasmon polariton (SSPP) is a special electromagnetic mode where the artificial plasma frequency are design specific rather than material specific. In addition, the modal volume of SSPP can be squeezed far below the Abbe diffraction limit without requiring the electromagnetic field penetrate into the metal. Thus we can, via SSPP, guide a signal through a sub-diffraction space.

The demonstration of the existence of SSPP mode in ultrathin structure by Shen et al. (*Shen et al.* (2013b); *Shen and Jun Cui* (2013)) broadened the scope of the application of spoof plasmon waveguide (*Ma et al.* (2014)). In 2016, Hao Yu and his

group demonstrated sub-wavelength size standalone interconnect operating at THz range implemented in thin, planar CMOS compatible SSPP metamaterial (*Liang et al.* (2015b,a, 2016)). This revealed the potential of SSPP interconnect to become a novel way of data transfer media between chips at THz speed and beyond.

Because of the nature of field confinement around an SSPP channel, the channels in a network can be designed to remain essentially isolated from each other in a compact design scheme. The bandwidth limitation on SSPP channel derives from a quite different physics: it is the resonant frequency of the unit cell (which in turn depends on the geometry of the cell) of the metamaterial that defines the bandwidth. Spoof plasmonics can be a very rich fields to explore for the future tera-scale data transfer between chips, as the spoof plasmon interconnect may amass the good sides of both electrical and optical interconnects. On the one hand, the SSPP interconnect possesses the great advantage of CMOS compatibility and its quasi-electrical mode can transfer data without a modulation scheme and thus liberate from overhead energy cost of source driver, modulators' and detectors' power. On the other hand, like optical ones, it can suppress cross-talk at high frequencies where bandwidth per channel can be few hundreds of Gbps for few tens of mm information propagation length, in addition to the possibility of ultra-low energy (subfemtojoule) (*Miller* (2017)) signal detection through facilitating 'quantum impedance conversion' (*Miller* (2010)) of photon. We may switch between these two different types of information transfer mode in SSPP interconnect, namely electro-SSPP and opto-SSPP mode, which may offer an energy-economic data transfer solution between chips where the data traffic volume may vary by orders of magnitude over the course of time. In this chapter, I will show that, with my prescribed geometry, an SSPP based data-bus can provide ~ 1 Gbps/μm bandwidth density while the signal can propagate upto state-of-the-art chip edge length ~ 10 mm, where each channel would carry information at approximately 300 Gbps rate without invoking significant cross-talk.

The current chapter demonstrates the fundamental interplay between various figure-of-merits of information capacity of an inter-chip communication network comprising SSPP channels. In section 3.4, I discuss the bandwidth density maximization strategy in an SSPP network. In section 3.5, I define the characteristic length of information propagation pertaining to SSPP channel and its relation to the geometry of the channel. Section 3.6 shows the relation between finite information propagation length and the resistivity of SSPP channel, which eventually led to the estimation of noise property and Shannon information capacity in the limit of thermal noise contributed by the SSPP channels. Section **??** discusses the quantitative comparison between various alternatives of chip-to-chip interconnects in terms of cross-talk in the system.

3.4 Bandwidth in Cross-talk mediated SSPP channels

Figure 3.1a is a schematic of the data transfer system that we propose for inter-chip communication where the data-bus consists of SSPP channels running in parallel. A pair of channels are formed by placing two SSPP waveguides back to back. Each of such channel-pair maintains a guard space between the nearest face-to-face SSPP waveguides to avoid cross-talk. An SSPP mode possesses a continuous band, starting from zero frequency- where there is no field confinement and hence the channel is subjected to significant cross-talk with the neighboring channels; upto the spoof plasma frequency- where the degree of field confinement is maximum and the channels can be decoupled from each other (Fig. 3.1b). Between these two extremities, the field localization property undergoes gradual changes. Figure 2.4b shows the dispersion diagram of an isolated SSPP channel. In order to generate a dispersion diagram independent of geometric dimensions of interconnects, we, in Fig. 2.4b, instead of plotting the absolute value of frequency ω and propagation constant β, choose to plot a unit-less frequency parameter $\hat{\omega} = 2\omega h/\pi c$ against another unit-less propagation

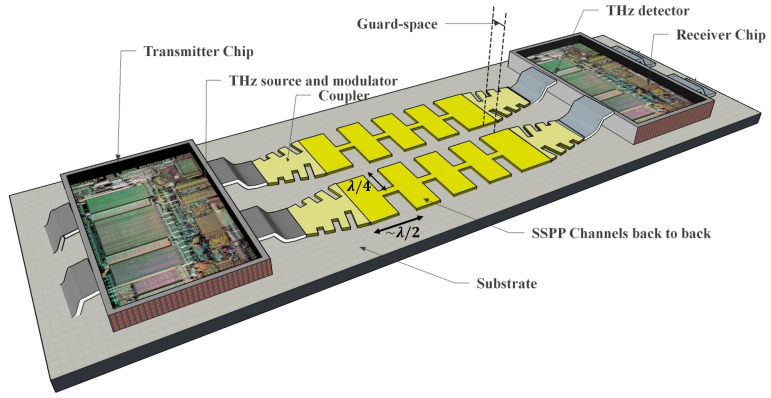

(a)

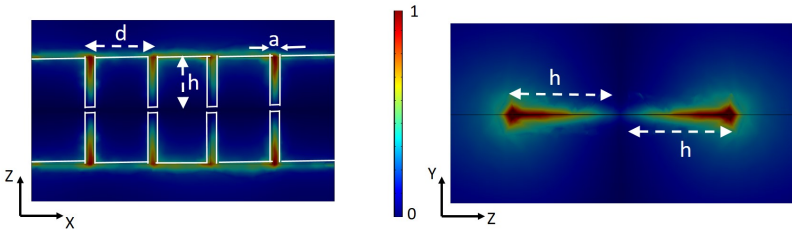

(b)

Figure 3.1: (a) An inter-chip communication network employing SSPP channels. Scales of interconnects are shown in terms of free-space wavelength (λ) corresponding to spoof plasmon resonance, a typical wavelength being 300 μm. (b) The left figure is the top-view of electric field distribution in SSPP channels, while the right figure is a cross-section view of the field, showing modal confinement. The simulation frequency is $\sim$ 1 THz, roughly the spoof plasmon resonance frequency of an SSPP interconnect with groove length 80 μm.

parameter $\hat{\beta} = \beta d/\pi$. At a given frequency ω, any change in the geometric dimension of SSPP interconnect would cause a corresponding change in the absolute value of β in such a way that the relation between the normalized parameter $\hat{\omega}$ and $\hat{\beta}$ will remain unaltered, as they absorb the effect of geometric change into themselves. We may distinguish two different regions in the dispersion curve of SSPP channels. One of them is the strong SSPP regime, where the dispersion curve becomes almost flat and provides deep sub-wavelength field confinement, which can be leveraged for high resolution imaging. The other region is the soft SSPP regime, where the field localization is moderate, however the bandwidth of this region is appreciably large. As soft SSPP regime can offer both large bandwidth and field confinement together, this can be leveraged towards making interconnect channel with high information capacity which may defy RC limited bandwidth.

Let us begin our analysis of an SSPP interconnect system by designating the groove length, width, period, thickness and channel separation as h, a, d, $2b$ and $2t$, respectively. It is shown in other works that the thickness ($2b$) of SSPP waveguide plays a trivial role in determining dispersion relation. This helps to divide the SSPP system in two independent 2D sub-systems for the sake of simpler analysis. The first subsystem comprises of a periodic groove of length h and period d on zx-plane where the subsystem is infinitely extended along y-direction. The second subsystem consists of a periodic array of metal slabs of small thickness $2b$, separation a, and period d on xy-plane where the subsystem is considered infinite along z-direction. Taking the midpoint of the groove as the origin of co-ordinates, the field distribution on the surface of the first sub-system can be written as follows.

$$
\begin{aligned}
E_{ax}^{(d)}(z) &= \sum_n A_{an} e^{-\kappa_{c,an}(z+t)} \\
E_{bx}^{(d)}(z) &= \sum_n A_{bn} e^{\kappa_{c,bn}(z-t)} \\
E_{az}^{(d)}(z) &= -\sum_n \frac{i\beta_{an}\kappa_{an}}{k^2-\beta_{an}^2} A_{an} e^{-\kappa_{c,an}(z+t)} \\
E_{bz}^{(d)}(y) &= \sum_n \frac{i\beta_{bn}\kappa_{bn}}{k^2-\beta_{bn}^2} A_{bn} e^{\kappa_{c,bn}(z-t)}
\end{aligned}
\tag{3.1}
$$

where A_{an} and A_{bn} are the complex amplitude of n-th mode of face-to-face posing SSPP waveguides 'a' and 'b', respectively, β is the propagation constant, and κ_c is the attenuation constant of evanescent field along z direction. κ_c can provide a measure of modal confinement that we shall capitalize to suppress cross-talk, and we shall be discussing about it in detail shortly. The magnetic field components outside the groove can be expressed as

$$
\begin{aligned}
H_{ay}^{(d)}(z) &= -\sum_n \frac{i\omega\epsilon_0\kappa_{an}}{k^2-\beta_{an}^2} A_{an} e^{-\kappa_{c,an}(z+t)} \\
H_{by}^{(d)}(z) &= -\sum_n \frac{i\omega\epsilon_0\kappa_{bn}}{k^2-\beta_{bn}^2} A_{bn} e^{\kappa_{c,bn}(z-t)}
\end{aligned}
\tag{3.2}
$$

Each of the above components has $e^{i\beta x}$ dependence along the propagation direction x. The dispersion relation of the sub-system is *Erementchouk et al.* (2016b),

$$
\sqrt{\beta^2 - Q^2} = Q\frac{a}{d}\,\mathrm{sinc}^2(\frac{a\beta_0}{2})\tan(Qh) \tag{3.3}
$$

where Q is the wave-vector inside the grooves along their length, and for infinitely extended subsystem ($2b \to \infty$) along y direction, $Q = k_0 = \frac{\omega}{c}$. The relation of $Q \approx k_0$ holds even at the limit of vanishing thickness b of SSPP interconnects. Therefore, analysis of surface mode for the second subsystem with finite thickness can be postponed until we begin section 3.6 that discusses thermal noise in SSPP interconnects. The length of modal confinement (t_c) of SSPP modes can be esti-

mated as $t_c = \dfrac{1}{2\kappa_c} = \dfrac{1}{2\sqrt{\beta^2 - (\frac{\omega}{c})^2}}$, where ω is angular frequency, and c is the speed of light. In order to transfer data with suppressed inter-channel coupling (less than $-3\ dB$), we may choose to utilize the upper f_c fraction of the bandwidth (BW_{sp}) of an SSPP channel where modal confinement is stronger. Then $\kappa_{c,min} \approx \dfrac{a}{d}\dfrac{\omega_{min}}{c} n_{g,eff} \tan(\dfrac{\omega_{min}}{c} n_{g,eff} h)$, where $\omega_{min} = 2\pi(1 - f_c)BW_{sp}$, and $n_{g,eff}$ is the effective refractive index of the medium adjacent to the channel. Hence the minimum amount of space required to interleave between a pair of neighboring SSPP channel is

$$t_{c,max}/h = \frac{d}{2a}\Big(\frac{1}{1 - f_c}\Big)^2 \Big(\frac{c}{2\pi n_{g,eff} h.BW_{sp}}\Big)^2. \tag{3.4}$$

The bandwidth BW_{sp} is itself a function of the groove geometry, particularly governed by groove length, as (*Erementchouk et al.* (2016b)):

$$\begin{aligned} BW_{sp} &= (\frac{\pi}{2} - \delta_w)\frac{c}{2\pi n_{g,eff} h} \\ &= \frac{c}{2\pi n_{g,eff} h}\Big[\frac{\pi}{2} - \frac{a}{d}\frac{d}{\sqrt{4h^2 - d^2}}\Big], \end{aligned} \tag{3.5}$$

An important figure of merit for an interconnect network is the bandwidth density (ρ_{BW}), defined as the amount of bandwidth available for data transfer per unit cross-sectional length of the data-bus at reduced cross-channel coupling. It has been experimentally demonstrated that, by placing two SSPP waveguide back-to-back with nominal separation, the cross-talk between them can be kept below -20 dB (**?**). So, the critical separation which would determine the channel packing density is the separation between two SSPP waveguide placed face-to-face. Bandwidth density of SSPP data bus of a design shown in Fig. 3.1a can be expressed as

$$\begin{aligned} \rho_{BW} &= \frac{2f_c.BW_{sp}}{t_{c,max} + 2h} \approx \frac{cf_c}{2n_{g,eff} h(t_{c,max} + 2h)} \\ &= \frac{c}{4n_{g,eff} h^2}\frac{f_c(1 - f_c)^2}{(1 - f_c)^2 + D}, \end{aligned} \tag{3.6}$$

where $D = \dfrac{d}{\pi^2 a}$. As evident from Eq. 3.6, choosing a substrate with low refractive index ($n_{g,eff}$ lower) is beneficial for the design of a closely packed SSPP network for a given bandwidth of data transfer. In addition, it shows that reducing groove length h leads to a greater bandwidth density. The lowest limit on h is dictated by the condition on the ratio of geometric length of the structure to support spoof plasmon mode, which is $2h > d$ (*Erementchouk et al.* (2016b)). The dependence of ρ_{BW} over f_c (i.e., fraction of total SSPP bandwidth BW_{sp} which is cross-talk suppressive) is also worth looking at. For small f_c, cross-talk limited bandwidth linearly increases with f_c, however, ρ_{BW} quadratically decreases as f_c approaches its maximum value of 1. Its optimum value $f_{c,opt}$ can be determined by considering $\dfrac{\partial \rho_{BW}}{\partial f_c} = 0$ that yields:

$$
\begin{aligned}
f_{c,opt} &= 1 - \frac{(D + \sqrt{D^2 + D^3})^{2/3} - D}{(D + \sqrt{D^2 + D^3})^{1/3}} \\
&\approx \begin{cases} \dfrac{2}{5} - \dfrac{3}{50}\delta, \text{ when } D = 1 + \delta \\ \\ \dfrac{1}{3}(1 + \dfrac{2}{3\sqrt{D}}), when \text{ D¿¿1} \end{cases}
\end{aligned}
\tag{3.7}
$$

In this limit of large D, an interesting relation of ($f_c \geq \frac{1}{3}$) emerges, which indicates that we can have at least 33% of the total bandwidth of the SSPP channel available for cross-talk suppressive data transfer. If we plug in the nominal value of $f_c = \frac{1}{3}$ in Eq. 3.6, then the maximum attainable bandwidth density in SSPP network is found to be $\rho_{BW}|_{max} \approx \dfrac{\pi^2 c}{n_{g,eff} h^2} \dfrac{1}{12\pi^2 + 27d/a}$.

Figure 3.2a gives the visual depiction of bandwidth optimization strategy. It shows that, we may utilize the upper 33% of each of the SSPP channel bandwidth to maximize the bandwidth density (ρ_{BW}). As the condition of existence of SSPP warrants $h_{min} = d/2$, we can increase bandwidth density ρ_{BW} further by reducing periodicity d. However, a reduction of d would increase the mode coupling factor

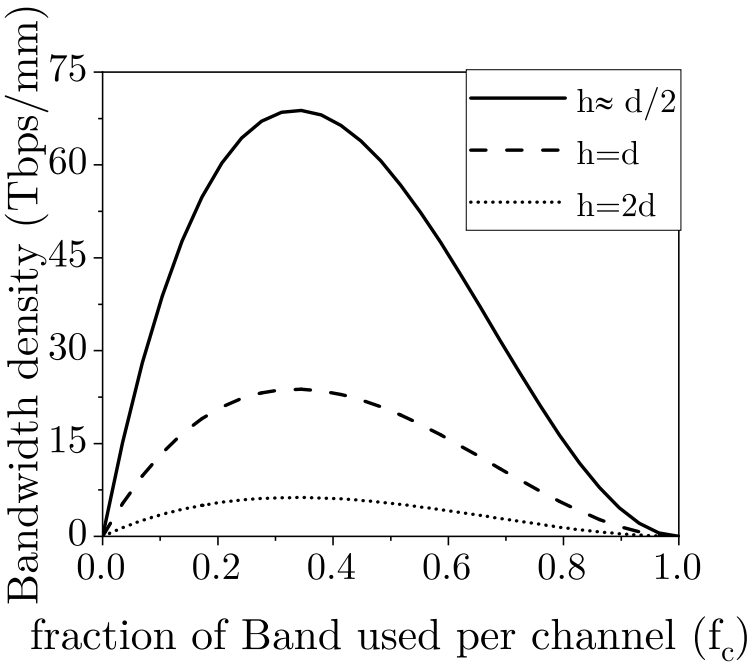

(a)

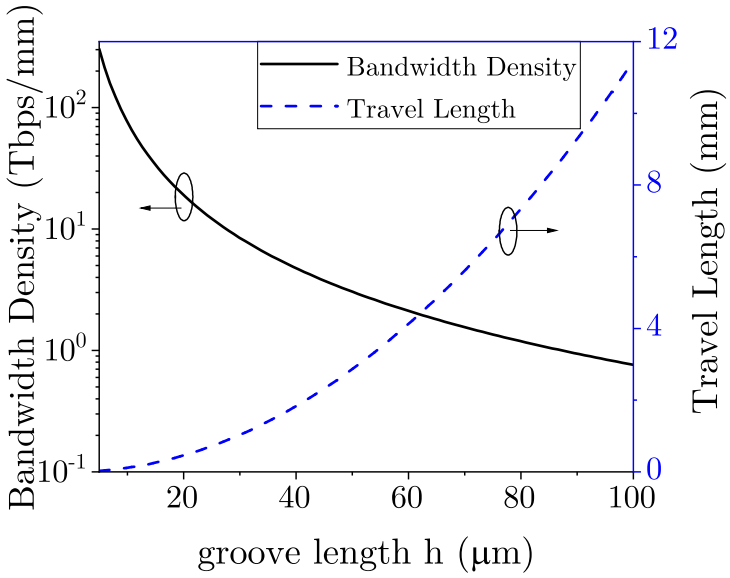

(b)

Figure 3.2: (a)Bandwidth density of SSPP data bus versus the fraction of the bandwidth utilized per SSPP channel. The graph is drawn for data bus consisting of crosstalk suppressive SSPP channels, each having a period, $d = 20\ \mu m$,$a \sim \frac{1}{10}d$. (b)The left vertical axis shows optimum bandwidth density ($f_c = 1/3$) of the SSPP data-bus. The groove length of the waveguide is varied, while the aspect ratios of its geometric parameters are kept fixed at $a/d = 0.1$, $h/d \approx \frac{1}{2}$. The right vertical axis shows the corresponding characteristic length of the SSPP channel made of gold (skin depth of gold at THz is ~ 60 nm) up to which half of the signal power retains.

$\frac{a}{d}$, which would adversely affect the BW_{sp}. In addition, reduction of h would also move the system into higher operating frequency, where the Ohmic loss in conductor through the skin effect would creep in and limit signal propagation length. Section 3 deals with the question of how far the information can travel through a channel consisting of a real metal with finite conductivity.

One other interesting feature of SSPP channel is its nature of confinement along the vertical (y) direction, which is in fact stronger than its lateral confinement and can be shown to be

$$t'^{-1}_{c,max} = 2\kappa'_{c,min} \approx 2\beta_{min} \approx \frac{\pi(1-f_c)}{n_g h} \tag{3.8}$$

where κ'_c is the vertical evanescent wavevector along y direction. If we stack SSPP channels one on top of the other with interleaving space between them equal to the vertical confinement length ($t'_{c,max}$) of the mode, then the bandwidth density ρ'_{BW} of the vertically stacked channels becomes,

$$\rho'_{BW} \approx \frac{\pi c}{4n_g^2 h^2} f_c(1-f_c) \tag{3.9}$$

Comparison of bandwidth density for planar SSPP channel cluster and that for vertical channel cluster written in Eq. 3.6 and 3.9 respectively reveals an interesting fact. Equation 3.9, unlike Eq. 3.6 is free from the term d/a. This adds a relative flexibility in designing the groove width a without affecting the bandwidth density. In addition, Eq. 3.9 shows that the optimal fraction of SSPP bandwidth in cross-talk suppressive regime, in case of vertical channel stacking, can be 50%, significantly higher than that achievable in planar arrangement of channels.

3.5 Traveling length of SSPP mode in lossy metal

Following (*Rusina et al.* (2010b)), we can incorporate metallic loss in our analysis of SSPP channel for metal with finite conductivity. We begin so by modifying the wave-vector Q along the direction(z) of groove length as follows,

$$Q \approx Q_0 n_g \Big(1 + i\frac{l_s}{2a}\Big) \tag{3.10}$$

where $Q_0 = \dfrac{\omega}{c}$, l_s is the skin depth of the metal. Employing the characteristic dispersion relation of SSPP mode (*Erementchouk et al.* (2016b); *Song and Mazumder* (2009)), we determine the finite propagation length of SSPP mode l_p at a given frequency as,

$$\frac{1}{2}l_p^{-1} = Im[\beta] \approx \begin{cases} Q'', for \beta \sim Q_0 n_g \\ \dfrac{\pi}{2}\dfrac{d}{a}Q''\dfrac{4h^2 - d^2}{d^2}, for \beta >> Q_0 n_g \end{cases} \tag{3.11}$$

where $Q'' = Im[Q]$. The regime $\beta >> Q_0 n_g$ can be seen in an SSPP structure with groove length (h) significantly larger than half of the period (d). It should be emphasized that the structures considered in the present work are characterized by $h < d$, and therefore do not operate in the strong decay regime. While a knowledge of l_p at a single carrier frequency ω_c may suffice to estimate the propagation distance of a message signal with bandwidth $\Delta\omega_m$ as long as $\omega_c >> \Delta\omega_m$, it is not quite useful in case of information transfer over SSPP channel network, where the carrier frequency is supposed to be nearly comparable to the signal bandwidth. Under such circumstances, we find it worthwhile to introduce a slightly different characteristic length l_t which is defined as the length that a pulse with rectangular Fourier spectral profile of bandwidth $\Delta\omega_m$ can travel until the power distributed over its bandwidth

reduces by half. This leads to following relation of power loss in metal,

$$P_{loss} = \int_{\omega_{min}}^{\omega_{max}} A^2 e^{-2\beta_I(\omega) l_t} d\omega = \frac{A^2 \Delta\omega_m}{2} \tag{3.12}$$

where $\beta_I = Im[\beta]$. If we operate in the weak SSPP regime for information transfer, it can be seen from Eq. 3.10 and 3.11 that, for $\frac{a}{d} << 1$,

$$\beta_I \approx \frac{\omega}{c} \frac{l_s}{2a} \tag{3.13}$$

Replacing the variable ω with β_I in the equation of P_{loss}, we get

$$l_t = \frac{1}{2} \frac{a}{l_s} \frac{c}{\omega_{mid}} \tag{3.14}$$

where the approximation $e^x \approx 1 + x + \frac{1}{2}x^2$ is applied, and $\omega_{mid} = \frac{\omega_{max}+\omega_{min}}{2}$. In terms of the spoof plasma frequency $\omega_p = \frac{\pi c}{2h}$ of the SSPP channel, we can rewrite the expression for l_t as,

$$l_t = \frac{1}{2} \frac{a}{l_s} \frac{c}{\omega_p(1 - 0.5 f_c)} = \frac{a}{l_s} \frac{h}{\pi(1 - 0.5 f_c)} \tag{3.15}$$

where $\omega_{max} \approx \omega_p$ is assumed, and $\Delta\omega_m = f_c \omega_p$ is substituted. It is obvious from the expression of l_t that, for a given information bandwidth $\Delta\omega_m$, the larger the length of the groove h of SSPP we choose, the further the signal can travel. The expression for bandwidth density and information propagation length reveals a fundamental trade-off about choosing groove length h. While choosing smaller h increases cross-talk limited bandwidth density of SSPP data-bus, it decreases signal traveling length through the channel. Figure 3.2b illustrates this trade-off, drawn for waveguide whose geometry is varied in a way so as to keep all relevant aspect ratios fixed at some optimal value (i.e., $h/d \sim \frac{1}{2}$, $a/d = 0.1$) and the groove length h is varied. The corresponding

maximum bandwidth density of SSPP data-bus and the traveling length of information at that maximum bandwidth density is plotted on the same graph. It can be seen from the diagram that, for interconnect length to be ~ 10 mm, which is roughly the state-of-the-art chip edge length, we can obtain ~ 1 Gbps/μm bandwidth density with an optimal geometry design of SSPP waveguide. Information carried by each channel can be determined as bandwidth density multiplied by an average space occupied by an individual channel including the guard space, which is found to be 300 Gbps. In order to determine the upper bound of signal propagation limit, we choose gold while plotting the numerical value of Fig. 3.2b which has a better conductivity over other commonly used metals. For a different choice of metal with conductivity σ_m, the numerical value of information transfer length can be found by scaling the value determined in Fig 3.2b by a factor of $\sqrt{\frac{\sigma_m}{\sigma_{Au}}}$, since skin depth $l_s \sim \frac{1}{\sqrt{\sigma}}$. If the optimal value of f_c is taken as $\frac{1}{3}$ as discussed previously, the corresponding value of information traveling length will be $l_{t,opt} = \frac{6}{5\pi}\frac{a}{l_s}h$.

3.6 Information capacity in the limit of thermal noise

In the regime of low-cross-talk, the main limitation on the Shannon information capacity of a channel originates from signal to noise ratio (SNR) in the channel. In the present work, we are particularly interested in the thermal noise characteristics of SSPP channels, which is expected to be the most dominant type of noise over others (such as flicker noise and shot noise) at higher operating frequency and low power transmission. If SNR of SSPP channel is limited by thermal noise, we may want to determine the equivalent electrical resistance of SSPP channel in order to estimate thermal noise. To this goal, we calculate the power ($P_{x,tot}$) propagating in the longitudinal (x) direction on a planar SSPP channel on each of its side and equate the fraction of the power lost in joule heating process with I^2R loss. Because of the boundary condition on the plane of SSPP channel made of metal of good

conductivity, it can be argued that the in-plane component E_z is negligible compared to the other component E_y of electric field. Hence power spectral density $P_{x,tot}$ is mainly contributed by E_y and H_z and can be found as follows.

$$\begin{aligned} H_{z,a} &= Ae^{i\beta x}e^{-\kappa(y-b)}e^{iQz} \\ E_{y,a} &= \frac{\beta}{\omega\epsilon}Ae^{i\beta x}e^{-\kappa(y-b)}e^{iQz} \\ P_{x,tot}(\omega) &= \frac{1}{2}\int_{z=0}^{h}\int_{y=b}^{\infty} Re[E_{y,a}H_{z,a}^{*}]dydz = \frac{1}{4}\frac{\beta}{\omega\epsilon\kappa}A^2h \end{aligned} \tag{3.16}$$

The set of relations in Eq 3.16 describes the second subsystem, discussed in section 3.4, comprised of metal slabs of infinite length and $2b$ thickness that accounts for field distribution in the region defined by $y \geq b$. Here A is the amplitude of magnetic field with the SI unit of Amp / meter $/\sqrt{Hz}$, and $\epsilon = n_{g,eff}^2$ is the effective homogeneous permittivity of the medium mediated by SSPP channel. The surface current in the longitudinal direction is

$$I_x(\omega) = \int_0^h J_x dz \approx hH_{z,a}(x)|_{y=b} = Ahe^{i\beta x} \tag{3.17}$$

If a pulse of bandwidth $\Delta\omega_m$ is to be transferred through the SSPP channel, half of the power will be lost after traveling the characteristic length l_{tr}. Thus the resistance (R_{SP}) of SSPP channel per unit length can be found from the following:

$$|I_x|^2 R_{SP} l_t \Delta\omega_m = \frac{1}{2}\int_{\omega_p-\Delta\omega_m}^{\omega_p} P_{x,tot}(\omega)d\omega \tag{3.18}$$

where we used the spoof-plasma frequency ω_p in the limit of integral as an approximation of BW_{sp}. If we denote the wave-vector along the groove length as Q, then using the fact that $Q \approx \omega/c$ in the relation $\beta^2 - \kappa^2 + Q^2 = (\omega/c)^2$ describing the dispersion characteristics of the field over the SSPP surface, we can set $\beta \approx \kappa$. Thus

we obtain,

$$R_{sp} = \frac{1}{8l_t}\frac{1}{\epsilon h \Delta\omega_m}\ln\left(\frac{\omega_p}{\omega_p - \Delta\omega_m}\right) = \frac{1}{8l_t}\frac{1}{\epsilon h \Delta\omega_m}|\ln(1 - f_c)| \tag{3.19}$$

where $\Delta\omega_m = f_c\omega_p$ is used. Then the electronic noise generated by the thermal agitation of electrons on patterned metal of the channel can be modeled as a noiseless resistor in series connection with a noise voltage source $\bar{v}_n$ as follows.

$$\bar{v}_n^2 = 4k_B T R_{sp} l_{ch} \Delta\omega_m / 2\pi \tag{3.20}$$

where $l_{ch} = Nd$ is the channel length, N being the number of unit cell in the SSPP channel with the period d. In addition, k_B is the Boltzmann constant and T is the absolute temperature of the channel. Now if the SSPP mode excites an rms voltage value of V_r at the signal receiving end, the Shannon information capacity (C_{info}) of SSPP channel in the limit of thermal noise can be written as

$$\begin{aligned} C_{info} &= \rho_{BW}\log_2(1 + SNR) \\ &= \rho_{BW}\log_2\left(1 + \frac{2\pi V_r^2(\Delta\omega_m)}{4k_B T R_{sp} l_{ch}\Delta\omega_m}\right) \end{aligned} \tag{3.21}$$

where $SNR = \dfrac{V_r^2}{\bar{v}_n^2}$ is the signal to noise ratio, ρ_{BW} is the SSPP bandwidth density limited by cross-talk among neighboring channels and follows Eq. 3.6. Voltage drop V_r across the receiver resistance R_r is related to the transmitted information bandwidth $\Delta\omega_m$ as follows.

$$V_r^2 = P_r R_r \tag{3.22}$$

$$P_r = \frac{1}{4}\frac{1}{\epsilon}A^2 h\left|\ln(1 - \frac{\Delta\omega_m}{\omega_p})\right|(1 - \frac{1}{2}\frac{l_{ch}}{l_t}) \tag{3.23}$$

where P_r is the power at the receiving end. Characterization of SSPP channel resistance R_{sp} facilitates determining the bit error rate (BER) due to channel induced noise. Out of two types of noise, namely, thermal noise and shot noise, let us assume that thermal noise prevails over shot noise (i.e., thermal noise power is at least twice of shot noise power), and the receiver can be controlled in a way so as not to contribute to the thermal noise. In addition, let us also choose to design receiver input resistance (R_r) to be an order of magnitude larger than the channel resistance ($R_{ch} = R_{sp}Nd = \frac{1}{r}R_r$), so that we may have large voltage drop (V_r) at the receiving end. Shot noise power can be written as $2qI_r\Delta f R_r$, where $I_r = \frac{V_r}{R_r}$. Thermal noise power can be written as $4k_BTR_{ch}\Delta f\frac{1}{R_r}$. Then the above stated condition leaves us with the following inequality condition

$$\frac{4k_BTR_{ch}\Delta f}{R_r} \geq 2 \times 2q\frac{V_r}{R_r}\Delta f R_r \tag{3.24}$$

These conditions set an upper limit for the signal voltage (V_r) at the receiving end as $V_r \leq \frac{k_BT}{rq}$, where r is the ratio of resistance of the receiver to the channel, q is the charge of electron. Since SSPP channel is not suitable to carry DC current, as at $\omega = 0$ there would be no field confinement, we must choose a source encoding scheme that is devoid of any DC offset. Let us choose non-return-to-zero (NRZ) coding for digital signal transmission where bit-0 and bit-1 are represented by negative and positive pulses of equal amplitude. Since we also want to maximize the information capacity by choosing optimal SNR, let us set $\pm V_{r,max} = \pm\frac{k_BT}{rq}$ to denote the mean value for binary bits, and zero as the threshold value. Since NRZ encoding is symmetric for 0 and 1 bit, the probabilistic bit error rate can be calculated as

$$\begin{aligned} BER &= \frac{1}{v_n\sqrt{2\pi}}\int_0^\infty \exp\Big(-\frac{(V+V_r)^2}{2v_n^2}\Big)dV \\ &= \frac{1}{2}\operatorname{erfc}\Big(\frac{V_r}{v_n\sqrt{2}}\Big), \end{aligned} \tag{3.25}$$

where $V_r = V_{r,max}$ is chosen for maximum SNR. Then for the utilization of f_c fraction of SSPP bandwidth for data transmission with suppressed inter-channel coupling, the BER can be related with the geometry of the SSPP waveguide as follows.

$$BER_{sp} = \frac{1}{2}\,\mathrm{erfc}\left(\frac{1}{rq}\sqrt{\frac{\pi\epsilon k_B T}{|\ln(1-f_c)|}\frac{l_t}{l_{ch}}}\sqrt{h}\right) \tag{3.26}$$

If $f_c = \frac{1}{3}$ is chosen for the reason of bandwidth density maximization as described in previous section, and channel length is taken as $l_{ch} = l_t$, and $r = 10$ is considered, then the optimal BER turns out to be $BER_{sp,opt} = \frac{1}{2}\,\mathrm{erfc}\left(\frac{1}{5q}\sqrt{\frac{\pi\epsilon K_B T}{2\ln(3/2)}}\sqrt{h}\right)$. At the same optimal condition for data transfer within thermal noise limit, the optimal Shannon information capacity can be written as

$$\begin{aligned} C_{info,opt} &= \rho_{BW,max}\log_2(1+SNR_{max}) \\ &= \frac{\pi^2 c}{n_{g,eff}h^2}\frac{1}{12\pi^2 + 27\frac{d}{a}} log_2\Big(1+\frac{8\pi\epsilon h K_B T}{25q^2\ln(3/2)}\Big) \end{aligned} \tag{3.27}$$

where SNR_{max} is the maximum SNR possible to obtain at the receiver while still operating in the limit of thermal noise generated by SSPP channel. Figure 3.3 shows how the Shannon information capacity and BER of an SSPP channel at room temperature vary with the groove length while SNR is maximum at the receiving end within the limit of thermal noise generated by SSPP channel.

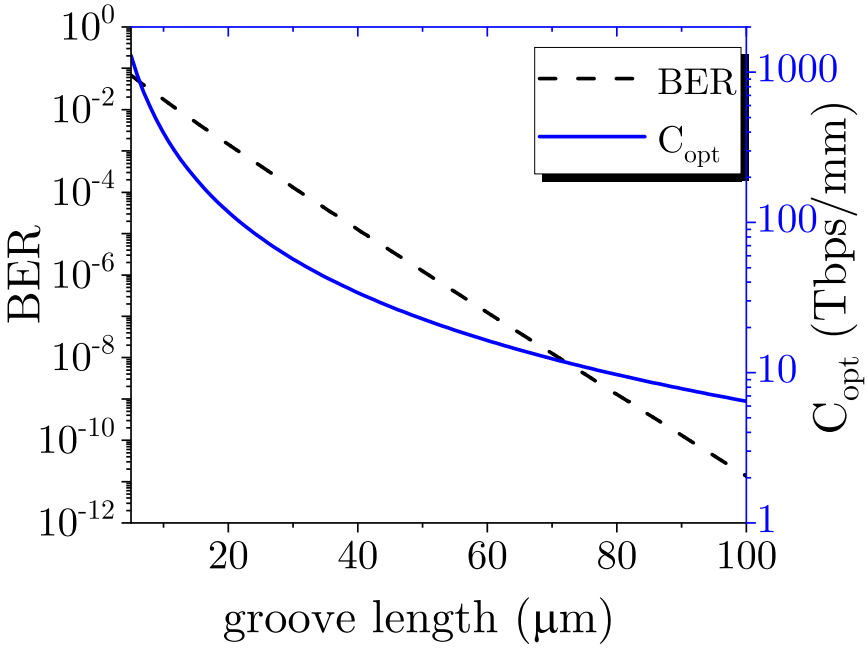

Figure 3.3: Variation of the optimized Shannon information capacity (C_{opt}) and the optimized bit error rate (BER) in SSPP channel at $T = 300K$ with the variation of groove length. The channel length is taken as the characteristic traveling length (l_t) for the corresponding groove length. The data is plotted for maximum attainable SNR at the receiver end within thermal noise limit of the channel. The geometric ratio a/d of the SSPP channel is taken as 0.1.

3.7 Summary of this chapter

In a nut shell, the present chapter comprises an information theory adopted for spoof plasmon channels which promise to be an energy-economic solution to traverse the broadly-discussed 'last centimeter' distance between two chips. This is a unique solution for centimeter scale data transfer that combines the advantages of both optical and electrical nature. The purpose of my analyses is to reveal and quantify the interplay between various parameters related to the information transfer process through a compact data-bus of spoof plasmon channel. A part of my work addresses the optimization of the bandwidth density and signal propagation length. My analysis shows that the best way of maximizing bandwidth density is to design SSPP channels

with the groove length comparable to half of the period of the structure, leading to ~ 1 Gbps/μm bandwidth density with the signal propagation length ~ 10 mm, and ~ 300 Gbps speed per channel. An effective resistivity of the quasi-optic SSPP channel has been introduced and used for the analysis of the noise characteristics of the channel at a given temperature. In the limit of thermal noise generated by SSPP channel, I quantitatively demonstrated that an interplay exists between maximization of Shannon information capacity of the channel and the probability of bit error for digital data transfer via spoof plasmon channel. This work may lay a foundation for the novel and prospective technique of spoof plasmon based inter-chip communication to facilitate the next generation fast and reliable data transfer process with high signal integrity.

CHAPTER IV

Spoof Plasmonics for Signal Modulation

4.1 Introduction

In order to transmit digital data over SSPP channel through high frequency modulation mechanism, we need to find a way of modualating the transmission property of the SSPP channel (see Fig. 4.1). In microwave wireless communications, we usually switch the carrier source by the data generator. However, in case of SSPP channel assisted data transfer, we target to send information through densely packed parallel bus, where each channel of the bus may share the same carrier frequency at a time. Therefore, for SSPP data-bus, we have to modulate the transmission property of the channels rather than switching the oscillator, so that each channel of the data-bus can independently be controlled. This chapter discusses some potential mechanism of modulating the transmission co-efficient of the SSPP channel.

In this chapter, my goal will be finding a way so that we can dramatically alter the transmission property of SSPP channel by introducing minimal change in its physical state. Our novel technique of spoof plasmon mode modulation will rely on the existance of electromagnetic bandgap in spoof plasmon channel.

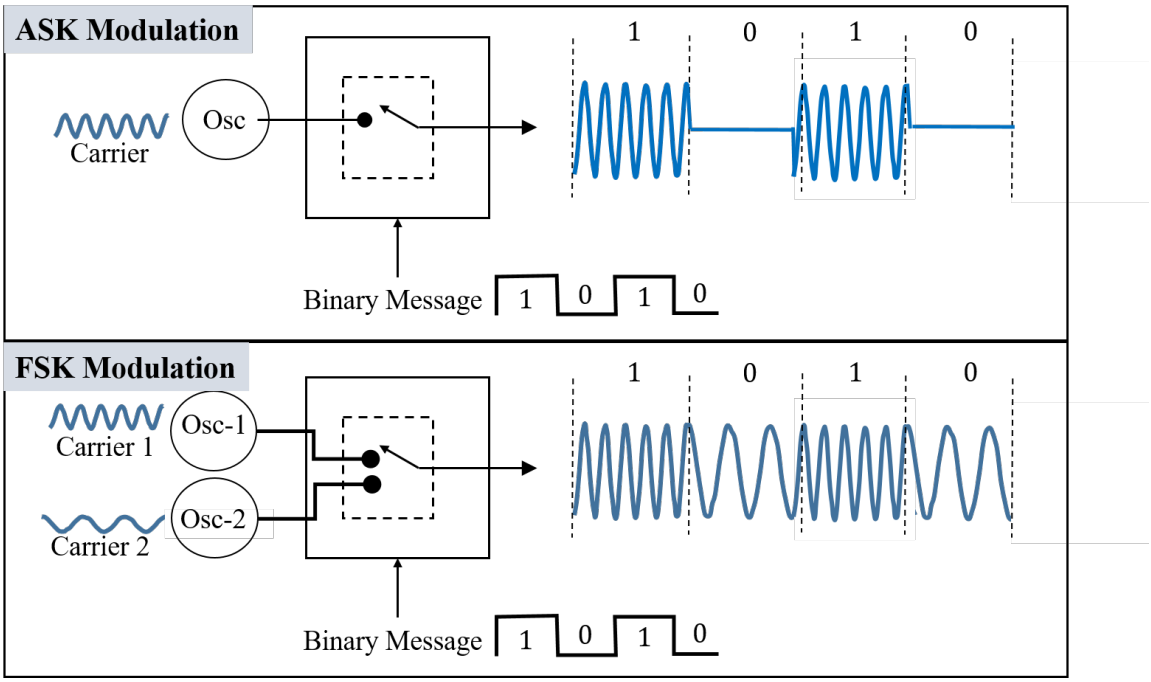

Figure 4.1: A generic block diagram of digital signal modulation scheme: amplitude shift keying (ASK) and frequency shift keying (FSK)

4.2 Background studies: design of modulator

A standard practice of designing high speed modulator is to couple the waveguide with a resonator, and then change the resonant frequency ω_r by altering the electromagnetic property of the resonator. This technique capitalizes the fact that the transmission of a resonator coupled waveguide at a given frequency ω is ultra-sensitive to the change of ω_r. Fortunately, spoof plasmonic waveguide is intrinsically made of quarter wavelength resonators, giving us an opportunity to design modulator by changing the resonance frequency of the in-built resonators. However, an SSPP waveguide consists of periodic resonators; and we definitely cannot afford to control a large number of resonators– as this would result in issues with synchronization and large footprint of modulator. Thus the question remains as to how many of those resonators' property we have got to change in order to make a modulator with high extinction (ON/OFF) ratio.

It is a commonly held belief that an effective medium description of a metastruc-

ture breaks down as the number of functional elementary cells becomes too small (*Wu et al.* (2014)). In contrast to this argument, I show here that spoof surface plasmon polariton (SSPP) structures, consisting of narrow grooves with sub-wavelength width on a plain metal surface [see Fig. 4.2(a)], can preserve the same 'effective medium' description even when the size of the structure is reduced down to minimal number of unit cells. This facilitates building a very short and simple 1D SSPP grating structure, which is able to manifest excellent mode confinement quality, i.e., high Q-factor ($\sim Q_{max} \approx 10^5$) and high Purcell factor. The structure is simple in the sense that it does not require high index or negative index medium. Additionally, the spoof plasmon states defined by dispersion relation medium are well preserved in finite structures, as periodicity plays a very nominal role in determining its propagation character, which is in strong contrast to crystal structures (*Noda et al.* (2000)) in general.

One of the standard technique of controlling signal transmission in waveguide is the incorporation of pre-engineered defects in plasmonic (*Cai and Shalaev* (2010); *Engheta and Ziolkowski* (2006)) and photonic structures (*Yablonovitch* (1993)). High speed modulation, coherent electron-photon interactions (*Wallraff et al.* (2004)), ultra-small filters, low threshold lasers (*Lu et al.* (2012); *Wu et al.* (2015)), photonic chips, multiplex biosensing (*Anker et al.* (2008)) and quantum information processing (*Akimov et al.* (2007)); all these sophisticated applications almost invariably seek for a mode confining structure with both high quality factor, Q, and small modal volume, V.

For example, a point defect embedded into a large array of photonic crystal can yield a high-Q resonant mode inside the photonic bandgap. However, many applications require devices with stringent conditions of small sizes. In those cases, the wavelength scale photonic-crystal based device falls markedly short of, especially at low frequencies. Meta-materials, with their ability to offer deep subwavelength confinement (*Han et al.* (2008); *Smith et al.* (2004)), stand out to be better candidates

for small devices. Efforts for making a small cavity size of good quality have so far resorted to embed the defect in a large array of unit cells, the number of cells reaching an order of 10^2 or even higher (*Minkov and Savona* (2014); *Gan et al.* (2013); *Lemoult et al.* (2013)). The reasons are apparent. In both photonic crystals or metamaterials, the resonant mode lies inside the bandgap of a host structure formed as a result of interference of multiple scattered waves. Therefore, one has to leave a long chain of unit cells around the defect in order to reproduce the effect of periodic structure. Reports on appearance of bandgap in disordered metamaterials also resort to a large ($\approx 10^2$) number of unit cells to host a defect (*Kaina et al.* (2013)). High quality mode proposed or realized by far, thus, inexorably bring large structures.

4.3 Author's contribution in the field of controlling spoof plasmon

My observations of the properties of an SSPP waveguide reveals a staggering fact. The transmission and dispersion characteristics of these waveguides obliviate the need for a long structure. In fact, a single unit cell suffices to conserve the main electromagnetic scattering properties of a periodic structure. This can enable to realize a high-Q resonant tunneling of spoof plasmon mode in a very short host medium. I illustrate this observation by considering a chain of three unit cells of a SSPP waveguide, with the left and right grooves having groove height h_h, and the groove at the middle having height h_d. I show that, for $h_d \neq h_h$, a resonant tunneling mode inside SSPP bandgap is formed. Thus, we can reduce the entire structure of 'a defect in host' system to its minimal possible length. In the subsequent sections, I shall refer to this minimal length 'host-defect-host' hetero-junction system as a (1–1–1) structure. The first part of this chapter discusses, how the incorporation of a pre-engineered defect structure in the spoof plasmon waveguide can provide means

to control the transmission property of the channel. The second part of this chapter discusses how the dynamic alternation of the waveguide's transmission is possible to realize by incorporating transistors in each of the defect cells, and develped a theoretical model for the dispersion behavior of the transistor incorporated spoof plasmon waveguide. Based on my developed model, I analyzed various crucial figure-of-merits of this newly proposed mechanism of the modulation of spoof plasmon signal: such as modulation speed and extinction ratio.

4.4 Transmission spectra of homogeneous and heterogeneous structures

The schematic of the structure under study is presented in Fig. 4.2(a). Periodic structures were a subject of intensive research *Ho et al.* (1990); *Joannopoulos et al.* (1997); *Astratov et al.* (1999); *Barnes et al.* (2003a) and their basic properties are well established. The SSPP dispersion diagram in a periodic structure is presented in Fig. 4.2(b). The gaps in the spectrum indicate the frequency regions where finite SSPP structures demonstrate subsided transmission as is illulstrated by spectra shown in Fig. 4.3(a): the transmission coefficient of the waveguide stays close to unity in a wide frequency range with slight modulation by Fabry-Perot ripples and shows strong reflection in the bandgap zone.

A thorough treatment of the optical response of a good conductor's surface with periodic narrow grooves shows that such structures are characterised by an effective Drude model with a spoof plasma frequency

$$\omega_p = \frac{\pi c}{2h\sqrt{\epsilon}}, \tag{4.1}$$

where h is the height of the grooves, c is the speed of light in vacuum and ϵ is the dielectric function of the medium filling the groove. It should be emphasized that

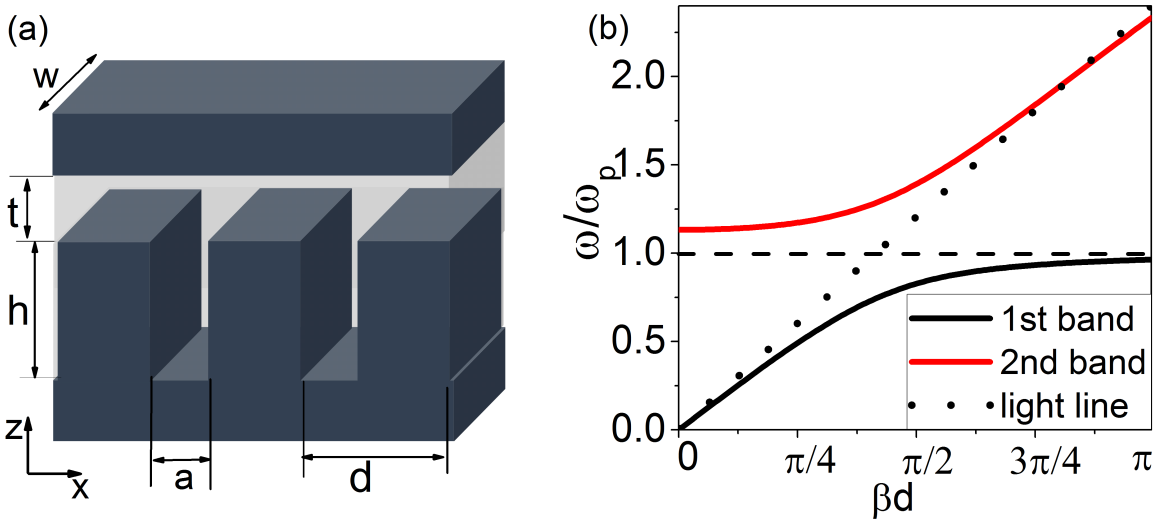

Figure 4.2: (a) The geometry of a homogeneous SSPP structure. The dark regions of the schematic are metal and light regions are dielectric. (b) The dispersion diagram of a periodic SSPP waveguide with $h/d \sim 1$, $t/d \sim 0.3$, $a/d \sim 0.1$, and $w \sim \lambda$. The frequency is normalized by the spoof plasma frequency $\omega_p = \pi c/2h$. The bands are formed due to anti-crossing between light-line and ω_p. For $2h \gg d$, the anti-crossing happens far away from the Brillouin zone boundary.

this frequency does not derive from material properties, but from the geometry of the structure. Generally, taking into account the higher resonances, the n-th spoof plasma frequency can be written as

$$\omega_p^{(n)} = (2n-1)\omega_p, \tag{4.2}$$

with $n = 1, 2 \ldots$.

Figure 4.3(a) shows that the major characteristics of transmission spectra of a long periodic SSPP waveguide successfully retains in a finite waveguide even when its size is reduced to a single unit cell. This result implies the immunity of SSPP waveguide's dispersion to finite size-effects. Manifestation of this transmission-dip or anti-resonance of a cell with a single groove is utilized to propose band-stop filter in other works as well*Lin and Huang* (2008), albeit in a different context not related to spoof plasmon concept. In-fact, the attenuated transmission around cavity reso-

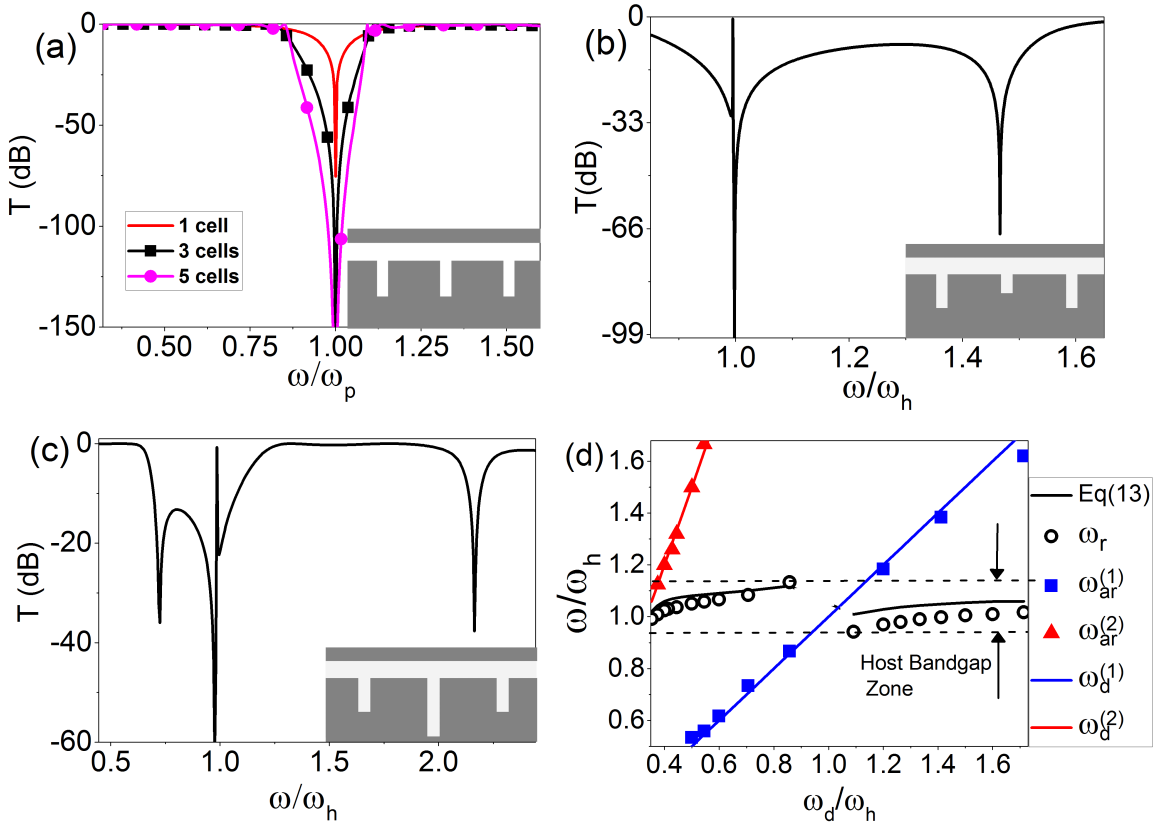

Figure 4.3: (a) Transmission spectra of homogeneous SSPP waveguides with different number of unit cells. Inset shows the corresponding SSPP structure. (b,c) Transmission spectra of heterogeneous structures with the defect cells characterized by $h_d/h_h = 0.75$ and $h_d/h_h = 1.25$, respectively. Anti-resonances (transmission dips) at $\omega/\omega_d \neq 1$ are induced by zeroth and higher order spoof plasmon resonance modes of defect cells. In addition, a transmission resonance emerges inside the bandgap. The insets show corresponding heterogeneous geometry. (d) Trajectories of transmission resonance (ω_r) and anti-resonances ($\omega_{ar}^{(1)}$ and $\omega_{ar}^{(2)}$) in heterogeneous SSPP structures as functions of the spoof plasma frequency of the defect cell. The solid black curves are loci of transmission resonances obtained via Eq. (4.13). Note that, the locus of transmission resonances ω_r demonstrates discontinuity around $\omega_d/\omega_h \sim 1$, as at this condition, the SSPP structure becomes homogeneous and contains no resonance inside bandgap. The dots of ω_r and $\omega_{ar}^{(n)}$ show the loci of the resonance and the n-th antiresonance, respectively, obtained from the full-wave simulation.

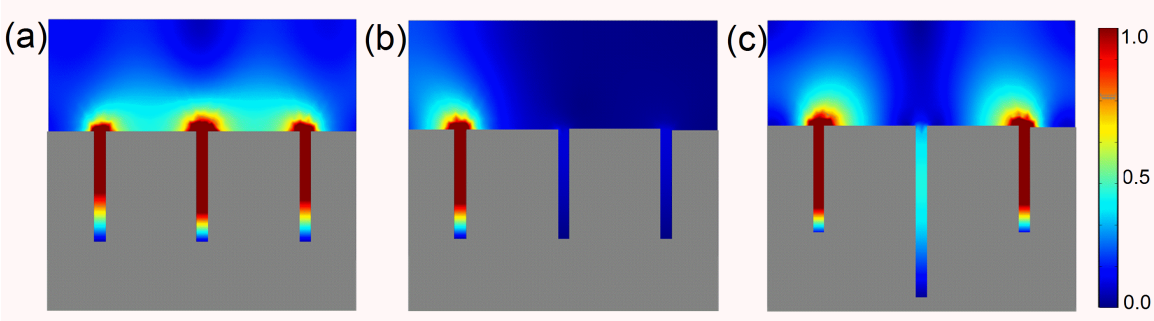

Figure 4.4: The field distribution inside a three-cell structure with incoming wave from the left side. (a) Propagating SSPP mode in a homogeneous structure at a frequency corresponding to pass-band. (b) Non-propagating SSPP at a frequency inside the stop-band. (c) Resonant tunneling SSPP mode in a heterostructure incorporating a defect cell in the middle.

nant frequency is a characteristic of a laterally coupled waveguide-cavity system in general*Fan* (2002). Here, however, we emphasize that, a single cell of spoof plasmon waveguide yields not only the 'bandgap effect' but also the 'dispersion effect' of a periodic waveguide.

To demonstrate the above mentioned phenomenon, we study the transmission behavior of a composite (1–1–1) structure made of three unit cells of SSPP waveguide, all but the middle unit cell having groove height h_h. We shall call the middle cell a 'defect' with groove height $h_d \neq h_h$ embedded in a host medium. The term 'defect' in this context means an intentional breaking of translational symmetry of an otherwise regular structure. As we will show, the transmission property of the composite medium can be successfully explained by considering each of the single host and defect cells as an effective individual SSPP medium, characterized by ω_h and ω_d spoof plasma frequencies, respectively. To put differently, the effective medium description of SSPP metastructure is valid for a single cell as well. The apparently simple concept has far greater significance than being of a mere theoretical interest. This helps in designing, as we shall show, a very short spoof plasmon structure with giant Q-factor and Purcell factor, which is remarkable from application point of view.

The transmission spectrum of the composite structure is a result of interplay

between characteristic frequencies describing states of the field in periodic structures made of either host or defect unit cells. A straightforward impact of series addition of a new functional cell to a background regular SSPP waveguide is added spectral filtering (Fig. 4.3b,c). Due to short attenuation length, as is demonstrated in Fig. 4.4(b), each cell acts as a band-rejection notch filter which suppresses transmission around its own spoof plasma frequency ω_p.

A non-trivial case of transmission resonance as well may arise for a specific configuration of the composite SSPP system: structure with a defect cell inserted in the middle of a regular host waveguide. In this case, the narrow transmission resonance [see Fig. 4.3(b,c)] corresponding to a resonant tunneling, would emerge inside the host SSPP bandgap. The characteristic field distribution of this special resonant tunneling mode is shown in Fig. 4.4(b). Figure 4.3(d) depicts the trajectories of the transmission resonances ω_r and anti-resonances ω_{ar} with variation of ω_d. In the next section, we show how the numerically obtained trajectory of ω_r and ω_{ar} in a (1–1–1) composite structure can be explained by describing the propagating state in each single cell as spoof plasmon mode. In this regard, it should be emphasized that, as Fig. 4.4 demonstrates, all modes, propagating, non-propagating and resonant tunneling, are concentrated close to the surface of the structure. Appearance of such kind of resonant tunneling mode of spoof plasmon with high Q-factor supported by SSPP in short structures is the principle message of the present work.

4.5 SSPP scattering in heterogeneous structures

Despite significant efforts invested into theoretical studies of SSPP, a full yet tractable description of the propagation of spoof plasmons in finite structures is yet to be developed. Basic transport properties of such structures, however, can be understood within a simplified picture based on the assumption that the propagation within a single cell can be effectively characterized by a Bloch wavenumber and imposing

continuity on average conditions at the interfaces between different cells.

In what follows, we will denote host and defect cells with subscripts 'h' and 'd', respectively. Retaining a single mode, the electric and magnetic fields can be presented as

$$H_y = e^{iq(\omega)z}\{f_+ e^{i\beta(\omega)x} + f_- e^{-i\beta(\omega)x}\} \tag{4.3}$$

$$E_z = -\frac{\beta(\omega)}{\omega\epsilon} e^{iq(\omega)z}\{f_+ e^{i\beta(\omega)x} - f_- e^{-i\beta(\omega)x}\}, \tag{4.4}$$

where the coordinate axes are chosen as shown in Fig. 4.2(a), f_+ and f_- are amplitudes of the waves propagating forward and backward, respectively, $q(\omega) = \sqrt{(\omega/c)^2 - \beta^2(\omega)}$ is the transverse wavenumber and $\beta(\omega)$ is found for the host and defect cells from the respective dispersion equations $D_{h,d}(\omega, \beta) = 0$, where *Xu et al.* (2012a)

$$D(\omega, \beta) = \frac{q}{\omega/c}\tan(qt) + \frac{a}{d}\mathrm{sinc}^2(a\beta/2)\tan(\omega h/c). \tag{4.5}$$

The possibility to characterize the state of the electromagnetic field within a single cell with the help of dispersion equation (4.5) is suggested by the following consideration. In a typical periodically perturbed system, say a photonic crystal, the corresponding band diagram can be obtained by replicating the dispersion diagram of the background at each reciprocal lattice site. The replicated diagrams intersect at the boundary of the Brillouin zone and the cross-resonance between them leads to opening a gap between the bands. Figure 4.5(c) shows how the gap formation occurs in a typical photonic crystal. Periodicity thus playes the most crucial role for bandgap formation in photonic crystal. Far away from the boundary of the Brillouin zone, the band modification due to periodicity is weak. Bandgap in spoof plasmon, however, is born of a different type of mode coupling. The coupling here occurs between states inside the groove and that outside the groove. The mechanism of SSPP bandgap creation due to cross-over between the light-line in dielectric outside of the groove

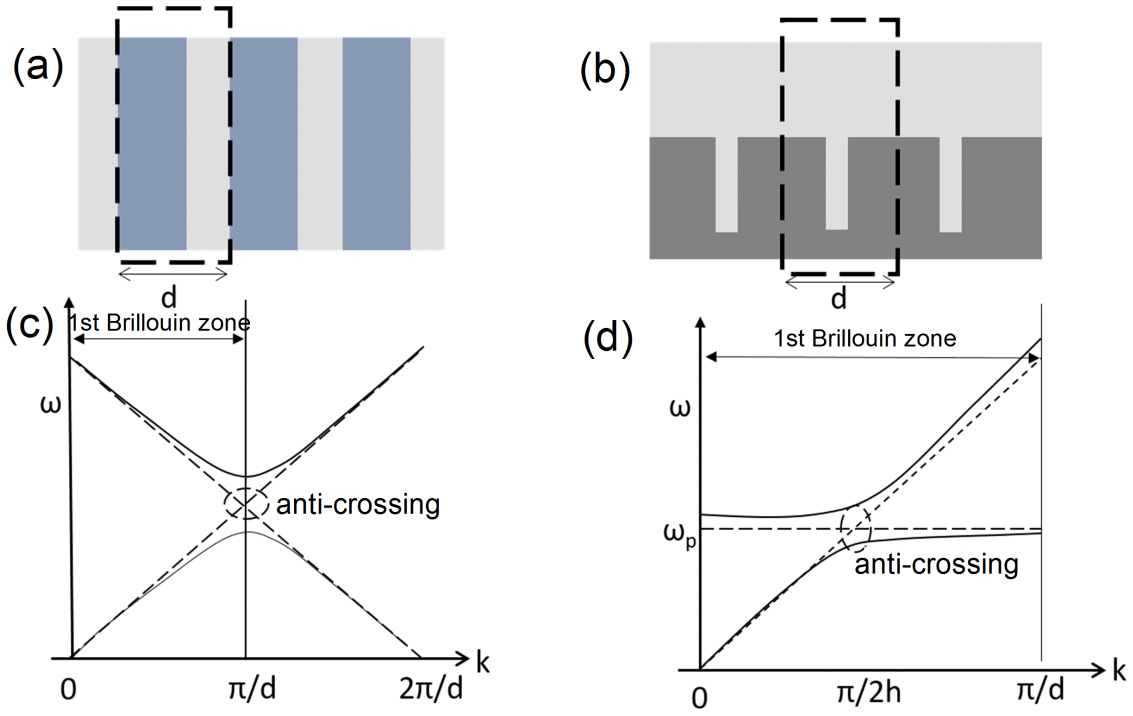

Figure 4.5: (a,b) 1D photonic crystal and SSPP structure, respectively. The dashed box indicates the unit cells and periodicity d. (c,d) Band diagrams of a photonic crystal and a SSPP periodic waveguide, respectively. Anticrossing (dashed circles) between bands of the perturbed background (dashed lines) leads to formation of new bands (solid lines). For the SSPP, the anticrossing location ($k = \pi/2h$) must occur far away from the boundary of the Brillouin zone in order to have well developed SSPP. As a result, SSPP modes are immune to broken periodicity and withstand the finite size effect.

and the resonant mode inside the groove at frequency ω_p is shown in Fig. 4.5(d). We notice that, well-defined SSPP are formed when $h > d/2$*Erementchouk et al.* (2016a), which holds when the intersection between light-line and the resonant mode is far from the boundary of the Brillouin zone. Thus, in well-defined SSPP supporting structure, periodicity becomes a nominal concern for band formation, and one can regard Eq. (4.5) as describing an effective medium even for a very short SSPP structure with minimal number of cells.

Assuming that the interface between the cells is situated at $x = 0$, the continuity on average condition for the tangential component of the electric field at the interface has the form

$$\int_0^t E_{z(d)}|_{x=0} dz = \int_0^t E_{z(h)}|_{x=0} dz, \tag{4.6}$$

while the continuity of the total energy flux across the interface leads to

$$\int_0^t E_{z(d)} H^*_{y(d)} dz = \int_0^t E_{z(h)} H^*_{y(h)} dz. \tag{4.7}$$

Enforcing these conditions, we obtain the transfer matrix for the interface between host and defect cells

$$\begin{pmatrix} f_{h+} \\ f_{h-} \end{pmatrix} = \frac{1}{2} \begin{pmatrix} t_1 & t_2 \\ t_2 & t_1 \end{pmatrix} \begin{pmatrix} f_{d+} \\ f_{d-} \end{pmatrix} = T_{hd} \begin{pmatrix} f_{d+} \\ f_{d-} \end{pmatrix}.$$

Here $t_i = A - (-1)^i \beta_d / A\beta_h$ and, for small arm thickness t, one has $A = \dfrac{q_d}{q_h} \dfrac{e^{iq_h t} - 1}{e^{iq_d t} - 1} \approx 1$. Here q_d and q_h are transverse wavevectors of the defect and host cells, respectively.

An SSPP structure with a defect cell in the middle is described by the transfer matrix

$$T = T_{eh} T_h T_{hd} T_d T_{dh} T_h T_{he}, \tag{4.8}$$

where $T_{dh} = T_{hd}^{-1}$, $T_{h,d} = \mathrm{diag}\left(e^{i\theta_{h,d}}, e^{-i\theta_{h,d}}\right)$, with $\theta_{h,d} = \beta_{h,d}d$, are the transfer matrices through the host and defect cells, and $T_{eh} = T_{he}^{-1}$ are the transfer matrices between the SSPP structure and enviornment, which we will take in the form of an interface transfer matrix

$$T_{eh} = \frac{1}{2}\begin{pmatrix} s_1 & s_2 \\ s_2 & s_1 \end{pmatrix}, \tag{4.9}$$

with some parameters $s_{1,2}$, the specific form of which is of low importance for the following.

Since we are interested in the frequency range inside the bandgap of the host structure, where $\beta = i\kappa_h$, we present $\theta_h = iNd\kappa_h$, where N is the number of host cells on either side of the defect cell; and obtain from Eq. (4.8) the transmission coefficient

$$t = \frac{16e^{i\theta_d}s_1s_2t_1t_2}{e^{2\kappa_h N}\mathcal{D}^{(+)} + e^{-2\kappa_h N}\mathcal{D}^{(-)} + \mathcal{D}^{(0)}}, \tag{4.10}$$

where

$$\begin{aligned} \mathcal{D}^{(\pm)} &= (s_1 \pm s_2)^2\left[(t_1 \pm t_2)^2 - e^{2i\theta_d}\left(t_1 \mp t_2\right)^2\right], \\ \mathcal{D}^{(0)} &= 2(1 - e^{2i\theta_d})\left(s_1^2 - s_2^2\right)\left(t_1^2 - t_2^2\right). \end{aligned} \tag{4.11}$$

The resonant tunneling occurs at frequency, where the exponential attentuation of the transmission with the length of the host cancels. This yields

$$\mathcal{D}^{(+)}(\omega) = D_+(\omega)D_-(\omega) = 0, \tag{4.12}$$

where $D_\pm(\omega) = t_1e^{-i\theta_d/2} \pm t_2e^{i\theta_d/2}$. Using the obtained transfer matrices, it can be shown that $D_+(\omega) = 0$ and $D_-(\omega) = 0$ define frequencies of states confined to the defect cell embedded into an infinite host structure, even and odd with respect to the center of the defect cell, respectively. It's not difficult to see, however, that $D_+(\omega) = 0$ does not have solutions inside the first Brillouin zone. Thus, the resonant

transmission is supported only by odd local states, or when

$$\frac{\beta_d(\omega)}{\kappa_h(\omega)} = \cot\left(\frac{d\beta_d(\omega)}{2}\right). \tag{4.13}$$

Basic features of the transmission resonance can be discussed directly on the base of Eq. (4.13) taking into account that inside the band gap above host spoof plasma frequency ω_h, (i.e., $\omega_h < \omega < \omega_h^{(H)}$), we have

$$\kappa_h = \frac{\omega}{c}\sqrt{\frac{\omega_h^{(H)} - \omega}{\omega - \omega_h}}. \tag{4.14}$$

Here, $\omega_h^{(H)}$ is the upper frequency edge of the SSPP bandgap, which is found to be

$$\omega_h^{(H)} = \omega_h\left(1 + \frac{4ah}{\pi^2 dt}\right). \tag{4.15}$$

As the height of the groove in the defect cell increases, the transmission resonance ω_r emerges near $\omega_h^{(H)}$ and moves deeper into the host bandgap ($\omega_h^{(H)} - \omega_r \sim \sqrt{h_d - h_h}$). Defect cell with shorter groove can be of particular interest, however. It yields resonant state with evanescent transverse field profile in defect cell. The surface bound resonant mode for shorter defect groove may be exploited to design a high-Q cavity with no physical enclosure around defect cell. The comparison of the analytical estimation following from Eq. (4.13) and the numerical results is provided in Fig. 4.3(d). The very well agreement with the numerically obtained data validates the concept that spoof plasmon mode can survive even in a short meta-structure consisting of minimal number of cells. It should be noted that when the resonance frequency ω_r approaches ω_h, the point $\beta_d(\omega_r)$ gets close to π/d, where the characterization of the state of the electromagnetic field inside the defect cell in terms of dispersion equation (4.5) is no longer valid and Eq. (4.13) breaks down.

We conclude this section with a note about the defect induced anti-resonances in

transmission spectra, for instance, at $\omega/\omega_h \approx 1.45$ in Fig. 4.3(b) and at $\omega/\omega_h \approx 0.7$ and 2.2 in Fig. 4.3(c). They, as well, can be studied using Eq. (4.10). It's not difficult to see that they emerge at frequencies inside the stop-band of the defect cell. As a result, with the variation h_d, they follow defect cell spoof plasma frequencies, $\omega_d^{(n)}$.

4.6 Q-factor and enhanced radiation rate

We consider two figures of merit for the resonant mode inside the SSPP bandgap: the Q-factor and the Purcell factor. In a defect incorporated finite waveguide, for a given frequency inside the bandgap, the fraction of power scattered out through the structure can be written as

$$|t|^2 \sim e^{-4\kappa_h dN}. \tag{4.16}$$

As the Q-factor is inversely proportional to the power radiated out of the structure, taking into account Eq. (4.14) for κ_h, we can estimate for frequencies not too close to ω_p

$$\log Q \sim N\sqrt{\frac{\omega_h^{(H)} - \omega_r}{\omega_r - \omega_h}}. \tag{4.17}$$

As has been discussed above, with gradually changing the height of the groove in the defect cell, the resonance frequency approaches ω_h, which results in significant increase of κ_h, yielding very high quality modes localized on the defect cell.

Figure 4.6a shows how the quality factor changes with the variation of the defect's spoof plasma frequency. The fact that electromagnetic transmission essentially stops at ω_h results in exponential increase of the Q-factor. Thus, a very high quality resonating mode is possible to realize in a SSPP host medium consisting of only a single groove on each side of the defect cell. Although the divergence in Eq. (4.17) is an artifact of the approximation retaining only single mode inside the grooves, the COMSOL MULTIPHYSICS full-wave simulation justifies very high Q-factor in the (1–1–1) structure, which hits a maximum of value of 10^5 when resonant mode

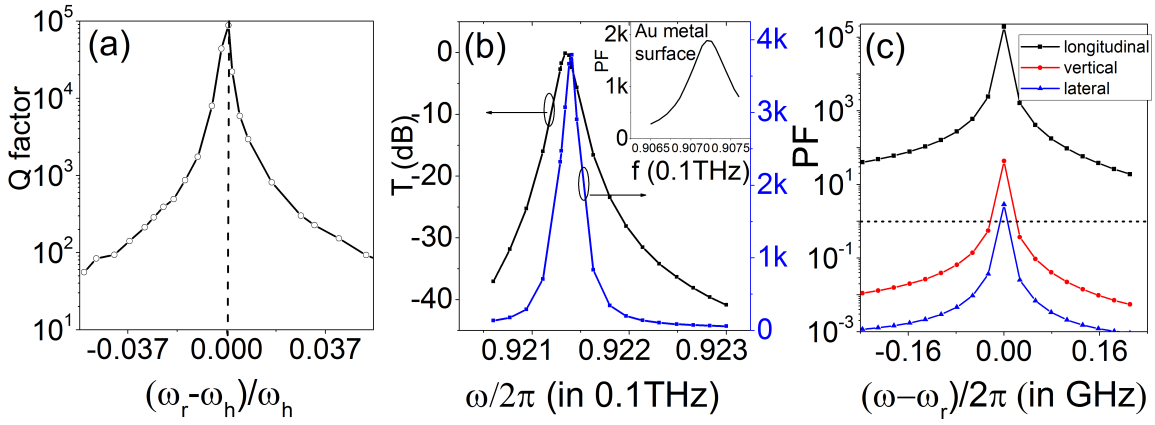

Figure 4.6: (a) The Q-factor as a function of the difference between resonant mode and host's spoof plasma frequency. Physical height of each grooves = 0.8 mm, period = 1 mm, arm = 300 μm, defect's optical height = 2.5mm. (b) The Purcell factor, F_p, in the limit of perfect electric conductor in the (1–1–1) heterostructure is plotted together with the transmission spectrum. Inset shows the Purcell factor around the resonant frequency for a structure of the same geometry but with Au metal surface. (c) The Purcell factor in (1–1–1) SSPP heterostructure with the above mentioned geometry for source with three different dipole orientations, positioned near the groove opening in the defect cell. The region above the dotted line corresponds to $F_p > 1$.

frequency coincides with the host spoof plasma frequency ω_h.

4.7 Dynamic switching of SSPP transmission property

While the previous sections discuss how can we get resonant mode in SSPP waveguide with high quality factor, we are yet to discuss how this property can be leveraged to make modulators, i.e., how to dynamically alter the effective height of the groove.

There are two possible options for dynamic modification of effective groove height:

- by loading the interior of the groove with electro-optic material, such as lithium niobate ($LiNbO_3$) that shows Kerr effect, and applying voltage to get the electro-optic effect.

- by placing transistors across each of the grooves of spoof plasmonic waveguide. Switching the transistors ON or OFF can drastically alter the effective resonating length of grooves.

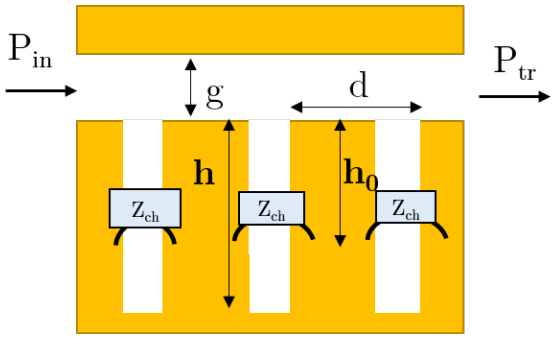

Figure 4.7: Schematic of SSPP waveguide with arm and external impedances connected at every cell.

While the first option is commonplace in the design of optical modulator, the second one is yet unexplored. In addition to that, the second approach does not rely on finding a right material with desired electro-optic property, and hence can considerably simply the design strategy. In the subsequent sections, I will discuss spoof plasmon modulation strategy based on the second approach.

4.7.1 Modal Analysis of SSPP with external impedance

Figure 4.7 gives the schematic view of the SSPP waveguide with the inclusion of external impedances. We shall insert a variable resistor Z_{ch} at some position ($z = -h_0$) of the groove, where the groove has a physical length of h.

Then, at $y = -h_0$, looking into the groove, we can express the total impedance as $Z_{in} = Z_{ch}||Z_1$ in terms of the ratio of tangential electric and magnetic field, where Z_1 is the impedance of the groove at position $y = -h_0$ in absence of the shunt path Z_{ch}.

$$Z_1 = \frac{E_{g,x}}{H_{g,z}} = -i\frac{\omega\mu}{Q_0}\tan(Q_0(h - h_0)) \tag{4.18}$$

here $Q_m + (\frac{m\pi}{a})^2 = (\frac{\omega}{c})^2$.

If the wave inside the groove is split into two parts, forward and backward wave, with amplitude G_{m+} and G_{m-} respectively, and $m = 0$ mode is assumed to be domi-

nant, then the impedance Z_{in} can be related to the wave magnitudes as,

$$\left.\frac{E_{g,x}}{H_{g,z}}\right|_{y=-h_0} = \frac{G_{0+}e^{iQh_0} + G_{0-}e^{-iQh_0}}{Q/(\omega\mu) \times (G_{0+}e^{iQh_0} - G_{0-}e^{-iQh_0})} = Z_{in}$$

which implies the following

$$G_{0+} = G_{0-}re^{i\theta}$$

where $r = \dfrac{\tilde{Z}_{in}+1}{\tilde{Z}_{in}-1}$, $\tilde{Z}_{in} = \dfrac{QZ_{in}}{\omega\mu}$ being the normalized input impedance, and $\theta = -2Qh_0$.

Then, for an SSPP waveguide with groove width a, period d, and a gap g between the waveguide and the lid, the relation between transverse wave-vector $k_y^2 = (\frac{\omega}{c})^2 - \beta^2$ and the frequency ω is following:

$$k_y = k_y' + ik_y'' = i\frac{\omega}{c}\frac{a}{d}\,\mathrm{sinc}^2(\frac{a\beta}{2})\cot(k_y g)\frac{1+re^{i\theta}}{1-re^{i\theta}} \tag{4.19}$$

4.8 Estimation of Bandgap

We can estimate the bandgap in SSPP waveguide transmission from Eq. 4.19. For an intrinsic SSPP waveguide with lid on top of it (i.e., no external impedance Z_{ch}), Eq. 4.19 simplifies to the following:

$$k_y = -\frac{\omega}{c}\frac{a}{d}\,\mathrm{sinc}^2(\frac{a\beta}{2})\cot(k_y g)\tan(Qh) \tag{4.20}$$

For the convenience of analysis, the bandgap around the resonant frequency $\omega_{sp} = \dfrac{\pi}{2}\dfrac{c}{h}$ can be divided into two parts: the gap below ω_{sp}, and the gap above it.

For the lower bandgap part, the band-edge frequency is:

$$\omega_e = (\frac{\pi}{2} - \delta_L)\frac{c}{h}, \tag{4.21}$$

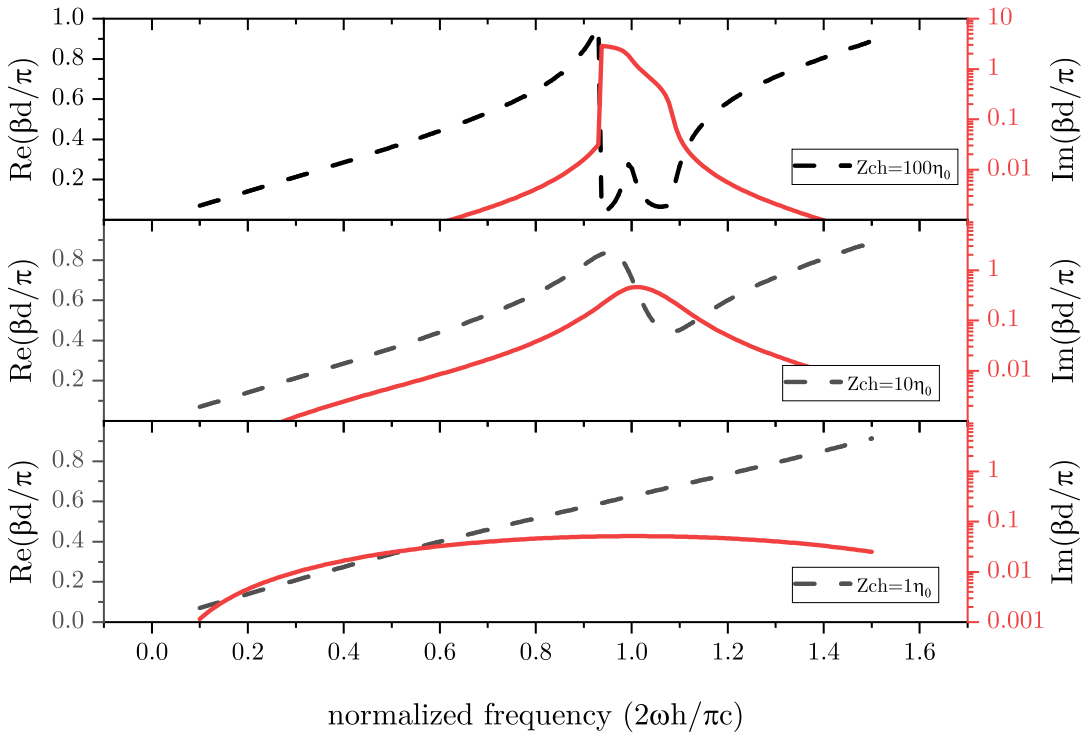

Figure 4.8: Real and imaginary part of longitudinal wave-vector in SSPP waveguide for different value of Z_{ch} attached to the mouth of the groove. SSPP waveguide geometry : a/d=1/10, a/h=1/8, a/g=1/3. With the continual change of Z_{ch} from a very high value to very low value, the bandgap existing around spoof plasmon frequency disappears, and the waveguide becomes an all-pass medium.

where δ_L is the detuning from resonant frequency. If δ_L is small, then $k_y(\omega_e)^2 \approx (\frac{\pi}{2h})^2 - \beta(\omega_e)^2 = (\frac{\pi}{2h})^2 - (\frac{\pi}{d})^2$, and $\tan(Qh) \approx \frac{1}{\delta_L}$. Thus the lower bandgap is

$$\delta_L \approx \frac{\pi}{2}\frac{a}{d}\frac{\coth(\kappa_e g)}{\kappa_e h} \tag{4.22}$$

where $k_y = i\kappa$ and $\kappa_e = \kappa(\omega = \omega_e) = \sqrt{(\frac{\pi}{d})^2 - (\frac{\pi}{2h})^2}$

On the other hand, the upper part of the bandgap can be estimated by finding the frequency (ω_u) of the next higher band at which $\beta = 0$ (i.e., $k_y = \frac{\omega}{c}$). If the detuning δ_u of the frequency $\omega_u = \omega_{sp} + \delta_u \frac{c}{h}$ from the resonant frequency ω_{sp} is also considered small, then setting $k_y = \frac{\omega}{c}$ in Eq. 4.20 with the approximation of

$\tan(Qh) = \tan(\frac{\pi}{2} + \delta_u) \approx -\frac{1}{\delta_u}$ yields the following:

$$\delta_u \approx \frac{a}{d}\cot(\frac{\pi g}{2h}) \tag{4.23}$$

Thus the total bandgap Δ_g, in terms of Hertz (Hz), of an intrinsic SSPP waveguide with the lid on top of it is:

$$\Delta_g = (\delta_u + \delta_L)\frac{c}{2\pi h} \tag{4.24}$$

It is evident from Eq. 4.22 and 4.23 that, both of the lower bandgap and upper bandgap increases as g becomes smaller, i.e., the lid is moved closer to SSPP waveguide. Thus, the parameter g provides an extra degree of freedom to knob the bandgap of SSPP waveguide, which will be helpful in the design of high-speed SSPP modulator.

4.9 Design of SSPP modulator

In the previous section, we have seen how the inclusion of an external impedance can change the transmission properties of an SSPP waveguide. With that knowledge, now we shall design a modulator for a given SSPP waveguide. Despite an SSPP waveguide with a lid on top of it is excellent in transmitting signals from zero frequency to all the way up to spoof plasma resonant frequency, we have to keep in mind that, we shall eventually taper out the lid to leave SSPP as open structure, which can only transmit the high-frequency spectrum faithfully. (Remember that, the whole point of using SSPP is to employ an open structure that obviates the need of having external shielding conductor, and thus can free up some precious spaces on the electrical board ! An SSPP mode has an auto-immunity to cross-talk without the help of a lid/shielding conductor. Whereas, without a shielding conductor, an electrical interconnect heavily corrupts the signal at the high frequency end.)

Therefore, we shall design modulator which will alter the transmission at the high-frequency edge of an open structure SSPP waveguide. This can be achieved by joining the given SSPP waveguide of groove length h with a second SSPP waveguide of larger groove length h_m ($h_m > h$). From now on, we shall call the first SSPP waveguide as primary SSPP channel, and the second SSPP waveguide as modulating SSPP channel. The groove length h_m of the modulator SSPP channel along with the lid-gap g can be tuned together in order to get the desired speed of modulation at the chosen spectrum. To exemplify the design process, let us take an SSPP waveguide with groove length $h = 6$ mm, period $d = 6$ mm, and waveguide-to-lid gap $g = 3$ mm. The spoof plasma resonance of this waveguide will be at $f_{sp} = \omega_{sp}/2\pi = \dfrac{c}{\lambda_{sp}} = \dfrac{c}{4h} = 12.5$ GHz. The edge of the band of this SSPP waveguide can be found from Eq. 4.22 as $f_e = \omega_e/2\pi = \dfrac{c}{4h} - \dfrac{\delta_L c}{2\pi h} = 10.7$ GHz. Let us say, we want to transmit 2 Gbps data through SSPP waveguide by utilizing its spectral transmission window spanning from the band-edge $f_e = 10.7$ GHz to 8.7 GHz (Note that, $10.7 - 8.7$ GHz=2 GHz). Then the designed modulator should have a speed of 2 Gbps, and switching the modulator ON and OFF should greatly alter the transmission magnitude of SSPP waveguide in the spectral window of 8.7 to 10.7 GHz. If the $\dfrac{a}{d}$ ratio of the modulating SSPP channel is kept same as that of the primary SSPP channel, then we are left with only two parameters h_m and g_m to tune in order to meet the specification of the modulator, where g_m is the waveguide-to-lid gap in the modulator SSPP channel. Then we shall employ two equations, namely Eq. 4.24 and 4.21, coupled with 4.22 with the replacement of $\Delta_g = 2$ GHz and $\omega_e = 2\pi \times 8.7GHz$, and solve for g_m and h_m.

Figure 4.9 shows the transmission spectrum of homogeneous SSPP waveguide (upper graph), and that of heterogeneous SSPP waveguide (lower graph): where homogeneity refers to the structure of SSPP waveguide with identical groove length throughout. The upper graph shows how the position of bandgap can be tuned by

choosing a different length of groove in the waveguide. For the transmission spectrum in the lower graph of Fig. 4.9, the corresponding heterogeneous SSPP waveguide comprised of two homogoneous SSPP waveguides of different groove length, cascaded. Let us call the waveguide with groove length 6 mm as the primary waveguide, and the other waveguide with larger groove length (9 mm) as the auxiliary waveguide. It is evident that the nature of the transmission characteristics of a heterogeneous SSPP structure can be readily traced back to that of each of the constituent homogeneous waveguide. By carefully choosing various geometric parameters such as the groove length and lid-gap of the auxiliary SSPP waveguide, we appended the bandgap of the auxiliary waveguide to that of the primary waveguide, and thus lowered down the edge of the transmission band of the primary waveguide from $\sim$ 10 GHz to $\sim$ 7 GHz.

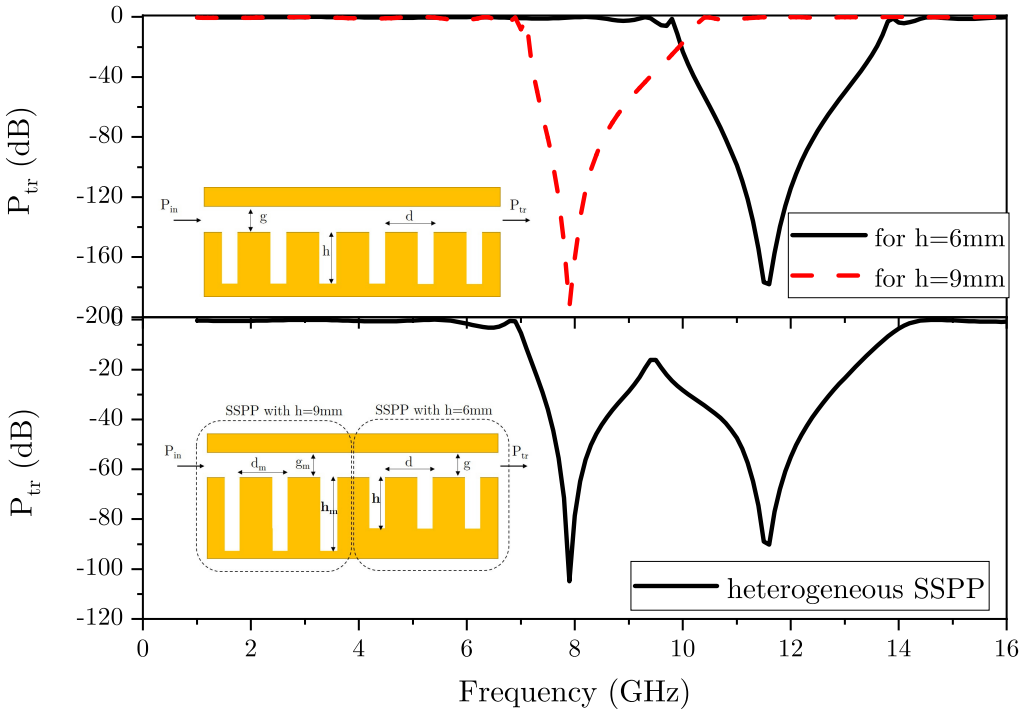

Figure 4.9: Transmission properties of homogeneous SSPP waveguide (upper figure) and heterogeneous SSPP waveguide (lower figure). The inset shows the corresponding structure of the waveguide.

In order to make dynamic change to the transmission band of the primary waveguide, we have attached an external impedance to the opening edge of each of the groove of the auxiliary waveguide. The impedance of the attached element can be controlled by a third terminal. The physical implementation of such an element with variable impedance can be a three-terminal transistor, such as MOSFET, with its drain and source making the bridge between two edges of a groove, while the gate terminal will be controlled by the voltage from the message signal. Altering the gate voltage around the threshold voltage of the transistor would change the impedance of the channel of the transistor, which in turn will alter the electromagnetic transmission property of the primary SSPP waveguide at the desired band. Figure 4.10 shows how the switching of the external impedance Z_{ch} between ∞ (open-circuit) to 0 (short-circuit) attached to each of the grooves of the auxiliary SSPP waveguide can sweep the edge of the transmission-window of the primary waveguide between 7 GHz and 10 GHz.

4.9.1 Speed of modulation: Rate of change of SSPP bandgap with channel impedance Z_{ch}

In the previous sections, we have discussed the fact that the bandgap of SSPP waveguide can be made disappear and re-appear by switching the channel impedance Z_{ch} of the attached transistors at the SSPP grooves between 0 and ∞. However, we are yet to discuss the most critical issue of modulation: the speed of SSPP signal modulation. The speed of modulation depends on two factors: the rate of change of channel impedance with the applied gate voltage ($\frac{\partial Z_{ch}}{\partial V_g}$), and the rate of change of bandgap of SSPP auxiliary waveguide with the change of channel impedance ($\frac{\partial \Delta_g}{\partial Z_{ch}}$). The preceding factor $\frac{\partial Z_{ch}}{\partial V_g}$ depends on the nature of the specific transistor technology employed in the SSPP modulator, and would not be discussed here. The later factor $\frac{\partial \Delta_g}{\partial Z_{ch}}$ merits some discussion in this thesis. Since, sweeping the value of impedance

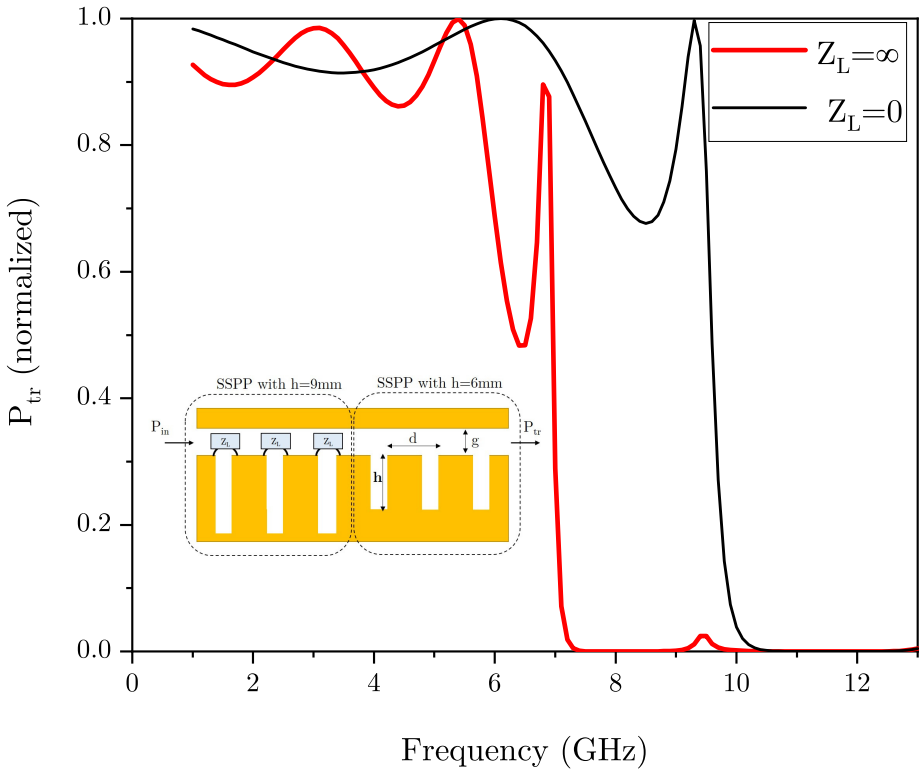

Figure 4.10: Dynamic change of transmission property of the primary SSPP wavegude by altering the impedance Z_{ch} attached to the grooves of the preceding auxiliary waveguide. Inset shows the corresponding structure of waveguide.

between 0 and ∞ would be impossible by all available practical means, in this section, we would discuss the differential rate of change of the bandgap with the change of Z_{ch} to figure out the minimum order of change in Z_{ch} we require to employ in order to toggle the signal between transmission-ON and transmission-OFF mode.

If the bridge element with impedance Z_{ch} is made at the mouth (i.e., $h_0 = 0$) of the grooves of SSPP waveguide, then the corresponding dispersion relation can be found from Eq. 4.19 by placing $\theta = -2Qh_0 = 0$,

$$k_y = i\frac{\omega}{c}\frac{a}{d}\,\mathrm{sinc}^2\left(\frac{a\beta}{2}\right)\cot(k_y g)\frac{1+r}{1-r} \tag{4.25}$$

with $r = \dfrac{\tilde{Z_{in}}+1}{\tilde{Z_{in}}-1}$, $\tilde{Z_{in}} = \dfrac{Q}{\omega\mu}(Z_{ch}||Z_1)$, and $Z_1 = -i\dfrac{\omega\mu}{Q}\tan(Qh)$, $Q = \dfrac{\omega}{c}$.

Setting different value of Z_{ch} in Eq. 4.25, and solving for the imaginary part of β for a typical SSPP waveguide yield Fig. 4.11, where the various geometric ratio is taken as follows: $\frac{a}{d} = \frac{1}{10}$, $\frac{a}{h} = \frac{1}{8}$, $\frac{a}{g} = \frac{1}{3}$.

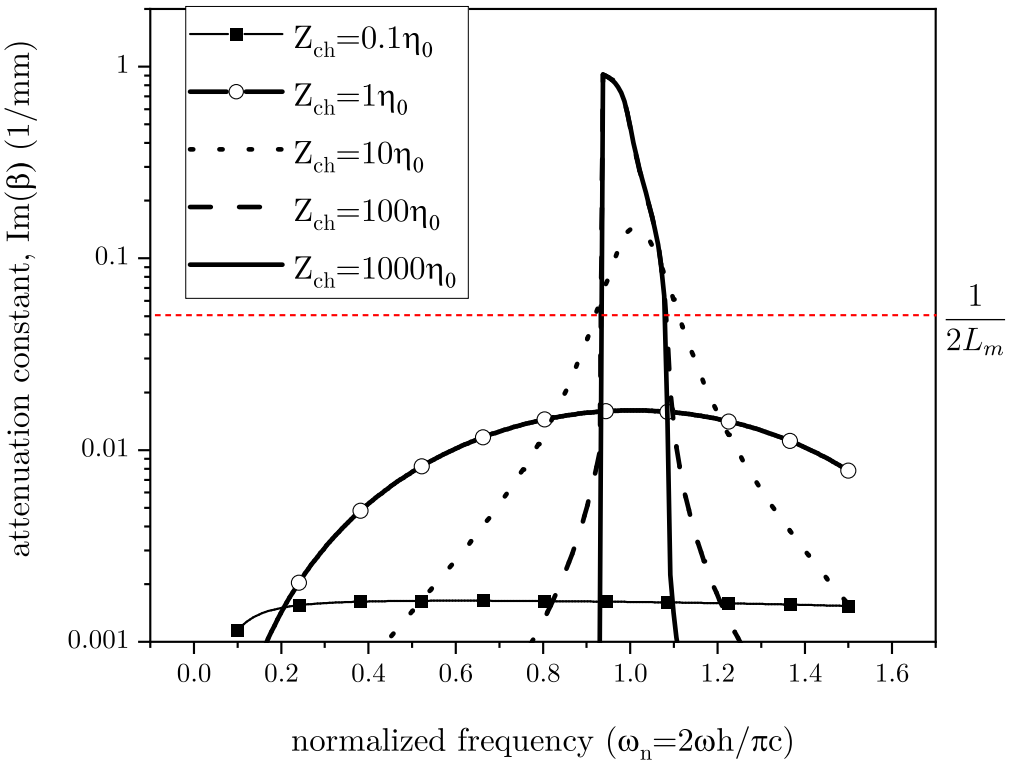

Figure 4.11: Attenuation constant of SSPP waveguide for different values of channel impedance Z_{ch}. The bandgap can be defined by the width of attenuation constant spectrum that goes above $\dfrac{1}{2L_m}$, where L_m is the length of SSPP modulator.

Figure 4.11 is the starting ground from where we can discuss about the maximum speed of modulation, i.e., modulation bandwidth, which corresponds to the spectral gap for which carrier signal attenuation is high enough. Carrier signal is of the form of $\sim exp(i\beta x)$, hence the corresponding carrier power is $\sim exp(2i\beta x)$. We can define spectral gap as the extent of spectrum for which carrier signal power is reduced by a

factor of $exp(-1) \approx 36\%$. Then, between the spectral gap,

$$Im(\beta) \geq \frac{1}{2L_m}$$

where L_m is the length of modulator SSPP waveguide, and $Im(\beta)$ is the attenuation constant. It is evident from Fig. 4.11 that the part of the spectrum with high attenuation constant in SSPP waveguide always spans around the normalized frequency $\omega_n = \frac{2\omega h}{\pi c} = 1$. Also, with the increase of channel impedance Z_{ch}, the maxima of attenuation constant increases, while the spectral width of attenuation constant (i.e., $\sim FWHM$) decreases.

If we choose to design auxiliary SSPP (modulator SSPP) waveguide to have a length of $L_m = 20$ mm, then, we can see from Fig. 4.11 that the spectral gap of the modulator expands from ~ 0.9 to ~ 1.1 of normalized frequency ω_n.

If we choose $h = 8$ mm, then the actual frequency f corresponding to the unity normalized frequency $\omega_n = 1$ is $\frac{c}{4h} = 9.38$ GHz. Therefore the spectral gap would extend from 8.44 GHz to 10.31 GHz, making the spectral gap to be $(10.31 - 8.44)$ GHz ≈ 1.8 GHz. If this spectral gap is optimally merged with the band-edge of the primary SSPP waveguide, then this 1.8 Gbps would the maximum speed of modulation that we can expect for the aforementioned chosen geometry of SSPP modulator.

We can also recommend, from the observation of Fig. 4.11 that, for achieving 1.8 Gbps modulation speed, we have to be able to switch the channel impedance Z_{ch} from $1\eta_0$ to $10\eta_0$ at least at a speed of orders of magnitude faster than the modulation bandwidth, where $\eta_0 = 377\Omega$ for free standing SSPP waveguide. If we consider the effect of substrate, then the corresponding η would be smaller.

The other geometric dimensions of the SSPP modulator corresponding to the choice of $h = 8$ mm would be: period, $d = 10$ mm, groove width $a = 1$ mm, and arm width $g = 3$ mm, which would result in the same profile of attenuation constant as shown in Fig. 4.11. Since $L_m = 20$ mm, the modulator would comprise of two

grooves, each situating 10 mm apart.

There are two possible ways of increasing the speed of modulation with the given groove length $h = 8$ mm. One, we can increase the length of modulator, which will increase the percentage of carrier signal decay for the same attenuation constant. The drawback of this approach is: the increase of modulator length L_m means more grooves has to be included in the modulator waveguide, with bridge on each groove. As each bridge essentially represents the channel of transistor, there will be challenges in synchronizing the switching of greater number of transistors. The second way of increasing the modulation bandwidth is to reduce the arm-width g, which would increase the bandgap of SSPP waveguide, following Eq. 4.21 and 4.23. Reduction of g however, may introduce additional mechanism of slowing down the modulation speed once the resistance R of the metals of waveguide, and therefore the relaxation time constant $\tau = RC$ of the SSPP arm is no longer negligible.

Let us present a demonstration of the effect of increasing the speed of modulation on the signal quality through numerical simulation. If a carrier signal of unity amplitude is chosen with frequency ω_c to coincide with the band-edge of the principal SSPP waveguide, and is modulated by the mechanism of abrupt bridge impedance alternation between the range of $Z_{ch} = [Z_p, Z_s]$, where Z_p stands for the lower limit of impedance meant for passing the carrier signal, and Z_s stands for the upper limit of impedance meant for stopping the carrier signal, then the output $S_{mod}(t)$ of the signal modulator will be,

$$\begin{aligned} S_{mod}(t) &\sim e^{-i\omega_c t}\Pi_T(t)\sum_{m=\infty}^{m=\infty}\delta(\omega-(\omega_c+m\omega_{mod})) \\ &= \sum_{m=-\infty}^{m=\infty} c_m e^{-i(\omega_c+m\omega_{mod})t}\delta(\omega-(\omega_c+m\omega_{mod})) \end{aligned} \tag{4.26}$$

where $\Pi_T(t)$ is a square wave function in time domain with period T, and with

its maximum value as $|T_{zp}(\omega)|$, and the minimum value as $|T_{zs}(\omega)|$. Here $T_{zp}(\omega)$ stands for the transmission spectrum of the composite SSPP waveguide when the bridge impedance $Z_{ch} = Z_p$ and $T_{zs}(\omega)$ stands for the transmission spectrum of the composite SSPP waveguide when the bridge impedance $Z_{ch} = Z_s$. Also, $\omega_m od = \frac{2\pi}{T}$, and m is the indices of various components $c_m$of the fourier series of the square wave function $\Pi_T(t)$.

The second line of Eq. 4.26 is written with the expansion of the square wave $\Pi_T(t)$ in its fourier series. For 50% duty cycle, the $m-th$ component is,

$$c_m = \begin{cases} \frac{1}{2}[|T_{zp}(\omega)| - |T_{zs}(\omega)|]\,\mathrm{sinc}(\frac{m}{2}) & \text{for } m \neq 0 \\ \frac{|T_{zs}(\omega)| + |T_{zp}(\omega)|}{2} & \text{for } m = 0 \end{cases} \tag{4.27}$$

The fourier components with the $+ve$ frequency would add up with the carrier frequency ω_c and blue-shift the frequency. Since ω_c is chosen to coincide with the band-edge of principle SSPP waveguide, further blueshift of this frequency would fall into band-stop zone of the interconnect, and therefore we shall only take into account of those terms with $-ve$ frequency.

After taking into account only the first fourier component of switching function $\Pi_T(t)$, we get the following expression of the modulated signal:

$$\begin{aligned} S_{mod}(t) &\sim c_0 \cos(\omega_c t) + c_{-1} \cos((\omega_c - \omega_{mod})t) \\ &= c_0 \cos(\omega_c t) + c_{-1} \cos(\omega_c t) \cos(\omega_{mod} t) + c_{-1} \sin(\omega_c t) \sin(\omega_{mod} t) \end{aligned} \tag{4.28}$$

It can be seen from the above equation that, if the second fourier component of the modulated signal c_{-1} becomes 0, then $S_{mod}(t)$ will become a mere monotone signal of frequency ω_c, and we cannot retrieve any information out of it. Thus, we can define the critical limit of modulation frequency ($\omega_{mod,c}$) for which the modulation depth $c_{-1} = 0$, which implies, from Eq. 4.27 that, at the critical modulation frequency,

$|T_{zp}(\omega = \omega_c - \omega_{mod,c})| = |T_{zs}(\omega = \omega_c - \omega_{mod,c})|$. For retrievable information transfer, ω_{mod} must be smaller than $\omega_{mod,c}$.

For instance, for the specific SSPP modulator with the transmission property depicted in Fig. 4.10, if the carrier frequency ω_c is chosen to coincide with the band-edge of the principle SSPP waveguide $\sim$ 9.5 GHz, then the maximum allowable modulation frequency $\omega_{mod} < \omega_{mod,c}$ can be found from the graph of second fourier component c_{-1} vs ω_{mod}, as shown in Fig. 4.12.

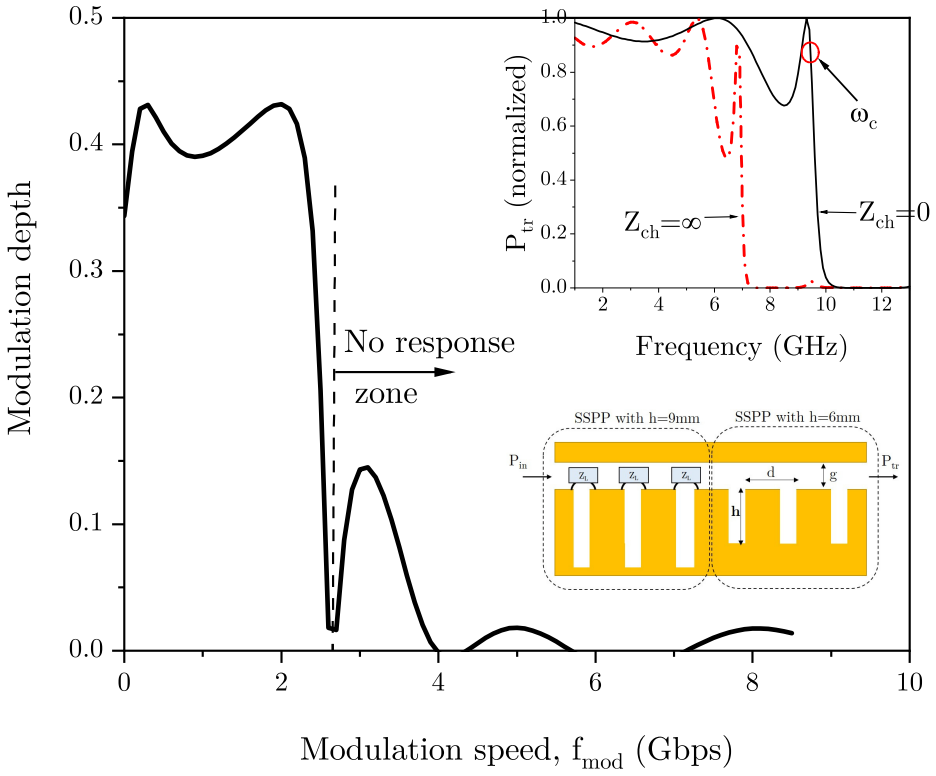

Figure 4.12: Modulation depth of the output of the SSPP modulator with the increase of modulation frequency ω_{mod}. The inset shows the corresponding geometry of SSPP modulator and also the transmission spectrum when the bridge impedance Z_{ch} swings between 0 and ∞.

Figure 4.12 shows how much modulation frequency is allowable for the SSPP modulator with the following geometry: groove length of primary SSPP waveguide, h = 6 mm, that of auxiliary/modulator SSPP waveguide, h_m = 9 mm, d = 6 mm

and $g = 3$ mm, and the auxiliary SSPP modulator consists of 3 grooves. The inset of Fig. 4.12 shows the corresponding geometry of the modulator, along with the transmission spectrum of the modulator for two extreme value of $Z_{ch} = [0, \infty]$. As we see, for this particular case, the carrier signal stops responding to the modulation mechanism once we go past the modulation speed of ~ 2.5 Gbps.

4.10 Summary of this chapter

In this chapter, I discussed how to harness the resonating property of spoof plasmon waveguide in order to make high-speed modulator for spoof plasmonic signal. I demonstrated that the length of the spoof plasmonic modulator can be as short as that containing a single unit cell, and described how we can design a spoof plasmon waveguide with high Q-factor resonant tunneling mode by cascading grooves of different lengths. Then I proposed an idea of dynamically altering the effective resonant frequency of the waveguide by attaching a transistor across each of the grooves of the modulator; so that the transmission property of the waveguide can be drastically changed upon switching the transistor ON and OFF. The parameters of the modulating waveguide that can be tailored in order to increase the modulation speed and depth of modulation are also discussed with analytical expressions.

CHAPTER V

Preserving Signal Integrity in SSPP channels

5.1 Introduction

The issue of interconnect designing has so far been dealt with intelligent designing such as multiple layer interconnect, cross-bar data-bus etc. (*Park et al.* (2008)), but we are gradually running out of design space, and the circumstances calls for finding a new type of interconnect obeying different physics. The present thesis proposes a technique of information transfer over short distance, spanning $0.1 - 10$ cm by spoof surface plasmon polariton (SSPP), an entirely different class of quasiparticle accommodated by metallic surface with deliberate design pattern (*Erementchouk et al.* (2016a)). Spoof plasmon interconnect is a novel communication system which leverages the unique electromagnetic properties of metasurface for high speed data transfer while maintaining high signal integrity by suppressing cross-talk among adjacent wires. Unlike conventional interconnects which incur aggravated signal fidelity at elevated frequencies owing to cross-talk, spoof plasmon channel demonstrates quite reverse trend: the cross-talk is suppressed further at high frequency end of its band—allowing the possibility of faster data transfer with signal integrity.

5.2 Background studies: Process variation in interconnects

The effect of process variation in deep submicron interconnect on-chip is a well studied field. However, the standard interconnects usually have a very simple and plain geometry: such as that of an electrical interconnect with rectangular cross-section, and therefore the nominal variation of process parameters resulting in the variation of the geometry of the interconnect does not pose a major issue in the electronic conduction mechanism of the standard channels. However, pattern-irregularity in spoof plasmon interconnect may warrant us to take the effect of process-variation more seriously than ever before in order to deal with potential new issues while testing its feasibility. To elaborate, the unique ability of the metasurface to carry information with high fidelity is attributed to its carefully crafted geometric pattern (*Huidobro et al.* (2020)); and hence it might be critical to brood over about the possibility of inadvertent pattern irregularity in metasurface due to fabrication imperfection, and about the effect of these undesired irregularity on signal integrity. To elaborate, there are finite probabilities that the patterns will not be identical to the design due to variation in fabrication process such as mask misalignment, diffraction in lithography, non-uniform metal deposition and polishing etc. As the electromagnetic properties of a metasurface is governed by the geometry, the inadvertent process variation may lead to aberration of the data transmission behavior of the channel.

It might be argued that, the state-of-the-art fabrication technologies have become matured enough to provide sub-nanometer scale resolution (*Ryu Cho et al.* (2017)), and therefore the study of the impact of process variation in SSPP structures with micron scale feature sizes is now little more than an academic interest. While the argument is valid for a planar or horizontal interconnect structure, an act of metal patterning on a vertical direction, for instance if SSPP interconnect has to replace conventional through-silicon-vias (TSV) in a three dimensional large scale integration (3D-LSI) system (*Motoyoshi* (2009)), would definitely confront far more challenges,

and could easily be resulted into significant pattern variation.

5.3 Author's contribution in the field of spoof plasmon signal restoration

In the present chapter, I delved into some practical fabrication non-idealities that can impact the performance of spoof plasmon channel. I investigated the frequency responses of an ideal SSPP channel with regular pattern, and analyze how these responses get affected when the metal patterning becomes irregular owing to fabrication imperfection. I then elaborated the consequences of the geometric pattern irregularity of SSPP on the integrity of the digital signal transmitted through the channel; and explain how one can build compensating analog circuit in order to recuperate the loss in signal quality in real-time.

5.4 Frequency response of SSPP channel

5.4.1 SSPP channel with ideal pattern

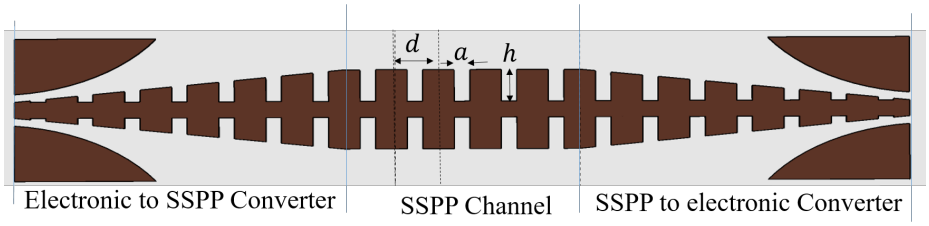

Figure 5.1: Geometric features of SSPP channel, including the electronic-SSPP converter on both end

In order to make point to point electrical signal transmission via SSPP interconnect, we designed an appropriate adapter in the transmitting end so as to convert the transverse electromagnetic mode into a surface bound mode. The adapter comprises of a Vivaldi antenna, and the length of the grooves of the adapter has been gradually

increased so as to match the TEM mode with SSPP mode over a broadband. In the receiving side, we employed the mirrored structure of the transmitting adapter. The geometry of an isolated SSPP interconnect with converter is shown in Fig. 5.1.

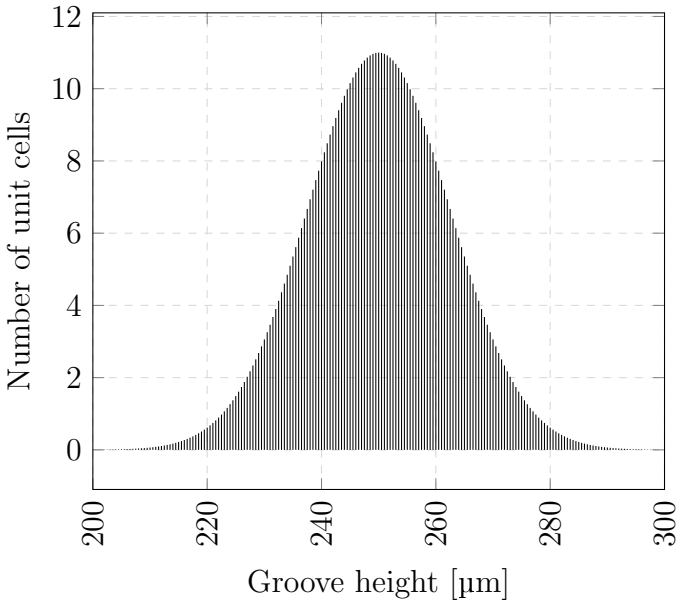

Figure 5.2: Probability distribution of groove length in a 5 cm SSPP channel, where the length varies around the designed mean value by 3%

SSPP metasurface is characterized by few features including length (h) and width (a) of groove, thickness (t) of metal film, refractive index (n_s) of substrate. Among them, the most critical parameter happens to be h, since it determines the resonant frequency (ω_r). Near resonance, an SSPP bandgap arises, the detuning of the band-edge frequency (ω_B) from ω_r is proportional to the coupling between the modes in resonating groove and that in free space. The fundamental band of SSPP spans from zero frequency up to ω_B. The field confinement gradually increases as one proceeds along the band to the highest frequency ω_B. Because of the nominal field confinement in the lower part of the band, we have to forsake some lower fraction of the band to avoid cross-talk among neighboring channels. It has been shown in **?** that, given the condition of cross-talk remaining below -3 dB at any transmitted frequency

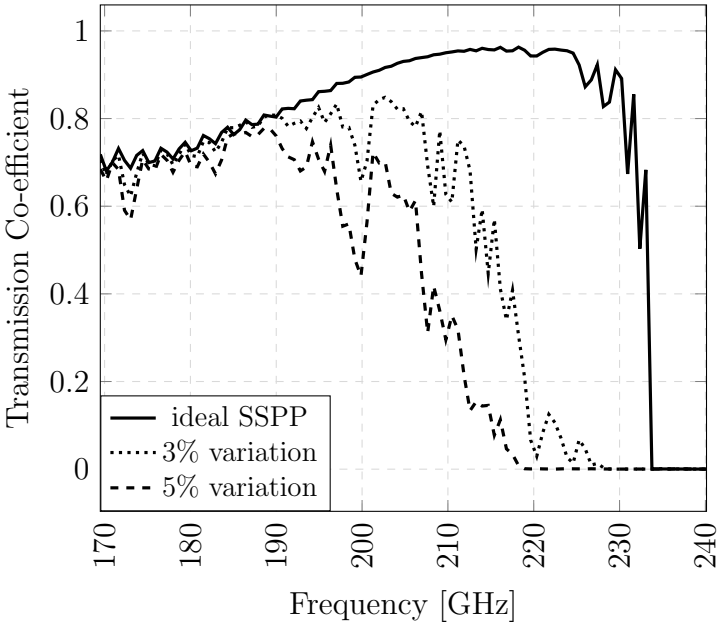

(a) Magnitude response

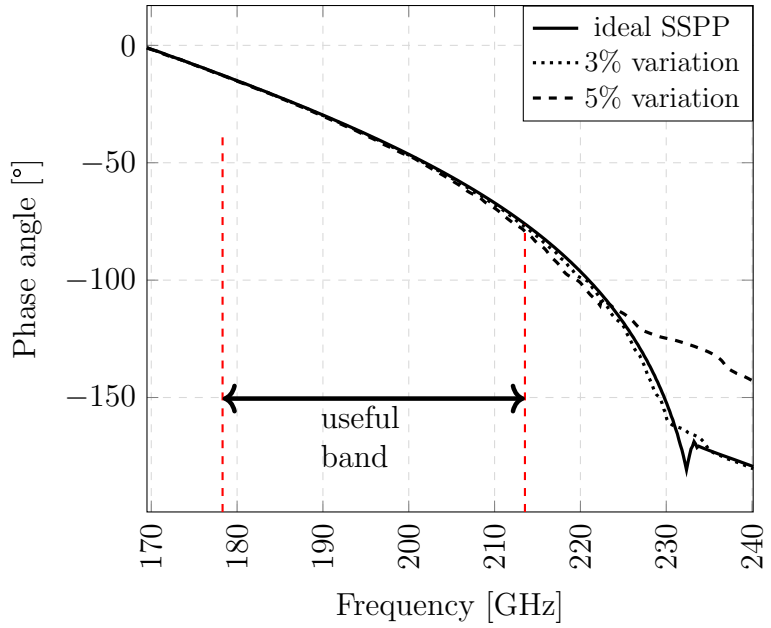

(b) Phase response

Figure 5.3: (a) Magnitude and (b) phase response of ideal SSPP, SSPP with 3% and 5% co-efficient of variance of the irregular metasurface pattern. The relatively linear segment of the band that can be utilized for data transfer is also shown with double arrow sign.

component in a parallel data-bus, the maximum bandwidth density corresponds to the utilization of upper one-third ($\frac{1}{3}$) fraction of the full fundamental band of SSPP for data transfer.

In the present study, we designed the groove length (h) such that the resonant frequency (ω_r) appears to be close to 300 GHz frequency. The ratio a/d is taken to be 0.3. For a given period d in the metasurface, an increase of $\frac{a}{d}$, at the cost of nominal decrease in bandwidth, benefits us in two ways: it increases field confinement for a broader range of frequencies on the fundamental band which helps combat cross-talk, and it also reduces ohmic loss in the metal, as the loss is proportional to a/l_s, where l_s is the skin depth of the metal at the operating frequency.

5.4.2 SSPP with pattern irregularity

We assumed that the process variation would result in a Gaussian distribution of the feature size of SSPP metasurface, as such sorts of distributions are also reported in the features of standard VLSI interconnects *Verma et al.* (2009). If needed, our method could be easily adapted for other types of statistical, such as Poisson distribution analysis by redefining the rate parameters. In our model, the number of unit cells having groove length h is defined as follows:

$$N(h) = \frac{N_T}{\sigma_h\sqrt{2\pi}} exp\Big(- \frac{(h - h_m)^2}{2\sigma_h^2}\Big) \tag{5.1}$$

Where N_T is the total number of unit cells in an SSPP channel, h_m is the mean value of groove length in the structure, and $\sigma_h^2 = 1/N_T \sum_i (h_i - h_m)^2$ is the variance of the distribution for h, which depends on the particular fabrication process. Since we are dealing with discrete numbers, we ensured that the length of grooves of all the unit cells in a given structure is accounted for within the range of $\pm 3\sigma_h$. As per the suggestion of **?**, , the signal propagation length through an SSPP channel

with groove length of 250 μm can be up to 5 cm. We have taken the period of the structure to be 375 μm, and the groove width is taken as 125 μm. The rationale of choosing these value of h parameter follows from the fact that the corresponding resonant frequency of the unit cell is 300 GHz, and this is the spectral ballpark where state-of-the-art sub-terahertz CMOS oscillator can generate carrier frequency efficiently (*Tousi et al.* (2012)). The value of period d is chosen in a way so that we meet the condition ($2h > d$) of yielding high field confinement zone of SSPP (*Erementchouk et al.* (2016a)), but at the same time evade being into too deep SSPP region where the advantage of strong field confinement is smeared by the drawback of dispersion induced pulse distortion and heightened ohmic loss. With the chosen value of period d in a 5 cm long interconnect, there will be more than 120 unit cells in the channel, which is a reasonably large number to test the impact of inhomogeneity in their geometric shape.

In order to study the impact of geometric shape variation of SSPP structure on the information capacity of the channel, we took different values of σ_h. For instance, for a 3% variation, the length of the groove h among all the unit cells in the 5 cm long channel will vary within the range of (250$\pm$7.5) μm around the designed length of 250 μm, which corresponds to $3\sigma_h = 7.5$ μm. Figure 5.2 shows the gaussian distribution of the groove lengths, centered around the mean value of 250 μm, that we have taken to simulate the behavior of SSPP channel with pattern irregularity.

5.5 Performance Loss for Structural Imperfections

5.5.1 Bandwidth degradations

Because of random variation of the length of groove in SSPP structure, the transmission characteristics over the frequency range is affected. Figure 5.3a and 5.3b show the magnitude and phase of transmission coefficient, respectively for different

degree of co-efficient of variance of SSPP pattern irregularity. We defined the bandwidth of a perfect SSPP channel by the difference between the upper (f_U) and lower cut-off frequency (f_L). The upper cut-off frequency is marked by the drop of power gain from the maxima by -3 dB, while the lower cut-off frequency is marked by the frequency below which transmission co-efficient drops below 0.7. We observed that the upper cut-off frequency is quite sensitive to the variation of groove length, and shows red-shift with the increase of σ_h. On the contrary, the lower cut-off frequency is relatively less sensitive to the variation of groove length. In addition, with the increase of statistical variation of groove length, the roll-off of the transmission power with frequencies around the upper cut-off frequencies reduces.

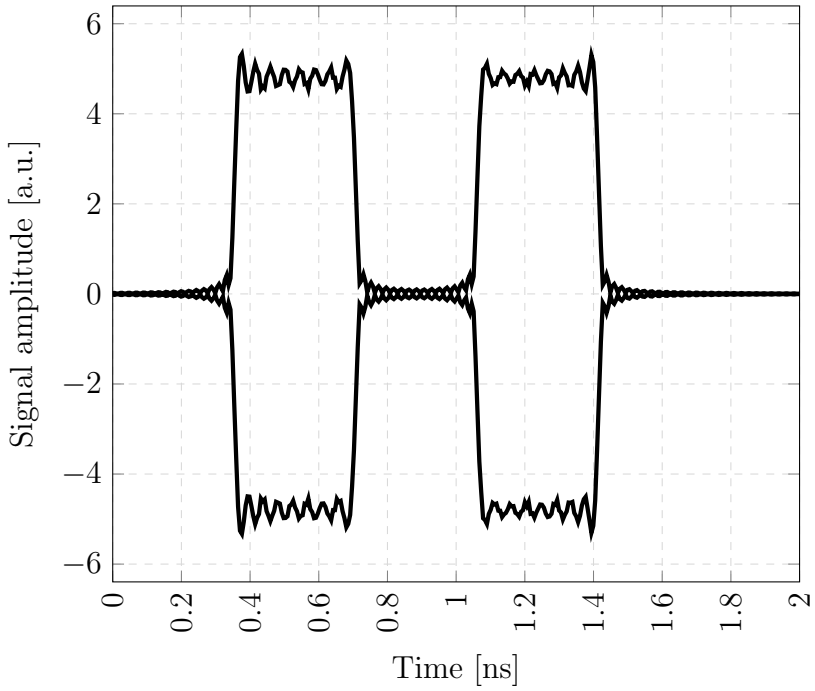

Figure 5.4: Sub-terahertz carrier frequency modulated random digital data, after being filtered is provided as input to the SSPP interconnect

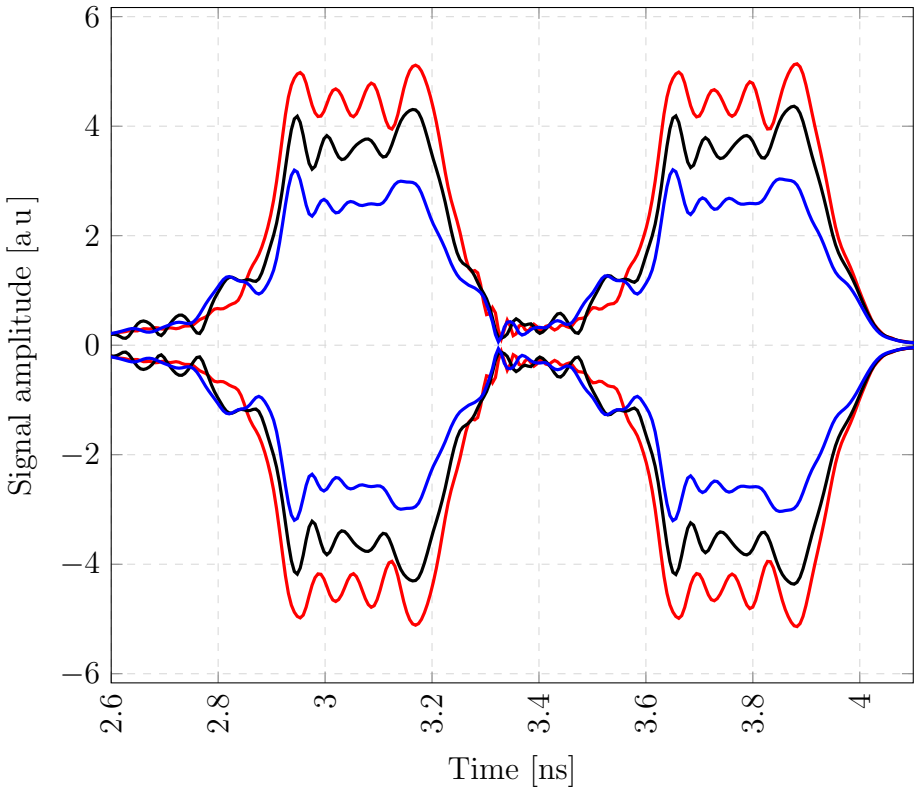

Figure 5.5: Received signal after transmitting through ideal SSPP (red line), SSPP with 3% variation (black line) and SSPP with 5% variation (blue line), Besides signal attenuation, the signal also suffers from shape distortion

5.5.2 Loss of signal integrity

In order to evaluate the integrity of transmitted signal, we must carefully consider both the magnitude and phase responses of the SSPP structure. In absence of any geometric variation, the magnitude of transmission coefficient shows a value of ≥ 0.8 from 180 GHz to 230 GHz. However, near 230 GHz, we observed a sudden spike in the gain magnitude. This spike is likely to be resulted from the Fano-antiresonance. At the same time, the phase response also shows a sudden change around fano-antiresonance near 230 GHz. As the strong nonlinearity in phase response can result in significant distortion of pulse, a fraction of the bandwidth in the upper extreme of SSPP spectrum has to be sacrificed for the sake of maintaining signal integrity. Therefore, while transmitting data through SSPP channel, we restrict the bandwidth

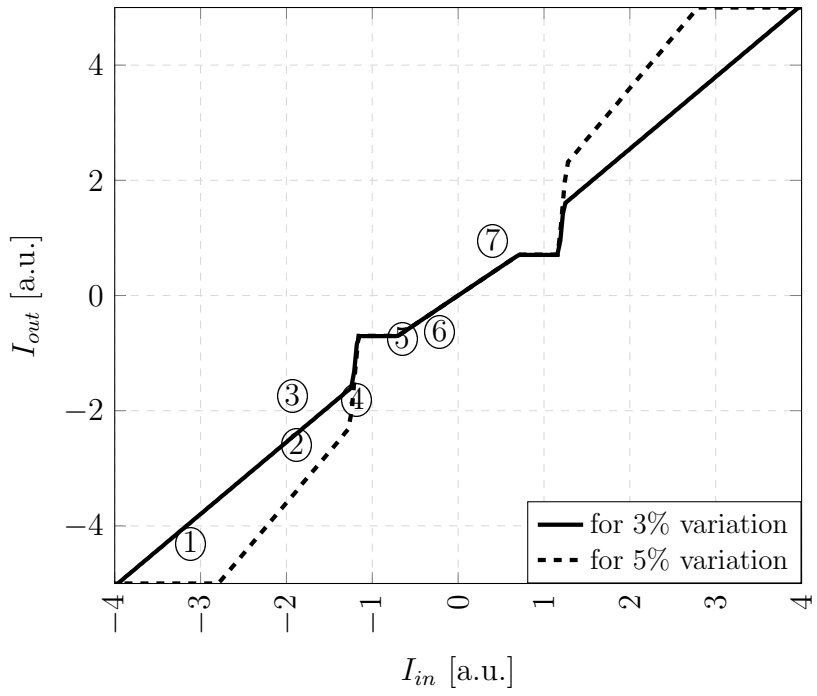

Figure 5.6: Transfer function of nonlinear compensation circuit for different degrees of structural irregularities in SSPP channel. The different linear pieces on a particular compensation function are designated with numbers from ① to ⑦

of the data pulse to be within $(225 - 180)$ GHz= 45 GHz, the spectrum over which the gain remains roughly constant, and phase remains roughly linear, as indicated in Fig. 5.3b. We transmitted the double side-band data, hence the carrier frequency is selected to be the mid-frequency $f_{carrier} = (225 + 180)/2$ GHz ≈ 203 GHz of the available transmission window of SSPP channel. We sampled random binary data at a sampling rate of F_s. Since a rectangular function in time domain spreads up to infinite frequency in spectral domain, we truncated the spectrum of the pulse by a low-pass filter with a cut-off frequency at $(225 - 203)$ GHz= 22 GHz. F_s is chosen in a way so that the main lobe in addition to eight side-lobes on each side of the main lobe of the spectrum of a rectangular pulse can fit within the transmission window of SSPP.

$8F_s = 22GHz$

Theoretically it could have been possible to make data transfer rate F_s equal to

half of the available bandwidth in the channel. However, in a real set-up, doing so could have resulted in worse bit-error-rate in the receiving side due to the presence of noise and the jitter in signal recovery timing.

Figure 5.4 depicts the input signal, taken as '1010' bit pattern, sampled at a frequency of $F_s = 2.75$ GHz and modulated by frequency $f_{carrier} = 203$ GHz, that is fed to the SSPP channel after appropriate filtering and modulation. Depending on the degree of of patterning irregularity in SSPP metasurface, the fidelity of the signal emerging from the other end of the channel aggravates. Figure 5.5 shows the time domain '1010' signals that emerge at the receiving side of SSPP channel, and compares the signal integrity for different extent of pattern imperfection in the channel. The comparison vividly shows that, with the pattern irregularity getting worse, the amplitude of the signal deteriorates. However, if it were only the amplitude that would aggravate with pattern irregularity, we could have recuperated the signal by simply deploying appropriate amplifier. Unfortunately, due to the apparent non-uniformity in the frequency response of the imperfect SSPP channel over the chosen 45 GHz bandwidth, the signal also undergoes pulse-shape distortion, shown by red mark in Fig. 5.5, which complicates the design process of the compensation circuit for regaining signal quality.

5.6 Mitigation of Performance degradation

5.6.1 Mathematical Functions to Compensate for Signal Loss

We analyzed what should be the mathematical function of amplitude response of the compensation circuits so that they can restore the distorted signal to its original shape. In order to do so, we have taken the envelop of a modulated signal of a '...000101000..' data stream. This particular bit-pattern is chosen since it represents the most critical transition of bits, and hence is expected to undergo the most severe

effect of dispersion and bandwidth loss. The chosen bit stream is filtered and supplied to the input of two different kinds of SSPP channels: one whose geometry is periodic, and one whose geometry is not. Thus we obtained a pair of envelop function of the output data streams as a function of time, and performed appropriate signal processing in order to express the output signal amplitude of imperfectly shaped SSPP channel (with variance in groove length) as a function of that of perfect SSPP channel. The resultant transfer function is then smoothened in order to approximate it with a piece-wise linear function. This is the function that must have to be the amplitude transfer characteristics of the nonlinear compensation circuit in order to recuperate the signal from distortion incurred from the irregularity in the metasurface channel. Figure 5.6 shows the approximated transfer function of the compensating circuit. Different linear segments of the transfer curve is designated with encircled numbers from ① to ⑦ for the ease of subsequent referencing.

Readers should note that, in actual circuit implementation, the transfer curve depicted in Fig. 5.6 should retain the same shape over the entire bandwidth of data around the carrier frequency. Ensuring the wide-bandwidth amplitude response of the compensating circuit around the carrier frequency is a challenging task, and merits a separate manuscript on its own. In the present work, we shall keep us limited to the analysis of DC characteristics only of the compensating circuit.

5.6.2 Nonlinear Circuit Design for Real-time Compensations

There can be multiple ways of implementing a non-linear circuit with the desired amplitude response function. I have chosen the technique of 'summation of current' in a circuit node in order to generate the particular non-linear response, since addition of current can be as simple as joining wires to a common output node. The basic building blocks of the designed circuit are current mirrors (CM). The CM blocks are supplied with two bias currents, I_1 and I_2. One pair of the FET have a width ratio

of $\frac{1}{\alpha}$. The I/O characteristics of each of the current mirror blocks is a straight line with a slope α, which is clipped at two different co-ordinates: the bottom co-ordinate corresponds to $C_1 \equiv (I_1, 0)$, the top one to $C_2 \equiv \left(I_1 + \frac{I_2}{1+\alpha}, \frac{I_2\alpha}{1+\alpha}\right)$. Transition of output current from C_1 to C_2 follows a straight line with slope = α. Figure 5.7 shows the basic CM block and its amplitude transfer function. It has been shown in *Wilamowski et al.* (2000) that the above described CM blocks can be combined to generate arbitrary non-linear transfer function.

For concise representation of the final design of the full compensation circuit, I shall represent the CM block as a black box, characterized by the ratios of transistors' widths. In order to acquire the desired transfer characteristics (shown in Fig. 5.6) of the compensating circuit, I added the output node of five such CM blocks, where the ratios of transistors' widths of each of the CM blocks have been chosen carefully so as to generate the full transfer curve, as shown in Fig. 5.8. As the individual CM blocks cannot provide bidirectional current, we have to also add an offset current source at the input terminal of the compensation circuit so as to shift the entire transfer curve either to the right or to the left of x-axis (i.e., to a quadrant of the cartesian co-ordinate system where input current is unidirectional). The output of the compensation circuit will be fed to the next SSPP channel through a transformer so as to truncate the DC component from the output signal.

5.6.3 Dynamic Tunablity of Compensation Circuit

Despite a standard fabrication process is characterized by minimum resolution features and expectation value of errors, it is unlikely that we would have a prior exact knowledge of the degree of variations in a specific sample of SSPP channel. Hence the compensation circuit ought to have the in-situ tunability, as the fine details of the input-output characteristics of the required compensating circuit depends upon the exact co-efficient of variance of geometric pattern of the particular sample interconnect

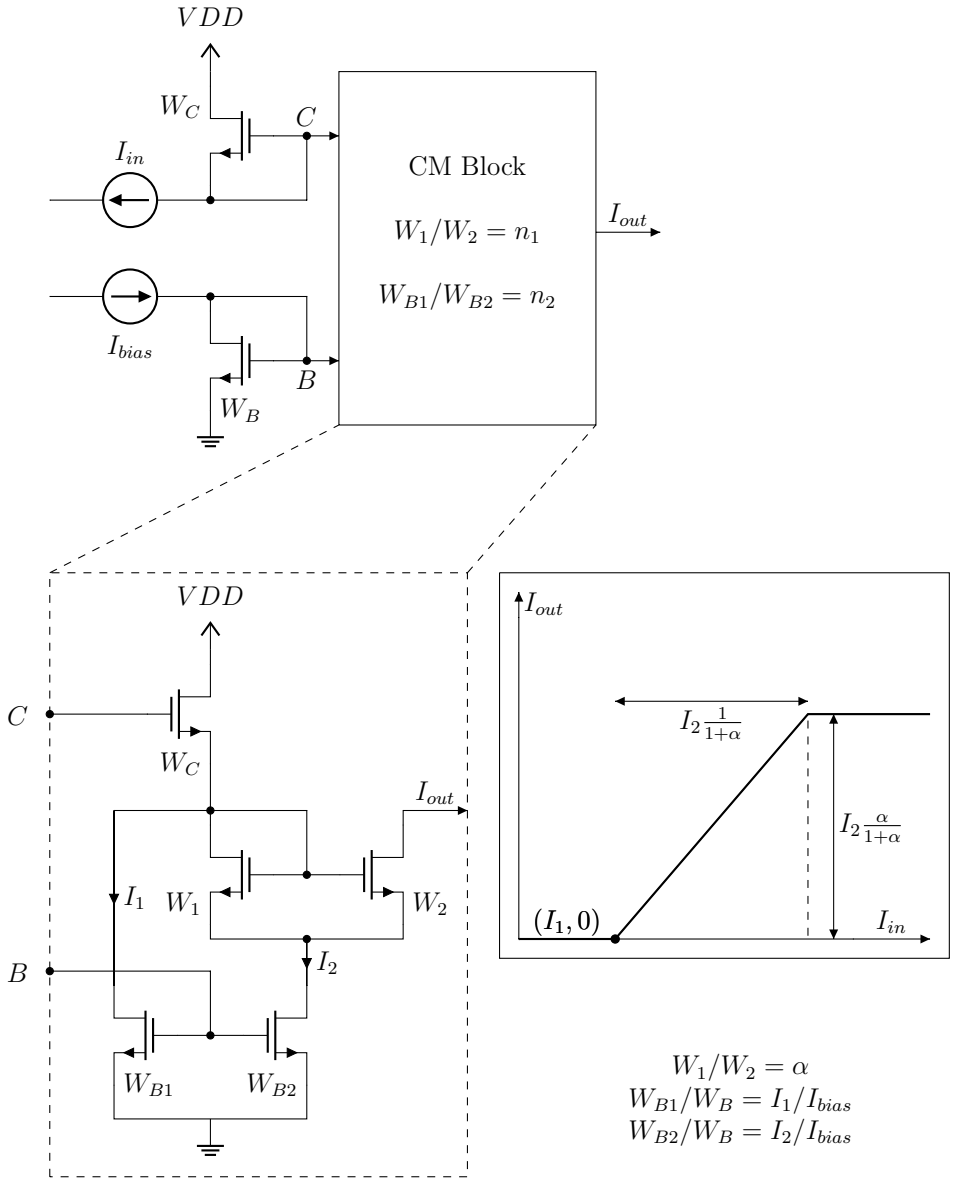

Figure 5.7: Basic current mirror block of the compensation circuit with its piecewise linear amplitude response shown in the inset. Such sort of blocks will be combined to construct the full compensation circuit.

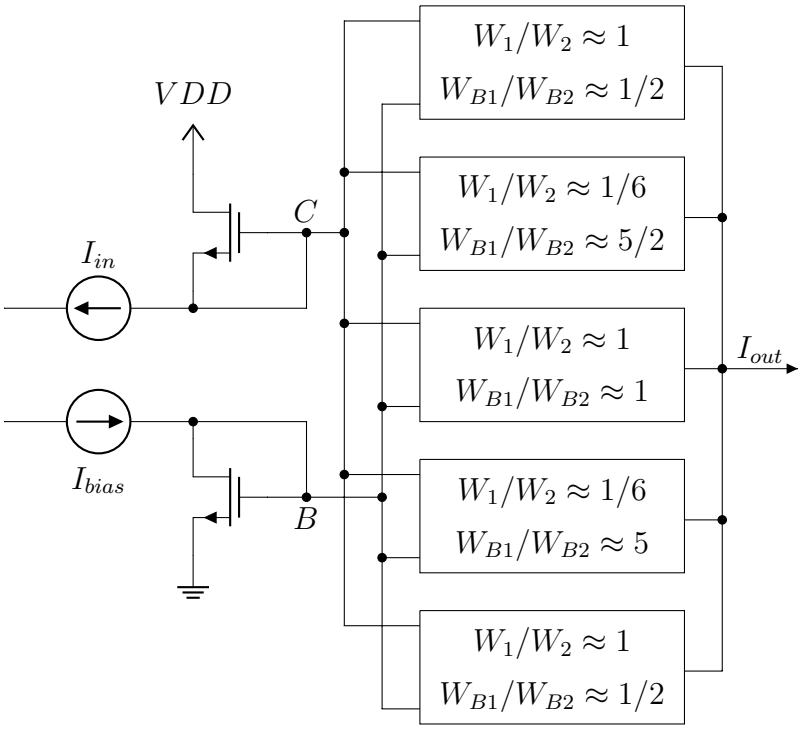

Figure 5.8: Full circuit design for compensation of performance loss of SSPP channel for structural irregularity. The current mirrors are drawn in the form of black boxes, characterized by the ratios of transistor widths for concise representation.

chip.

As suggested by my analysis, regardless of the degree of pattern irregularity, the required input-output amplitude transfer behavior of the compensation circuit remains mostly identical for region ③, ④, ⑤, designated on Fig. 5.6. The parts of the compensation function designated as region ①, ②, ⑥, ⑦ vary with the degree of geometric irregularity in terms of their slopes, where the slopes have to become steeper with increased degree pattern irregularity. The tunability of the compensation circuit can be readily obtained by inclusion of additional FETs parallel to that designated with transistor width W_2 in Fig. 5.7, each of the additional FETs will be controlled by a series connected transistor. Further tunability, if needed, can also be obtained by provision of extra bias current sources.

5.7 Summary of the chapter

With the beginning of the era of 'tyranny of interconnect', the quest for a novel interconnect technology can potentially be satiated by spoof surface plasmon based channel, which gets rid of conventional parasitic effect such as channel capacitance and inductance. In this chapter, I endeavored to analyze the collateral fabrication issues that may emerge with the introduction of the new technology, the ramification of the same in the channel performance, and the methodology for compensation for the degraded performance by proper circuit design. This may constitute an important step towards realization of the novel technology and integrating it with the standard CMOS fabrication process.

CHAPTER VI

Roadmaps for Spoof Plasmon Interconnect Research

6.1 Introduction

The thesis, so far, has endeavored to build a coherent theory for data transfer through the bus of spoof plasmon interconnect for a point to point parallel communication. It started with determining the electromagnetic dispersion relation in a periodically corrugated film of metal residing on a substrate– the most common form of in-plane spoof plasmon interconnect. Later on, based on the developed dispersion relation, this thesis analyzed various performance metrics of spoof plasmon interconnect, such as bandwidth density, propagation loss, bit-error-rate and their trade-off relations. The thesis also showed the proof-of-concept demonstration of the existance of two kinds of electromagnetic modes in spoof plasmon data bus, that are outright different to each other in their characteristics of cross-talk suppression mechanism; as well as it proposed the concept of bandwidth augmentation by harnessing those two kind of modes. The thesis also proposed the technique of signal modulation in spoof plasmonic domain, and analyzed on how to tailor the speed of modulation, and the extinction ratio. Finally the thesis also illustrated how we can recuperate the signal integrity that is otherwise lost in a spoof plasmon interconnect that is degraded of

its ideal geometric pattern for various inadvertent reasons, such as process variation in manufacture, or aging issue.

Yet there is left a number of other things that we have to investigate in order to evaluate the full potential of spoof plasmon interconnect. For instance, this thesis have overlooked the issue of possible impedance mismatch between the channel and the transmitter/ receiver, or mismatch due to channel bending, which may become a severe issue in an actual data transfer system, especially when a very wide spectrum of data is being propagated over the channel.

Among other issues the thesis has not talked about much is the issue of pulse dispersion in an isolated channel– the phenomenon of widening of pulse in time domain due to non-uniform phase velocity of different parts of the spectrum of transmitted data. It also does not discuss much on the possibility of the loss of signal integrity due to non-uniform gain over the spectrum of interest; the non-uniformity in the channel gain can result from fabry-perot ripple in spoof plasmon waveguide.

Because the greatest promise of spoof plasmon interconnect lies in its ability of cross-talk suppression; a significant fraction of the thesis models the interconnect as a lossless line, so that it can extrude the effect of mere cross-talk on our ability of data transmission. However, in real cases, speed of data transmission is also limited by material loss, radiation, channel latency etc. In fact, in chapter 3 of this thesis, it has been shown that, spoof plasmon mode, due to its involvement to resonating grooves, is prone to increased material loss as compared to a TEM mode in a conventional electrical interconnect. Therefore, given all metals are lossy, spoof plasmon interconnect may experience excess loss of signal quality and bandwidth, which may compete, or outweigh the benefit of cross-talk suppression. Therefore, in order to judge the full potential of spoof plasmon interconnect, all the factors that limits signal integrity has to be taken into account, which is of course a daunting task. However, before we move on to the hardware platform, it is imperative to develop a full scale com-

putational model for THz spoof plasmonic network in order to analyze, understand, and determine the best design practice for this novel technology. This thesis should be considered as a precursor to that direction of making full scale electronic-design-automation (EDA) tool to do the performance analysis of spoof plasmon data bus. In the following sections, I discuss some inherent challenges in developing EDA tools for THz SSPP network, and provide a guideline on how the future spoof plasmonic research may overcome those issues.

6.2 Computation of THz SSPP mode: fundamental challenges

Although Maxwell's equations are universal to all electromagnetic phenomena (*Jackson* (1999)), solution methods of those equations apply different approximation techniques in different frequency regimes to overcome the computational overhead associated with solving Maxwell's equations straightforwardly as well as difficulties in analyzing complex systems (*Bondeson et al.* (2005)). For instance, in low frequency circuits, we apply Kirchhoff's Law with lump impedance approximations (*Alexander* (2009)). In microwave circuits, we apply the notion of scalar state variables such as voltage and current to overcome the complexity with calculation of E and H vector fields (*Pozar* (2009)). In optical frequencies, we apply geometric optics with paraxial approximation (*Wolf* (2004); *Saleh and Teich* (2019)). However, the terahertz frequency domain is inherently the most difficult region to analyze because sizes of the components become comparable to the operating wavelength and almost all standard approximations applied to other spectral regions break down in the THz regime. Therefore, we must resort to analysis of the full-wave Maxwell's differential equations that demands exorbitant computation time as well large memory space. The computation efficiency takes further toll once we deal with not only terahertz frequency,

but also a very special form of it—spoof surface plasmon polariton (SSPP), a mode which is radically different from conventional guided modes and free space radiations (*Maradudin* (2011); *Maier* (2007)).

The state-of-the-art computation techniques, such as time-domain analysis (*Rao* (1999)) and frequency-domain analysis (*Notaros* (2008)) divide the entire system into a large number of fine grid points and solve the Maxwell's equations on each grid. Therefore, the degree of analytical complexity increases exponentially when the system becomes larger. Other alternative non-meshing methods such as boundary element analysis have also their own shortcomings in solving structures with fine feature sizes (*Hafner et al.* (1990); *Chew et al.* (2001); *Weile and Michielssen* (1997); *Kaklamani and Anastassiu* (2002)). Therefore, a large network becomes a formidable challenge to solve by existing simulation tools such as MEEP, COMSOL Multiphysics, and HFSS.

6.3 Towards an efficient computation strategy

As this thesis has laid out a mathematical framework yielding a number of closed form solutions for the analysis of the performance of spoof plasmon interconnect, this framework can be leveraged in an intelligent way to significantly reduce the computational complexity in THz surface-wave analysis by circumventing the strategy of full-wave analysis at each grid point in the meshed SSPP structure. Instead, the overall computational space can be divided into a few modular sub-spaces. It can be demonstrated how to employ reduced dimensional electrodynamics on those sub-spaces by leveraging special properties of SSPP (*Joy Soumitra Roy et al.* (2018)). Thus, this thesis can help to build a dedicated computational platform for terahertz spoof plasmon, which can significantly accelerate the computation time for large-scale network.

With the help of the theoretical framework laid by this thesis, one can attempt to

answer fundamental questions regarding information transfer mechanism in a dense SSPP network, then develop an efficient simulation algorithm for the THz surface-wave network, and finally perform experimental validation of the computation model.

6.4 Development of multi-level computation model for THz surface wave network

6.4.1 Simulation algorithm development

By leveraging several key features of THz surface-wave, the simulation speed of an SSPP based network can be improved by orders of magnitude compared to the existing state-of-the-art methodologies. The flow of the algorithm is explicated below.

Analysis of electrodynamics on modular sub-spaces: The space that accommodates SSPP interconnects will be divided into a few modular sub-spaces, where each of the modules will be subjected to different principles of analysis. On the plane of modal confinement, the waveguide essentially demonstrates electrostatic behavior, governed by Poisson's equation, which is more amenable to computation than the underlying full-wave electrodynamics. Additionally, the metallic part of the SSPP structure provides surface currents that further reduce the computational overhead as currents are scalar quantities. Then the remaining space for analysis is the propagation axis where one-dimensional wave optics can be employed, which can be computed fast enough considering the relevant state variables as quasi-scalar.

Analysis of the non-ideal effects:

The thesis has demonstrated that the effect of the presence of non-idealities on SSPP can be independently analyzed and then coupled to the solution of stand-alone channels in order to refine the results. This particular technique may potentially prove more efficient than the conventional many-grid analysis. Conventional methods require higher-order correction-terms associated with non-ideal phenomena such

as metallic loss and lateral waveguide coupling, thereby slowing down the computations. In order to tackle these issues, a novel computational model can be build that will utilize the first-order perturbation theory and the rigorous coupled-wave analysis (RCWA) approach. Therefore, the dedicated computation platform for THz surface-wave is expected to significantly accelerate the computation speed for large scale networks. At the end, after feeding the obtained solutions of state variables of the interconnect system into the full-wave differential equation solver, an iterative convergence analysis can be performed.

Analysis of noise characteristics in SSPP interconnect:

In the regime of low-crosstalk, the main limitation on the Shannon information capacity of a channel originates from signal to noise ratio (SNR) in the channel. A possible way to estimate thermal noise is to determine the equivalent electrical resistance of SSPP channel by calculating the power propagating in the longitudinal direction on a planar SSPP channel and equating the fraction of the power lost in Joule heating process with I^2R loss. For a relatively simpler case of standalone channel, I have theoretically derived the information capacity in terms of effective SSPP resistance and its bandwidth density for a given geometry. The optimization strategy for the geometry of SSPP channels will then yield the maximum information capacity and the corresponding bit-error-rate (BER) of the SSPP network. In an extended modeling framework, we may include the impact of other types of noises, such as flicker noise and shot noises, and noise introduced by timing jitter in the clock, in case of a digital data transmission. The noise analysis will lead to stochastic modeling of THz spoof plasmon network.

6.5 Summary of the chapter

This chapter reiterates the boundary of the discussion of the current thesis, and makes a critic remark on the frontiers where the scope of the thesis can be expanded

further. It particularly prescribes a guideline for the development of full scale electronic design automation (EDA) tools for analyzing the performance of complicated, large size network based on spoof plasmonic communication. The backbone of the simulation engine of such EDA tools can be established from the analytical, closed form expression of various figure-of-merits of data transfer established in this thesis. I believe, this thesis will act as a precursor for our advancement towards next generation high-speed multi-chip communication by electromagnetic metamaterial.

BIBLIOGRAPHY

BIBLIOGRAPHY

Aghadjani, M., M. Erementchouk, and P. Mazumder (2016), Spoof Surface Plasmon Polariton Beam Splitter, *IEEE Transactions on Terahertz Science and Technology*, *6*(6), 832–839, doi:10.1109/TTHZ.2016.2599289.

Akimov, A., A. Mukherjee, C. Yu, D. Chang, A. Zibrov, P. Hemmer, H. Park, and M. Lukin (2007), Generation of single optical plasmons in metallic nanowires coupled to quantum dots, *Nature*, *450*(7168), 402–406.

Alexander, C. K. (2009), *Fundamentals of electric circuits*, McGraw-Hill.

Ambati, M., S. H. Nam, E. Ulin-Avila, D. A. Genov, G. Bartal, and X. Zhang (2008), Observation of Stimulated Emission of Surface Plasmon Polaritons, *Nano Letters*, *8*(11), 3998–4001, doi:10.1021/nl802603r.

Anker, J. N., W. P. Hall, O. Lyandres, N. C. Shah, J. Zhao, and R. P. Van Duyne (2008), Biosensing with plasmonic nanosensors, *Nature Mater.*, *7*(6), 442–453.

Anwar, R. S., H. Ning, and L. Mao (2018), Recent advancements in surface plasmon polaritons-plasmonics in subwavelength structures in microwave and terahertz regimes, *Digital Communications and Networks*, *4*(4), 244–257, doi: 10.1016/j.dcan.2017.08.004.

Astratov, V., D. Whittaker, I. Culshaw, R. Stevenson, M. Skolnick, T. Krauss, and R. De La Rue (1999), Photonic band-structure effects in the reflectivity of periodically patterned waveguides, *Phys. Rev. B*, *60*(24), R16,255.

Barnes, W. L., A. Dereux, and T. W. Ebbesen (2003a), Surface plasmon subwavelength optics, *Nature*, *424*(6950), 824–830.

Barnes, W. L., A. Dereux, and T. W. Ebbesen (2003b), Surface plasmon subwavelength optics, *Nature*, *424*, 824–830, doi:10.1038/nature01937.

Benson, T., A. Anand, A. Akella, and M. Zhang (2010), Understanding data center traffic characteristics, *ACM SIGCOMM Computer Communication Review*, *40*(1), 92–99.

Bondeson, A., T. Rylander, and P. Ingelström (2005), *Computational electromagnetics*, vol. 51, Springer Science & Business Media.

Brar, V. W., M. S. Jang, M. Sherrott, J. J. Lopez, and H. A. Atwater (2013), Highly confined tunable mid-infrared plasmonics in graphene nanoresonators, *Nano letters*, *13*(6), 2541–2547.

Brey, B. B. (2008), *The Intel Microprocessors*, 8th ed., Prentice Hall Press, Upper Saddle River, NJ, USA.

Brillouin, L. (1948), Wave guides for slow waves, *Journal of Applied Physics*, *19*(11), 1023–1041.

Cai, W., and V. M. Shalaev (2010), *Optical Metamaterials*, Springer-Verlag New York.

Casper, B. K., M. Haycock, and R. Mooney (2002), An accurate and efficient analysis method for multi-gb/s chip-to-chip signaling schemes, in *2002 Symposium on VLSI Circuits. Digest of Technical Papers (Cat. No. 02CH37302)*, pp. 54–57, IEEE.

Chamberlain, J. M. (2004), Where optics meets electronics: recent progress in decreasing the terahertz gap, *Philosophical Transactions of the Royal Society of London A: Mathematical, Physical and Engineering Sciences*, *362*(1815), 199–213, doi: 10.1098/rsta.2003.1312.

Chang, W.-S., B. A. Willingham, L. S. Slaughter, B. P. Khanal, L. Vigderman, E. R. Zubarev, and S. Link (2011), Low absorption losses of strongly coupled surface plasmons in nanoparticle assemblies, *Proceedings of the National Academy of Sciences of the United States of America*, *108*(50), 19,879–19,884, doi: 10.1073/pnas.1113563108.

Chen, C. (2016), A new kind of spoof surface plasmon polaritons structure with periodic loading of T-shape grooves, *AIP Advances*, *6*(10), 105,003, doi: 10.1063/1.4964619.

Chew, W. C., E. Michielssen, J. Song, and J.-M. Jin (2001), *Fast and efficient algorithms in computational electromagnetics*, Artech House, Inc.

Cho, H., P. Kapur, and K. C. Saraswat (2004), Power Comparison Between High-Speed Electrical and Optical Interconnects for Interchip Communication, *Journal of Lightwave Technology*, *22*(9), 2021.

Chu, E., and W. W. Hansen (1947), The theory of disk-loaded wave guides, *Journal of Applied Physics*, *18*(11), 996–1008.

Dokania, R. K., and A. B. Apsel (2009), Analysis of Challenges for On-chip Optical Interconnects, in *Proceedings of the 19th ACM Great Lakes Symposium on VLSI*, GLSVLSI '09, pp. 275–280, ACM, New York, NY, USA, doi: 10.1145/1531542.1531607.

Duan, C., B. J. LaMeres, and S. P. Khatri (2010), *On and off-chip crosstalk avoidance in VLSI design*, Springer.

Engheta, N., and R. W. Ziolkowski (2006), *Metamaterials: Physics and Engineering Explorations*, John Wiley & Sons.

Erementchouk, M., S. R. Joy, and P. Mazumder (2016a), Electrodynamics of spoof plasmons in periodically corrugated waveguides, *472*(2195), 20160,616.

Erementchouk, M., S. R. Joy, and P. Mazumder (2016b), Electrodynamics of spoof plasmons in periodically corrugated waveguides, *Proc. R. Soc. A*, *472*(2195), 20160,616, doi:10.1098/rspa.2016.0616.

Essiambre, R.-J., G. Kramer, P. J. Winzer, G. J. Foschini, and B. Goebel (2010), Capacity Limits of Optical Fiber Networks, *Journal of Lightwave Technology*, *28*(4), 662–701.

Fan, S. (2002), Sharp asymmetric line shapes in side-coupled waveguide-cavity systems, *Appl. Phys. Lett.*, *80*(6), 908–910.

Fernandez-Dominguez, A., L. Martin-Moreno, F. Garcia-Vidal, S. R. Andrews, and S. Maier (2008), Spoof surface plasmon polariton modes propagating along periodically corrugated wires, *IEEE Journal of Selected Topics in Quantum Electronics*, *14*(6), 1515–1521.

Gan, X., et al. (2013), High-contrast electrooptic modulation of a photonic crystal nanocavity by electrical gating of graphene, *Nano Lett.*, *13*(2), 691–696.

Gao, X., and T. J. Cui (2015), Spoof surface plasmon polaritons supported by ultrathin corrugated metal strip and their applications, *Nanotechnology Reviews*, *4*(3), 239–258.

Garcia-Vidal, F., L. Martin-Moreno, and J. Pendry (2005a), Surfaces with holes in them: new plasmonic metamaterials, *J. Opt. A: Pure Appl. Opt.*, *7*(2), S97.

Garcia-Vidal, F. J., L. Martín-Moreno, and J. B. Pendry (2005b), Surfaces with holes in them: new plasmonic metamaterials, *Journal of Optics A: Pure and Applied Optics*, *7*(2), S97, doi:10.1088/1464-4258/7/2/013.

Gu, J., et al. (2012), Active control of electromagnetically induced transparency analogue in terahertz metamaterials, *Nature communications*, *3*(1), 1–6.

Gu, Q. J. (2015), THz interconnect: the last centimeter communication, *IEEE Communications Magazine*, *53*(4), 206–215, doi:10.1109/MCOM.2015.7081096.

Hafner, C., C. V. Hafner, C. V. Hafner, and C. V. Hafner (1990), *The generalized multipole technique for computational electromagnetics*, Artech House Boston.

Han, R., and E. Afshari (2015), Filling the terahertz gap with sand: High-power terahertz radiators in silicon, in *2015 IEEE Bipolar/BiCMOS Circuits and Technology Meeting - BCTM*, pp. 172–177, doi:10.1109/BCTM.2015.7340574.

Han, S., Y. Xiong, D. Genov, Z. Liu, G. Bartal, and X. Zhang (2008), Ray optics at a deep-subwavelength scale: a transformation optics approach, *Nano Lett.*, *8*(12), 4243–4247.

Haurylau, M., G. Chen, H. Chen, J. Zhang, N. A. Nelson, D. H. Albonesi, E. G. Friedman, and P. M. Fauchet (2006), On-Chip Optical Interconnect Roadmap: Challenges and Critical Directions, *IEEE Journal of Selected Topics in Quantum Electronics*, *12*(6), 1699–1705, doi:10.1109/JSTQE.2006.880615.

Heller, B., S. Seetharaman, P. Mahadevan, Y. Yiakoumis, P. Sharma, S. Banerjee, and N. McKeown (2010), Elastictree: Saving energy in data center networks., in *Nsdi*, vol. 10, pp. 249–264.

Hibbins, A. P., B. R. Evans, and J. R. Sambles (2005), Experimental verification of designer surface plasmons, *Science*, *308*(5722), 670–672.

Ho, K., C. T. Chan, and C. M. Soukoulis (1990), Existence of a photonic gap in periodic dielectric structures, *Phys. Rev. Lett.*, *65*(25), 3152.

Homola, J. (2003), Present and future of surface plasmon resonance biosensors, *Analytical and Bioanalytical Chemistry*, *377*(3), 528–539, doi:10.1007/s00216-003-2101-0.

Horowitz, M., C.-K. K. Yang, and S. Sidiropoulos (1998), High-speed electrical signaling: Overview and limitations, *IEEE Micro*, *18*(1), 12–24.

Huidobro, P. A., A. I. Fernández-Domínguez, J. B. Pendry, L. Martín-Moreno, and F. J. García-Vidal (2020), Spoof surface plasmon metamaterials, *MRS Bulletin*, *45*(4), 318–318.

Jackson, J. D. (1999), Classical electrodynamics.

Joannopoulos, J. D., P. R. Villeneuve, S. Fan, et al. (1997), Photonic crystals: putting a new twist on light, *Nature*, *386*(6621), 143–149.

Joy, S. R., M. Erementchouk, and P. Mazumder (2017), Spoof surface plasmon resonant tunneling mode with high quality and Purcell factors, *Physical Review B*, *95*(7), 075,435, doi:10.1103/PhysRevB.95.075435.

Joy, S. R., M. Erementchouk, H. Yu, and P. Mazumder (2019), Spoof Plasmon Interconnects—Communications Beyond RC Limit, *IEEE Transactions on Communications*, *67*(1), 599–610, doi:10.1109/TCOMM.2018.2874242.

Joy Soumitra Roy, Yu Hao, and Mazumder Pinaki (2018), Properties of spoof plasmon in thin structures, *Proceedings of the Royal Society A: Mathematical, Physical and Engineering Sciences*, *474*(2220), 20180,205, doi:10.1098/rspa.2018.0205.

Kaina, N., F. Lemoult, M. Fink, and G. Lerosey (2013), Ultra small mode volume defect cavities in spatially ordered and disordered metamaterials, *Appl. Phys. Lett.*, *102*(14), 144,104.

Kaklamani, D. I., and H. T. Anastassiu (2002), Aspects of the method of auxiliary sources (mas) in computational electromagnetics, *IEEE Antennas and Propagation Magazine*, *44*(3), 48–64.

Karkar, A., T. Mak, K.-F. Tong, and A. Yakovlev (2016), A survey of emerging interconnects for on-chip efficient multicast and broadcast in many-cores, *IEEE Circuits and Systems Magazine*, *16*(1), 58–72.

Kats, M. A., D. Woolf, R. Blanchard, N. Yu, and F. Capasso (2011), Spoof plasmon analogue of metal-insulator-metal waveguides, *Optics Express*, *19*(16), 14,860–14,870, doi:10.1364/OE.19.014860.

Keiser, G. (2003), Optical Fiber Communications, in *Wiley Encyclopedia of Telecommunications*, John Wiley & Sons, Inc., doi:10.1002/0471219282.eot158.

Kim, H., Y. Jeong, J. Park, Y. Hong, J. Kim, et al. (2003), Significant reduction of power/ground inductive impedance and simultaneous switching noise by using embedded film capacitor, in *Electrical Performance of Electrical Packaging (IEEE Cat. No. 03TH8710)*, pp. 129–132, IEEE.

Kleine-Ostmann, T., and T. Nagatsuma (2011), A review on terahertz communications research, *Journal of Infrared, Millimeter, and Terahertz Waves*, *32*(2), 143–171.

Lemoult, F., N. Kaina, M. Fink, and G. Lerosey (2013), Wave propagation control at the deep subwavelength scale in metamaterials, *Nature Phys.*, *9*(1), 55–60.

Liang, Y., H. Yu, H. C. Zhang, C. Yang, and T. J. Cui (2015a), On-chip sub-terahertz surface plasmon polariton transmission lines in CMOS, *Scientific Reports*, *5*, 14,853, doi:10.1038/srep14853.

Liang, Y., H. Yu, J. Zhao, W. Yang, and Y. Wang (2015b), An energy efficient and low cross-talk CMOS sub-THz I/O with surface-wave modulator and interconnect, in *2015 IEEE/ACM International Symposium on Low Power Electronics and Design (ISLPED)*, pp. 110–115, doi:10.1109/ISLPED.2015.7273499.

Liang, Y., H. Yu, J. Wen, A. A. A. Apriyana, N. Li, Y. Luo, and L. Sun (2016), On-chip sub-terahertz surface plasmon polariton transmission lines with mode converter in CMOS, *Scientific Reports*, *6*, 30,063, doi:10.1038/srep30063.

Liao, Z., Y. Luo, A. I. Fernández-Domínguez, X. Shen, S. A. Maier, and T. J. Cui (2015), High-order localized spoof surface plasmon resonances and experimental verifications, *Sci. Rep.*, *5*, 9590.

Lim, A. E. J., J. Song, Q. Fang, C. Li, X. Tu, N. Duan, K. K. Chen, R. P. C. Tern, and T. Y. Liow (2014), Review of Silicon Photonics Foundry Efforts, *IEEE Journal of Selected Topics in Quantum Electronics*, *20*(4), 405–416, doi:10.1109/JSTQE.2013.2293274.

Lin, X.-S., and X.-G. Huang (2008), Tooth-shaped plasmonic waveguide filters with nanometeric sizes, *Opt. Lett.*, *33*(23), 2874–2876.

Lindell, I. V., K. I. Nikoskinen, and A. Viljanen (1997), Electrostatic image method for the anisotropic half space, *IEE Proceedings - Science, Measurement and Technology*, *144*(4), 156–162, doi:10.1049/ip-smt:19971317.

Liu, J., T. Wang, and F. Nie (2017a), Narrow band resonance in the UV light region of a plasmonic nanotextured surface used as a refractive index sensor, *RSC Advances*, *7*(57), 35,957–35,961, doi:10.1039/C7RA01642E.

Liu, L., C. Yang, J. Yang, H. Xiang, and D. Han (2017b), Spoof surface plasmon polaritons on ultrathin metal strips: from rectangular grooves to split-ring structures, *JOSA B*, *34*(6), 1130–1134, doi:10.1364/JOSAB.34.001130.

Liu, X., Y. Feng, B. Zhu, J. Zhao, and T. Jiang (2013), High-order modes of spoof surface plasmonic wave transmission on thin metal film structure, *Optics Express*, *21*(25), 31,155–31,165, doi:10.1364/OE.21.031155.

Lu, Y.-J., et al. (2012), Plasmonic nanolaser using epitaxially grown silver film, *Science*, *337*(6093), 450–453.

Luo, S., J. Zhao, D. Zuo, and X. Wang (2016), Perfect narrow band absorber for sensing applications, *Optics Express*, *24*(9), 9288–9294, doi:10.1364/OE.24.009288.

Ma, H. F., X. Shen, Q. Cheng, W. X. Jiang, and T. J. Cui (2014), Broadband and high-efficiency conversion from guided waves to spoof surface plasmon polaritons, *Laser & Photonics Reviews*, *8*(1), 146–151, doi:10.1002/lpor.201300118.

Maier, S. A. (2007), *Plasmonics: fundamentals and applications*, Springer Science & Business Media.

Maier, S. A., S. R. Andrews, L. Martin-Moreno, and F. Garcia-Vidal (2006a), Terahertz surface plasmon-polariton propagation and focusing on periodically corrugated metal wires, *Phys. Rev. Lett.*, *97*(17), 176,805.

Maier, S. A., S. R. Andrews, L. Martín-Moreno, and F. J. García-Vidal (2006b), Terahertz Surface Plasmon-Polariton Propagation and Focusing on Periodically Corrugated Metal Wires, *Physical Review Letters*, *97*(17), 176,805, doi:10.1103/PhysRevLett.97.176805.

Maradudin, A. A. (2011), *Structured surfaces as optical metamaterials*, Cambridge University Press.

Markov, P., J. G. Valentine, and S. M. Weiss (2012), Fiber-to-chip coupler designed using an optical transformation, *Optics Express*, *20*(13), 14,705–14,713, doi:10.1364/OE.20.014705.

Martin-Cano, D., M. L. Nesterov, A. I. Fernandez-Dominguez, F. J. Garcia-Vidal, L. Martin-Moreno, and E. Moreno (2010), plasmons for subwavelength terahertz circuitry, *Optics Express*, *18*(2), 754–764, doi:10.1364/OE.18.000754.

Meindl, J. D. (2003), Beyond Moore's Law: the interconnect era, *Computing in Science Engineering*, *5*(1), 20–24, doi:10.1109/MCISE.2003.1166548.

Michel, J., and L. C. Kimerling (2007), Electronics and photonics: convergence on a silicon platform, in *33rd European Conference and Exhibition of Optical Communication*, pp. 1–2, doi:10.1049/ic:20070261.

Miller, D. A. B. (2010), Optical interconnects to electronic chips, *Applied Optics*, *49*(25), F59–F70, doi:10.1364/AO.49.000F59.

Miller, D. A. B. (2017), Attojoule Optoelectronics for Low-Energy Information Processing and Communications, *Journal of Lightwave Technology*, *35*(3), 346–396, doi:10.1109/JLT.2017.2647779.

Minkov, M., and V. Savona (2014), Automated optimization of photonic crystal slab cavities, *Sci. Rep.*, *4*, 5124.

Motoyoshi, M. (2009), Through-silicon via (tsv), *Proceedings of the IEEE*, *97*(1), 43–48.

Mui, M. L., K. Banerjee, and A. Mehrotra (2004), A global interconnect optimization scheme for nanometer scale vlsi with implications for latency, bandwidth, and power dissipation, *IEEE Transactions on Electron Devices*, *51*(2), 195–203.

Multiphysics, C. (), Comsol multiphysics reference manual, version 5.2a, *www.comsol.com*.

Mulvaney, P. (1996), Surface Plasmon Spectroscopy of Nanosized Metal Particles, *Langmuir*, *12*(3), 788–800, doi:10.1021/la9502711.

Noda, S., K. Tomoda, N. Yamamoto, and A. Chutinan (2000), Full three-dimensional photonic bandgap crystals at near-infrared wavelengths, *Science*, *289*(5479), 604–606.

Notaros, B. M. (2008), Higher order frequency-domain computational electromagnetics, *IEEE Transactions on Antennas and Propagation*, *56*(8), 2251–2276.

Note, A. A. (2003), Simultaneous switching noise and signal integrity, *Actel Corporation, Jul*.

Owens, J. D., W. J. Dally, R. Ho, D. Jayasimha, S. W. Keckler, and L.-S. Peh (2007), Research challenges for on-chip interconnection networks, *IEEE micro*, *27*(5), 96–108.

Park, D., S. Eachempati, R. Das, A. K. Mishra, Y. Xie, N. Vijaykrishnan, and C. R. Das (2008), Mira: A multi-layered on-chip interconnect router architecture, in *2008 International Symposium on Computer Architecture*, pp. 251–261, IEEE.

Parker, G. (1991), What is the capacitance of parallel plates?, *Computers in Physics*, *5*(5), 534–540.

Parker, G. W. (2002), Electric field outside a parallel plate capacitor, *American Journal of Physics*, *70*(5), 502–507, doi:10.1119/1.1463738.

Pendry, J., L. Martin-Moreno, and F. Garcia-Vidal (2004a), Mimicking surface plasmons with structured surfaces, *Science*, *305*(5685), 847–848.

Pendry, J. B., L. Martín-Moreno, and F. J. Garcia-Vidal (2004b), Mimicking surface plasmons with structured surfaces, *Science (New York, N.Y.)*, *305*(5685), 847–848, doi:10.1126/science.1098999.

Pillai, S., K. R. Catchpole, T. Trupke, and M. A. Green (2007), Surface plasmon enhanced silicon solar cells, *Journal of Applied Physics*, *101*(9), 093,105, doi:10.1063/1.2734885.

Pors, A., E. Moreno, L. Martin-Moreno, J. B. Pendry, and F. J. Garcia-Vidal (2012), Localized spoof plasmons arise while texturing closed surfaces, *Phys. Rev. Lett.*, *108*(22), 223,905.

Pozar, D. M. (2009), *Microwave engineering*, John Wiley & Sons.

Rao, S. M. (1999), *Time domain electromagnetics*, Elsevier.

Roelkens, G., P. Dumon, W. Bogaerts, D. V. Thourhout, and R. Baets (2005), Efficient fiber to SOI photonic wire coupler fabricated using standard CMOS technology, in *2005 IEEE LEOS Annual Meeting Conference Proceedings*, pp. 214–215, doi:10.1109/LEOS.2005.1547946.

Roelkens, G., et al. (2014), Silicon-Based Photonic Integration Beyond the Telecommunication Wavelength Range, *IEEE Journal of Selected Topics in Quantum Electronics*, *20*(4), 394–404, doi:10.1109/JSTQE.2013.2294460.

Rusina, A., M. Durach, and M. I. Stockman (2010a), Theory of spoof plasmons in real metals, in *SPIE NanoScience+ Engineering*, pp. 77,572R–77,572R, International Society for Optics and Photonics.

Rusina, A., M. Durach, and M. I. Stockman (2010b), Theory of spoof plasmons in real metals, *Appl. Phys. A*, *100*(2), 375–378, doi:10.1007/s00339-010-5866-y.

Ryu Cho, Y. K., et al. (2017), Sub-10 nanometer feature size in silicon using thermal scanning probe lithography, *ACS nano*, *11*(12), 11,890–11,897.

Saeedkia, D. (2013), *Handbook of terahertz technology for imaging, sensing and communications*, Elsevier.

Saleh, B. E., and M. C. Teich (2019), *Fundamentals of photonics*, john Wiley & sons.

Saraswat, K. C., and F. Mohammadi (1982), Effect of scaling of interconnections on the time delay of vlsi circuits, *IEEE Transactions on Electron Devices*, *29*(4), 645–650.

Shen, L., X. Chen, and T.-J. Yang (2008), Terahertz surface plasmon polaritons on periodically corrugated metal surfaces, *Optics Express*, *16*(5), 3326–3333, doi: 10.1364/OE.16.003326.

Shen, X., and T. Jun Cui (2013), Planar plasmonic metamaterial on a thin film with nearly zero thickness, *Applied Physics Letters*, *102*(21), 211,909, doi: 10.1063/1.4808350.

Shen, X., T. J. Cui, D. Martin-Cano, and F. J. Garcia-Vidal (2013a), Conformal surface plasmons propagating on ultrathin and flexible films, *Proc. Nat. Acad. Sci.*, *110*(1), 40–45.

Shen, X., T. J. Cui, D. Martin-Cano, and F. J. Garcia-Vidal (2013b), Conformal surface plasmons propagating on ultrathin and flexible films, *Proceedings of the National Academy of Sciences*, *110*(1), 40–45, doi:10.1073/pnas.1210417110.

Shin, D. J., et al. (2013), Integration of silicon photonics into DRAM process, in *2013 Optical Fiber Communication Conference and Exposition and the National Fiber Optic Engineers Conference (OFC/NFOEC)*, pp. 1–3.

Sirtori, C. (2002), Applied physics: Bridge for the terahertz gap, *Nature*, *417*(6885), 132–133, doi:10.1038/417132b.

Smith, D. R., J. B. Pendry, and M. C. Wiltshire (2004), Metamaterials and negative refractive index, *Science*, *305*(5685), 788–792.

Song, K., and P. Mazumder (2009), Active Terahertz Spoof Surface Plasmon Polariton Switch Comprising the Perfect Conductor Metamaterial, *IEEE Transactions on Electron Devices*, *56*(11), 2792–2799, doi:10.1109/TED.2009.2030838.

Song, K., and P. Mazumder (2011), Dynamic Terahertz Spoof Surface Plasmon #x2013;Polariton Switch Based on Resonance and Absorption, *IEEE Transactions on Electron Devices*, *58*(7), 2172–2176, doi:10.1109/TED.2011.2135370.

Song, K., and P. Mazumder (2012), Nonlinear spoof surface plasmon polariton phenomena based on conductor metamaterials, *Photonics and Nanostructures - Fundamentals and Applications*, *10*(4), 674–679, doi:10.1016/j.photonics.2012.06.008.

Song, K., and P. Mazumder (2013), Design of Highly Selective Metamaterials for Sensing Platforms, *IEEE Sensors Journal*, *13*(9), 3377–3385, doi: 10.1109/JSEN.2013.2260143.

Tousi, Y. M., O. Momeni, and E. Afshari (2012), A 283-to-296ghz vco with 0.76 mw peak output power in 65nm cmos, in *2012 IEEE International Solid-State Circuits Conference*, pp. 258–260, IEEE.

Urino, Y., T. Horikawa, T. Nakamura, and Y. Arakawa (2013), High density optical interconnects integrated with lasers, optical modulators and photodetectors on a single silicon chip, in *2013 Optical Fiber Communication Conference and Exposition and the National Fiber Optic Engineers Conference (OFC/NFOEC)*, pp. 1–3, doi: 10.1364/OFC.2013.OM2J.6.

Urino, Y., et al. (2011), First demonstration of high density optical interconnects integrated with lasers, optical modulators, and photodetectors on single silicon substrate, *Optics Express*, *19*(26), B159–B165, doi:10.1364/OE.19.00B159.

Verma, K., B. Kaushik, and R. Singh (2009), Effects of process variation in vlsi interconnects–a technical review, *Microelectronics International*.

Wallraff, A., D. I. Schuster, A. Blais, L. Frunzio, R.-S. Huang, J. Majer, S. Kumar, S. M. Girvin, and R. J. Schoelkopf (2004), Strong coupling of a single photon to a superconducting qubit using circuit quantum electrodynamics, *Nature*, *431*(7005), 162–167.

Wan, X., and T. J. Cui (2014), Guiding spoof surface plasmon polaritons by infinitely thin grooved metal strip, *AIP Advances*, *4*(4), 047,137, doi:10.1063/1.4874307.

Weile, D. S., and E. Michielssen (1997), Genetic algorithm optimization applied to electromagnetics: A review, *IEEE Transactions on Antennas and Propagation*, *45*(3), 343–353.

Wilamowski, B., E. Ferre-Pikal, and O. Kaynak (2000), Low power, current mode cmos circuits for synthesis of arbitrary nonlinear functions, in *9th NASA Symposium on VLSI Design*, pp. 7–3.

Willets, K. A., and R. P. V. Duyne (2007), Localized Surface Plasmon Resonance Spectroscopy and Sensing, *Annual Review of Physical Chemistry*, *58*(1), 267–297, doi:10.1146/annurev.physchem.58.032806.104607.

Wolf, K. B. (2004), *Geometric optics on phase space*, Springer Science & Business Media.

Woolf, D., M. A. Kats, and F. Capasso (2014), Spoof surface plasmon waveguide forces, *Optics Letters*, *39*(3), 517–520, doi:10.1364/OL.39.000517.

Wu, C., A. Salandrino, X. Ni, and X. Zhang (2014), Electrodynamical light trapping using whispering-gallery resonances in hyperbolic cavities, *Phys. Rev. X*, *4*(2), 021,015.

Wu, S., et al. (2015), Monolayer semiconductor nanocavity lasers with ultralow thresholds, *Nature*, *520*(7545), 69–72.

Xu, Z., and P. Mazumder (2012), Bio-Sensing by Mach Zehnder Interferometer Comprising Doubly-Corrugated Spoofed Surface Plasmon Polariton (DC-SSPP) Waveguide, *IEEE Transactions on Terahertz Science and Technology*, *2*(4), 460–466, doi:10.1109/TTHZ.2012.2202811.

Xu, Z., K. Song, and P. Mazumder (2012a), Analysis of doubly corrugated spoof surface plasmon polariton (dc-sspp) structure with sub-wavelength transmission at thz frequencies, *IEEE Trans. Terahertz Sci. Technol.*, *2*(3), 345–354.

Xu, Z., K. Song, and P. Mazumder (2012b), Analysis of Doubly Corrugated Spoof Surface Plasmon Polariton (DC-SSPP) Structure With Sub-Wavelength Transmission at THz Frequencies, *IEEE Transactions on Terahertz Science and Technology*, *2*(3), 345–354, doi:10.1109/TTHZ.2012.2188558.

Yablonovitch, E. (1993), Photonic band-gap structures, *J. Opt. Soc. Am. B*, *10*(2), 283–295.

Yamada, K., Y. Urino, T. Nakamura, and Y. Arakawa (2013), Integrated Silicon-based Optical Interconnect for Fast, Compact, Energy-efficient Electronic Circuit Systems | NTT Technical Review, *11*(2).

Yang, J., M. Zhao, L. Liu, H. Xiang, and D. Han (2017), Analysis of the Symmetric and Anti-Symmetric Modes in Spoof–Insulator–Spoof Waveguides, *Journal of the Physical Society of Japan*, *86*(6), 064,401, doi:10.7566/JPSJ.86.064401.

Yang, Y., H. Chen, S. Xiao, N. A. Mortensen, and J. Zhang (2015), Ultrathin 90-degree sharp bends for spoof surface plasmon polaritons, *Optics Express*, *23*(15), 19,074–19,081.

Yu, N., Q. J. Wang, M. A. Kats, J. A. Fan, S. P. Khanna, L. Li, A. G. Davies, E. H. Linfield, and F. Capasso (2010), Designer spoof surface plasmon structures collimate terahertz laser beams, *Nature Materials*, *9*(9), 730–735, doi:10.1038/nmat2822.

Zhang, X., and Z. Liu (2008), Superlenses to overcome the diffraction limit, *Nature Materials*, *7*(6), 435–441, doi:10.1038/nmat2141.

Zheng, N., M. Aghadjani, K. Song, and P. Mazumder (2013), Metamaterial sensor platforms for Terahertz DNA sensing, in *2013 13th IEEE International Conference on Nanotechnology (IEEE-NANO 2013)*, pp. 315–320, doi:10.1109/NANO.2013.6720831.